Using coherent ambient sound to probe the ocean

John Ragland

A dissertation
submitted in partial fulfillment of the
requirements for the degree of

Doctor of Philosophy

University of Washington

2024

Reading Committee:

Shima Abadi, Chair

Les Atlas

William Wilcock

Program Authorized to Offer Degree:

Electrical and Computer Engineering

University of Washington

Abstract

Using coherent ambient sound to probe the ocean

John Ragland

Chair of the Supervisory Committee:
Shima Abadi
School of Oceanography

Climate change is rapidly changing our oceans at faster time scales than have previously happened in 's history. Robust, full ocean observing systems are required for us to understand these changes and their consequences on the entire system. This work presents continued progress in the development of technologies that can utilize sound in the ocean as a tool to observe oceanographic variables, such as temperature. Coherent sound in the ocean contains information about the environment that it propagates in, and it is possible to use measured sound propagation to extract this information. Specifically, the sound speed of water is almost fully determined by the temperature of the water and measuring the sound speed of the ocean can result in robust measurements of ocean temperature. This work explores two methods of measuring acoustic propagation for the ultimate goal of oceanographic observations. The first utilizes coherent ambient sound, such as wind generated surface noise, to estimate sound propagation, and it is shown that these acoustic measurements can be utilized to estimate water column temperature. The second method uses a transmitted low frequency signal that is received across ocean basins. It is shown that this source can be received by various single hydrophones and has the potential to be used for future observations of ocean temperature.

TABLE OF CONTENTS

LIST OF FIGURES

ACKNOWLEDGMENTS

This work is based upon data created and made public by the Ocean Observatories Initiative (OOI), a major facility fully funded by the National Science Foundation under Cooperative Agreement No. 1743430, and the Woods Hole Oceanographic Institution OOI Program Office.

This material also made use of the Hybrid Coordinate Ocean Model (HYCOM), Argo, world ocean atlas (WOA), and GEBCO bathymetry data. Funding for the development of HYCOM has been provided by the National Ocean Partnership Program and the Office of Naval Research. Data assimilative products using HYCOM are funded by the U.S. Navy. Computer time was made available by the DoD High Performance Computing Modernization Program. The output is publicly available at `https://hycom.org`. ARGO data was collected and made freely available by the International Argo Program and the national programs that contribute to it. (`https://argo.ucsd.edu`, `https://www.ocean-ops.org`). The Argo Program is part of the Global Ocean Observing System. `https://doi.org/10.17882/42182`. World ocean atlas is a dataset provided freely and openly by the National Oceanic and Atmospheric Adminstration `https://www.ncei.noaa.gov/products/world-ocean-atlas`, and GEBCO bathymetry data is also freely available at `https://www.gebco.net/`.

I would like to acknowledge my advisor and all of the collaborators who have invested time in my development as a researcher, and the development of this work: Shima Abadi, Karim Sabra, Kai Gemba, Nicholas Durofchalk, David Dall'Osto

I would also like to acknowledge discussions with Dr. Kathleen Stafford which contributed to the fin-whale chorus sections of chapter 3.

Lastly, I would like to thank the Office of Naval Research for providing the funds for my PhD. Over the past four years, I have developed a passion for acoustic oceanography, and the first thing that made this possible was the funding supplied by ONR to pursue a PhD.

DEDICATION

I would like to acknowledge my unwavering companion, coffee, without whom none of this would have been possible.

But seriously, the marathon of completing a PhD is quite arduous, and I am incredibly thankful for the support of my wife Madison. From moving out to Seattle without a job lined up, to single-handedly keeping us financially afloat, to the immeasurable other areas that she has supported me, this accomplishment is as much hers as mine.

Chapter 1

INTRODUCTION

Acoustic waves contain information about the environment that they propagate in. Specific to ocean acoustics, measured propagation can be used to estimate acoustic and oceanographic variables such as sound-speed structure, water temperature, and water velocity [93]. This work presents continued development of two different methods to measure acoustic propagation in the ocean at different spatial scales. The first method, ocean ambient noise interferometry, uses coherent ambient sound to passively estimate the Green's function. Bottom mounted hydrophones in the deep ocean are used to measure arrival times in the Green's function with high enough accuracy to sense sub-seasonal fluctuations in a local (∼3 km) environment. The second method, receptions of low-frequency acoustic transmissions across ocean basins (∼4000 km), is explored and discussed.

Both methods use the hydrophones of the cabled ocean observatory, the Ocean Observatories Initiative (OOI). This observatory consists of a diverse suite of oceanographic sensors, including eleven hydrophones that are located at various depths and environments in the northeast Pacific Ocean. The data is fully open-access, creating a rich new dataset of underwater acoustics that can contribute to the open development of science and sensing technology.

The UNESCO led program, the Global Ocean Observing System (GOOS), recently named underwater sound as an essential ocean variable [149]. Because of this, there is increased need and interest to increase PAM infrastructure. The techniques presented and explored within this thesis aim to leverage existing and future PAM infrastructure to be able to measure acoustic propagation, alongside ambient sound levels. These measurements of acoustic propagation could then be used to invert for oceanographic variables such as integrated, deep ocean temperature.

1.1 Dissertation Organization

This chapter will provides context for the subsequent chapters of this work. In this chapter, the technique of ambient noise interferometry is explained, a theoretical derivation is provided, and a discussion of previous results in ocean acoustics is presented. Relevant prior work in ocean basin tomography will be presented, and the signal processing methods used for ocean basin acoustic receptions will be discussed as it relates to positive receptions of the Kauai Beacon by OOI hydrophones.

In Chapter 2, the statistics of the ambient soundscape, measured for all bottom-mounted OOI hydrophones, is presented. Understanding the features that are present in the ambient soundscape informs the technique of ambient noise interferometry, explored in future chapters, by characterizing what sound sources are being utilized to illuminate the acoustic propagation. Additionally, the statistics presented in this chapter provide insight into the noise floor for receptions of the Kauai Beacon.

In Chapter 3, the cross-correlations of ambient sound, measured by two OOI hydrophones, is investigated over 6 years. The cross-correlations of ambient sound are found to reliably converge to the empirical Green's function, containing multiple propagation paths. This is the first time that ambient noise interferometry has been used to resolve multi-path propagation in the deep ocean. The emergence of the Green's function and the signal-to-noise ratio are quantified. Additionally, various features in the cross-correlations throughout the six years are discussed.

In Chapter 4, a seismic reflection study is used as data of opportunity to experimentally characterize how surface source locations affect the correlation between two hydrophones. These results demonstrate that the sources illuminating the acoustic steep angle propagation paths that reflect off of the bottom or surface of the ocean are illuminated by local surface sources.

In Chapter 5, acoustic arrival times are estimated from the cross-correlations of ambient sound. The arrival times are compared to arrival times simulated with the ocean model HYCOM. A linear inversion model is proposed, and depth averaged water temperature is estimated over eight years with a high enough accuracy to sense sub-seasonal changes.

In Chapter 6, the potential of using OOI hydrophones to measure ocean basin acoustic propagation is explored. Acoustic arrivals are simulated and compared to positive receptions of the Kauai Beacon at various OOI hydrophones, over the course of the first year of transmissions (March 2023 - March 2024).

In Chapter 7, the results of this work are summarized.

1.2 Ocean ambient noise interferometry

In this section, the technique of ambient noise interferometry is explained, a theoretical derivation is provided and a discussion of previous results in ocean acoustics is presented.

The ocean ambient soundscape is dominated by several source mechanisms. Wind and rain generated surface sound, marine mammal vocalizations, seismic activity, and anthropogenic sources make up the primary contributors to the soundscape [161, 169, 96, 89, 90, 33]. This ambient sound contains critical information about the ocean environment. The individual sources that are present in ocean ambient noise can be used to study these specific phenomena, such as migration patterns of marine mammals [85, 75, 167] or rain and wind patterns [76, 124, 126]. It turns out, however, that the total, diffuse ambient sound field can also be used to learn information about the ocean. Ambient noise interferometry utilizes the fact that the spatial coherence of an ambient sound field approximates the channel impulse response between sensors, and these estimates of acoustic propagation can be used to estimate water temperature, currents, sound speed structure, and sensor location [172, 49, 140, 121].

For a diffuse sound field, where sound comes from all directions equally, sound waves that propagate through both receivers will have a constant phase difference and sound waves that take independent paths to the two receivers will have a non-constant phase difference. This means that if you take the cross-correlation, all sound that propagates through both sensors will constructively add together and all other sound will deconstructively interfere and cancel out. It turns out that, because of this, the time derivative of the cross-correlation between two points gives the Green's function at one point as if there was a source at the other, which is the basis of ambient noise interferometry. This technique has been applied to various fields such as helio-seismology, ultrasound, seismology and underwater acoustics [114, 163, 129, 151]

1.2.1 Theoretical derivation

In the following section, a mathematical derivation of the technique of ambient noise interferometry is presented. Specifically, the derivation will focus on applications to ocean ambient noise interferometry. The fundamental equation of NI will be derived, and the effect of non-diffuse sound sources will be explored. This derivation integrates several independent works [158, 135, 177, 137, 43].

Given the linear acoustic wave equation (equation 1.1), the pressure measured at location $\mathbf{x}_i$, due to a single sound source at location $\mathbf{x}_j$ and time history $s(t)$ can be represented with convolution (Equation 1.2), where $G_{\mathbf{x}_j\mathbf{x}_i}(t)$ is the Green's function characterizing acoustic propagation from $\mathbf{x}_j$ to $\mathbf{x}_i$, (satisfying equation 1.3), and where $*$ denotes convolution.

$$\nabla^2_{\mathbf{x}} p(\mathbf{x},t) = \frac{1}{c^2}\frac{\partial^2 p(\mathbf{x},t)}{\partial t^2} \tag{1.1}$$

$$p(\mathbf{x}_i) = s_{\mathbf{x}_j}(t) * G_{\mathbf{x}_j\mathbf{x}_i}(t) \tag{1.2}$$

$$(\nabla^2 + k^2(\mathbf{x}_i))G_{\mathbf{x}_j\mathbf{x}_i}(t) = \delta(\mathbf{x}_i - \mathbf{x}_j)\delta(t) \tag{1.3}$$

The cross-correlation between points in space, $\mathbf{x}_1$ and $\mathbf{x}_2$ is given in equation 1.4.

$$\begin{aligned}\langle C_{12}(\tau)\rangle &= \langle p(t+\tau,\mathbf{x}_1)p^*(t,\mathbf{x}_2)\rangle \\ &= \frac{1}{2\pi}\int_{-\infty}^{\infty}\langle P(\omega,\mathbf{x}_1)P^*(\omega,\mathbf{x}_2)\rangle\, e^{j\omega\tau}d\tau\end{aligned} \tag{1.4}$$

Assuming a distribution of sound sources with frequency content $N(\omega, \mathbf{x}_N)$, the pressure measured by a sensor at $\mathbf{x}_1$ is given by equation 1.5, where $H_1(\omega)$ is the frequency response of the sensor at location $\mathbf{x}_1$.

$$P(\omega, \mathbf{x}_1) = H_1(\omega) \int_V G_{\mathbf{x}_N \mathbf{x}_1}(\omega) N(\omega, \mathbf{x}_N) dV(\mathbf{x}) \tag{1.5}$$

Plugging equation 1.5 into equation 1.4, you get equation 1.6.

$$\begin{split} \langle C_{12}(\tau) \rangle = \frac{1}{2\pi} \int_{-\infty}^{\infty} H_1(\omega) H_2^*(\omega) \times \\ \iint_{V,V'} G_{\mathbf{x}_N \mathbf{x}_1}(\omega) \left\langle N(\omega, \mathbf{x}_N) \right\rangle G^*_{\mathbf{x'}_N \mathbf{x}_2}(\omega) \left\langle N^*(\omega, \mathbf{x}'_N) \right\rangle dV(\mathbf{x}_N) dV(\mathbf{x}'_N) e^{j\omega\tau} d\tau \end{split} \tag{1.6}$$

If noise sources are spatially uncorrelated, then equation 1.7 holds, where $S(\mathbf{x}_N, \omega)$ is the spatial distribution of the noise spectral density.

$$\langle N(\omega, \mathbf{x}_N) N^*(\omega, \mathbf{x}_N{}') \rangle = S(\mathbf{x}_N, \omega) \delta(\mathbf{x}_N - \mathbf{x}_N{}') \tag{1.7}$$

Plugging equation 1.7 into 1.6 gives 1.8, where K is the cross-correlation sensitivity kernel (equation 1.9), and $S_H(\omega)$ is the cross spectral density of the two sensor responses.

$$\langle C_{12}(\tau) \rangle = \frac{1}{2\pi} \int_\omega S_H(\omega) \int_V S_N(\mathbf{x}_N, \omega) K(\mathbf{x}_N, \omega, |\mathbf{x}_2, \mathbf{x}_2) dV(\mathbf{x}_N) e^{j\omega\tau} d\omega \tag{1.8}$$

$$K(\mathbf{x}_N, \omega, |\mathbf{x}_2, \mathbf{x}_2) = G(\omega, \mathbf{x}_N, \mathbf{x}_1) G^*(\omega, \mathbf{x}_N, \mathbf{x}_2) \tag{1.9}$$

The cross-correlation sensitivity kernel characterizes the contribution of a specific source location, $\mathbf{x}_N$, to the cross-correlation between two sensors located at $\mathbf{x}_1$ and $\mathbf{x}_2$ [135, 107]. This definition differs from the definition by Skarsoulis et. al. [135] because the sensor response is not included in the cross correlation sensitivity kernel. If the noise spectral density is uniform for all locations (i.e. $S_N(\mathbf{x}_N, \omega) = S_N(\omega)$ for all $\mathbf{x}_N$), then you get equation 1.10, where $D(\omega) = S_N(\omega) S_H(\omega)$.

$$\langle C_{12}(\tau) \rangle = \frac{1}{2\pi} \int_\omega D(\omega) \int_V K(\mathbf{x}_N, \mathbf{x}_1, \mathbf{x}_2, \omega) dV(\mathbf{x}_N) e^{j\omega\tau} d\omega \tag{1.10}$$

There are several techniques that have been used to evaluate the volume integral in equation 1.10. The volume integral can be converted to a surface integral using the divergence theorem [177], or the asymptotic technique of stationary phase can be used to simplify the integral for various environments [43, 137]. For a fully diffuse sound source distribution, both of these methods result in equation 1.11, which is the fundamental equation of noise interferometry. $D(\tau) = F^{-1}\left\{D(\omega)\right\}$. $D(\tau)$ characterizes how the two Green's functions are illuminated by the sound sources and sensor responses.

$$\left\langle \frac{d}{d\tau} C_{12}(\tau) \right\rangle = D(\tau) * [G_{12}(\tau) - G_{21}(-\tau)] \tag{1.11}$$

Given that sound source distributions in the ocean are not diffuse and are usually distributed along the surface, it is important to quantify how the non-diffuse sound source distributions affect the estimate of the Green's function. For the ocean acoustic propagation explained by rays, it has been shown that sources along the extensions of eigen-rays that connect the two sensors contribute to the correlation. All other source locations destructively interfere and cancel out [43, 158, 137]. For acoustic propagation explained by normal modes, sources within the plane connecting the two sensors and perpendicular to the ocean surface contribute to the correlation and the depths of the sources illuminate the different mode shapes [43, 109]. It's been shown that as long as the sound sources adequately illuminate the acoustic propagation, the coherence converges to an amplitude shaded Green's function (Equation 1.12) [43, 158, 120, 134].

$$\left\langle \frac{d}{d\tau} C_{12}(\tau) \right\rangle = D(\tau) * \left[\tilde{G}_{12}(\tau) - \tilde{G}_{21}(-\tau)\right] \tag{1.12}$$

The amplitudes of $\tilde{G}_{12}(\tau)$ and $\tilde{G}_{21}(\tau)$ are a function of the sound source statistics, which are not usually known. However, the phase of the amplitude shaded Green's functions remains the same as the actual Green's functions. From a mode or ray based perspective, the phase of the signal is what carries the information about the environment (i.e. ray travel times or specific mode phases). This means that, even if the sound source distribution is not diffuse, passive acoustic based environmental remote sensing is still possible [43].

1.2.2 Previous experimental results

Green's functions have been successfully estimated in a diverse set of ocean environments and illuminating sound sources. [116, 40, 52, 10, 11, 173, 110]. These passively estimated Green's functions have also been successfully used to estimate oceanographic variables. Using two arrays of hydrophones located in the sound channel, changes in water temperature were measured over a distance of 130 km [173]. An experiment in shallow waters off the coast of Florida has been able to measure sub-seasonal sound speed structure [177], mode shapes [44], and flow velocities [50]. This technique has also been used to measure bottom properties [145, 142, 51, 143].

1.3 Kauai Beacon transmissions

Sound speed is almost linearly related to water temperature and water pressure [77]. The higher the temperature and pressure, the higher the sound speed. For deep water environments, pressure increases with increasing depth and temperature decreases with increasing depth. The resulting typical deep ocean sound speed has a minimum around 1000 m which forms a sound channel, where acoustic waves can travel very long distances without interacting with the bottom or surface. Additionally, acoustic absorption is very low at low frequencies (dropping as low as $0.001\,\frac{\mathrm{dB}}{\mathrm{km}}$ around 100 Hz [153]). Because of these factors, low frequency underwater sound can travel across entire ocean basins [92]. This means that acoustic signals with relatively low energy can be transmitted and received across ocean basins at ranges on the order of 4000 km. A source off the coast of Kauai with source levels similar to blue whale vocalizations [42] has recently begun transmissions every four days. A similar experimental setup was used in the 1990s and early 2000s to successfully measure fluctuations in ocean basin travel times which are closely related to deep ocean temperature [34, 61, 62]. Receptions of the Kauai Beacon have been recently explored for two hydrophone locations in the Pacific [42]. In chapter 6, the first receptions of the KB by OOI hydrophones in a diverse set of ocean environments is presented.

Previous ocean basin acoustic measurements utilized large arrays of classified hydrophones, which were originally implemented for submarine detection during the Cold War [36]. Utilizing existing infrastructure allowed for a cost-effective method to retrieve acoustic receptions with large arrays, which enabled more processing gain from beamforming techniques. However, since the data was classified, it did not allow for the transparent description of the methods, which might aid in the adoption of these techniques by the greater oceanographic community. Additionally, the secretive nature of the data sources may have contributed to a larger distrust and associated controversy around ocean basin tomography experiments conducted in the 1990s and 2000s [106]. By utilizing existing and future open-access PAM infrastructure, the methods developed and the exact locations of hydrophones can be publicly available. This will be beneficial for contributing to open scientific development, but more advanced detection methods will need to be developed since the processing gain will be lower. Developing methods of processing and inversion centered around single hydrophone measurements will also allow for larger and more diverse sensor infrastructure to be used for ocean basin tomography using the KB.

1.3.1 Pulse compression and signal processing

The KB utilizes the concept of pulse compression to spread coherent energy out in time and frequency, which lowers the required transmit power for positive receptions across the ocean basin. KB uses a carrier frequency of 75 Hz to transmit a modulated, 1023 bit binary MLS. The 1023 bit, pseudorandom MLS is generated with 10 shift registers with a wiring configuration defined by the octal law 3471. (see [53, p. 62] for more information). Each bit is transmitted with Q=2, meaning that each bit consists of two cycles of the 75 Hz carrier signal, and the bits are phase modulated by 180°. This results in a bandwidth of the signal (defined by the first zero crossing) between 37.5 - 112.5 Hz. Figure 1.1 shows a small section of the transmitted signal in time and the frequency content of the signal, and the auto-correlation of the signal. The 1023 bit MLS encoded signal is 27.28 s long. The auto-correlation of a MLS encoded signal is a band limited impulse. This means that the channel impulse response can be estimated by match-filtering the received signal with a replica of

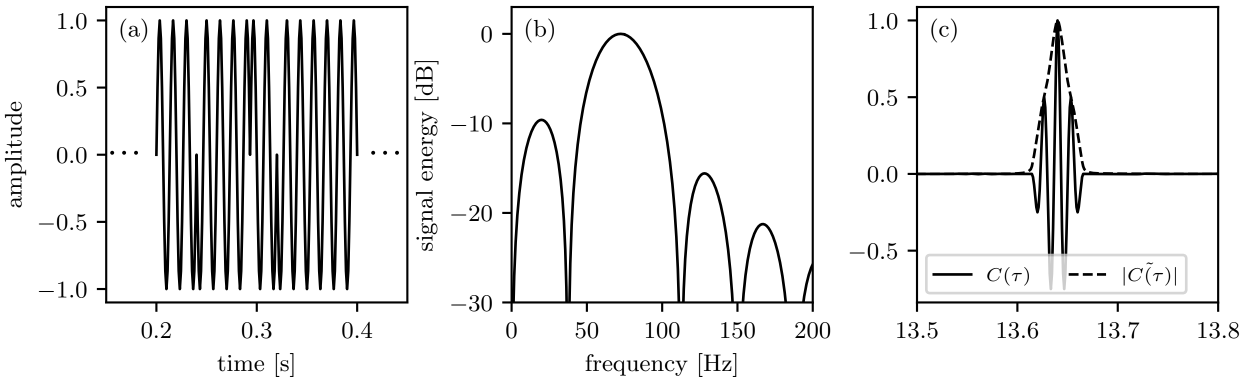

Figure 1.1: (a) Section of transmitted signal in time (b) frequency content of the transmitted signal. (c) Auto-correlation of the MLS modulated signal.

the transmitted signal. The match-filtered output results in a 27 ms wide pulse.

For a single transmission of the Kauai Beacon, the 27.28 s signal is repeated 44 times to make a 20 min transmission. After match filtering the signal with the 27.28 s replica, the reception can be averaged together in subsequent 27.28 s sections over the twenty-minute transmission, and coherent acoustic arrivals will constructively increase the processing gain. For a fully coherent ocean over the twenty-minute transmission, the maximum theoretical processing gain is 43.2 dB [42].

Chapter 2

OVERVIEW OF AMBIENT SOUND USING OCEAN OBSERVATORIES INITIATIVE HYDROPHONES

Abstract

The Ocean Observatories Initiative (OOI) sensor network provides a unique opportunity to study ambient sound in the north-east Pacific Ocean. The OOI sensor network has 5 low frequency (Fs = 200 Hz) and 6 broadband (Fs = 64 kHz) hydrophones that have been recording ambient sound since 2015. In this chapter, I analyze acoustic data from 2015 - 2020 to identify prominent features that are present in the OOI acoustic dataset. Notable features in the acoustic dataset that are highlighted in this chapter include volcanic and seismic activity, rain and wind noise, marine mammal vocalizations, and anthropogenic sound such as shipping noise. For all low frequency hydrophones and four of the six broadband hydrophones, I will present long-term spectrograms, median time-series trends for different spectral bands, and different statistical metrics about the acoustic environment. The statistical properties of the ambient sound presented in this chapter will inform the techniques explored in subsequent chapters. We find that 6-year acoustic trends vary depending on the location of the hydrophone and the spectral band that is observed. Some locations and spectral bands see increases in spectral levels while others see decreases in spectral levels over the course of the 6 years. Lastly, I discuss future areas of research that the OOI dataset lends itself to.*

2.1 *Introduction*

The Ocean Observatories Initiative (OOI) is an ocean observing network providing data from more than 800 instruments. The different sensor networks measure physical, chemical,

---

*This paper was joint work with co-first-authors John Ragland and Felix Schwock, as well as contributions from Shima Abadi and Matthew Munson and is available as:
Ragland, J., Schwock, F., Munson, M., and Abadi, S. (2022). “An overview of ambient sound using Ocean Observatories Initiative hydrophones,” The Journal of the Acoustical Society of America, 151, 2085–2100. doi:10.1121/10.0009836

geological, and acoustic data spanning from the air-sea interface to the seafloor. All of the data that is produced by OOI is available publicly. Public ocean datasets such as OOI play an important role in understanding the ocean [65]. In this chapter I will be providing an overview of acoustic data that is available through OOI from 2015 through 2020.

Currently, there are eleven different hydrophones that are part of the OOI sensor network that have been recording ambient sound from around the north-east Pacific Ocean since 2015. Five of the hydrophones are low frequency (LF) hydrophones with a sampling rate of 200 Hz. Six of the hydrophones are broadband (BB) hydrophones with a sampling rate of 64 kHz. Two of the BB hydrophones are located at depths of 200 m and are positioned in the Sound Fixing And Ranging (SOFAR) channel. The rest of the BB hydrophones and all of the LF hydrophones are located on the seafloor. The hydrophones are mounted on a tripod and approximately are 40 cm off of the seafloor, and no flow-shields are used. These long-term ambient sound recordings from the OOI network provide the opportunity for many data and experimentally driven advancements in the field of ocean acoustics. In this chapter, I will present a long-term statistical analysis of the ambient sound recorded at nine of the eleven hydrophones, as well as highlight acoustic features that are present throughout the six years of data presented in this chapter.

Monitoring long-term underwater ambient sound levels has received increasing attention in past years with more datasets emerging that cover ever larger temporal and spatial scales. Along with OOI, another ocean observatory that monitors the north-east Pacific is the Ocean Networks Canada (ONC) observatory [†]. [58] have evaluated data from the Ocean Noise Reference Station (NRS) network, consisting of twelve autonomous passive acoustic recorders distributed across various locations in the Atlantic and Pacific Ocean. Various datasets have also been used to compare LF sound spectral levels from the 1950s and 1960s to data recorded during the 1990s and 2000s to analyze the effect of increased shipping activity on underwater sound [5, 4, 81, 132]. Results seem to be highly dependent on the measurement site but generally indicate that the increase in ambient noise due to shipping activity has slowed down in more recent years compared to the the 1950s and 1960s data reported by [115]. These results were also confirmed by [21] and [39], who used hydrophone volume and line arrays in their measurement apparatus. Additionally, a statistical analysis of 2 years of ambient sound data investigating the shipping and whale sound contributions has been conducted in the Pacific [29]. With its eleven hydrophones recording ambient sound since 2015, the OOI provides an excellent complementary dataset to this area of ongoing research.

The OOI hydrophone dataset contains many different notable acoustic features. Some of these features are outlined in detail in section 2.3. A review of previous literature for some of the pertinent acoustic features is provided below.

Marine Mammals: Due to the difficult nature of directly observing information about marine mammals, passive acoustic monitoring is one the of the primary tools used for learning more about marine mammal populations in the ocean. The OOI hydrophone network

---

[†] `https://www.oceannetworks.ca/`

contains many marine mammal signals that offer the potential for further exploration (see 2.3). Passive acoustic monitoring of marine mammals is a well explored field [15, 170, 68, 85] that the OOI dataset can contribute to. One of the primary biological features that is present in the OOI acoustic dataset is seasonal fin whale calls. Fin whale calls and the inter-pulse intervals of these calls have been extensively explored [147, 138, 133, 161, 139]. While there are several types of fin whale calls, the most common call consists of a downward swept signal lasting approximately one second centered around 20 Hz. The presence of energy near 20 Hz can be used to monitor the migration patterns and seasonal fluctuations of fin whale vocalizations [79, 97]. Fin whale calls contain complex temporal and frequency patterns that indicate communication between multiple fin whales [79, 138].

Wind and Rain: Two of the six OOI BB hydrophones are accompanied by surface buoys that continuously record data at the air-sea interface such as wind vectors and rain rates. Those in-situ meteorological measurements with high temporal resolution (1-min) provide an excellent opportunity to use the OOI data for studying wind and rain noise in the northeast Pacific, which has recently been done by [126] and [124]. The results from these studies complement other studies on wind and rain noise that use long-term and large-scale hydrophone networks, most notably [69, 169, 76, 59].

Ship Noise: Sound from commercial ships has long been studied to assess its impact on the oceanic environment and marine life in particular [57, 86, 88]. It is also known that the acoustic signature of ships depend on a variety of factors such as ship type, size, and velocity [128, 157, 82, 83, 131, 41]. Since some of the OOI hydrophones are located in the vicinity of major shipping lanes, a large number of ship passages can be found in the dataset. Ship types observed in the OOI dataset include merchant ships, research vessels, fishing vessels, and recreational boats. Very recently, [30] explored the effects of the COVID-19 pandemic on ship noise using the OOI data.

The remainder of this chapter is outlined as follows: Sec. 2.2 describes the OOI hydrophones and data processing framework employed in this work. Sec. 2.3 presents spectrograms showing long-term sound spectral levels as well as specific acoustic features that can be found in the OOI hydrophone data. Sec. 2.4-2.7 then analyze mean spectral level time series, sound distribution, noise floor time series, inter-hydrophone cross-correlations and power spectrum covariance matrices extracted from the long term spectrograms. Sec. 2.8 discusses possible areas of future investigation using the OOI dataset. Finally, Sec. 2.9 summarizes the results of this research.

2.2 Experimental setup and data processing

The OOI acoustic dataset consists of 11 hydrophones located off of the north-west coast of the continental United States. There are 5 low frequency (LF) HTI-90-U hydrophones (High Tech, Inc., Mississippi, U.S.) and 6 broadband (BB) icListen HF hydrophones (Ocean Sonics, Nova Scotia, Canada) with sampling frequencies of 200 Hz and 64 kHz, respectively. For the purpose of this chapter, acoustic data analysis from all LF hydrophones and four of the six BB hydrophones will be presented. Two BB hydrophones are omitted because prolonged, strong interfering signals from other measurement instruments co-located with the hydrophones obscured the acoustic records. Fig. 2.1(a) shows the geographic location of the 9 hydrophones. Fig. 2.1(b) shows the measured sound speed profiles for different water column profilers in the OOI dataset along with the depths of the different hydrophones. The profiles used to measure the sound speeds are often unreliable at large depths, which results in gaps in the data. The lighter traces for Axial Base and Oregon Slope are a linear regression from valid data below the thermoclines. Data availability for the 9 hydrophones analyzed in this chapter is shown in Fig. 2.2. Table 2.1 shows the depth and location of all 9 hydrophones.

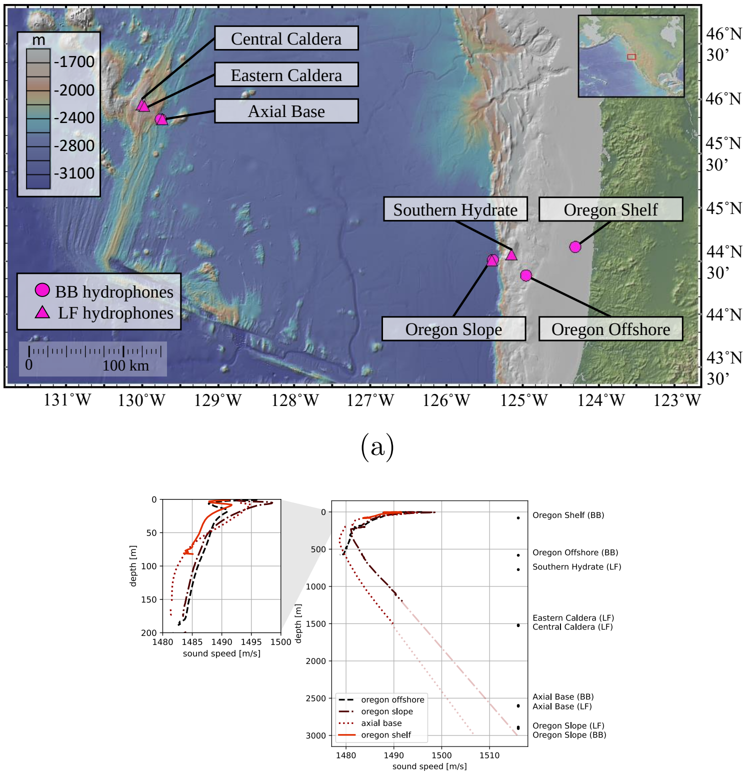

(a)

(b)

Figure 2.1: (a) Location of broadband (BB) and low frequency (LF) hydrophones in the north-east Pacific Ocean. The Axial Base location and the Oregon Slope locations have both an LF and BB hydrophone. (b) Sound speed profiles measured by different OOI profiles and the depths of the OOI hydrophones.

OOI has a web based data explorer (https://dataexplorer.oceanobservatories.org/) that has many of the data products easily accessible. Unfortunately, due to the high file size

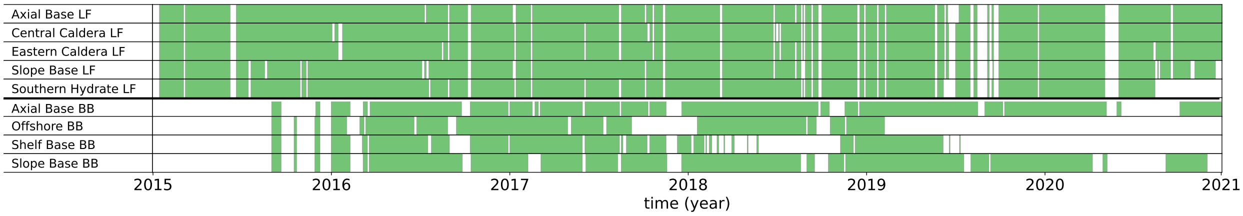

Figure 2.2: Data availability for all 9 hydrophones analyzed in this chapter

of the acoustic datasets, hydrophone data is not available through the OOI Data Explorer and must be accessed through the OOI raw data server (BB hydrophones) or IRIS data server (LF hydrophones). These data servers save the data in mseed format, and it is not straightforward to use the raw data server for analysis.

In order to make the OOI acoustic dataset more easily accessible and to expedite the research process using OOI datasets, I helped develop a public Python package called OOIPy [127]. OOIPy handles accessing the data from the raw data servers and converts the data into formats that are within the Python scientific computing framework. OOIPy also has several data processing methods that aid in the statistical analysis of the acoustic dataset. The Welch mean and median power spectral density (PSD) estimates using calibrated hydrophone data can be calculated within OOIPy, and these PSDs can be grouped together to form spectrograms.

OOIPy also handles the calibration of hydrophone data. For the broadband (BB) hydrophones, the frequency responses of the devices were recorded by the manufacturer in a water tank for frequencies between 0 - 200 kHz. For the low frequency hydrophones a single sensitivity value is reported which is valid between 2 - 90 Hz. Calibration data sheets for individual OOI hydrophones can be found at `https://github.com/OOI-CabledArray/calibrationFiles`. The 2 Hz cutoff for the LF hydrophones is the lowest frequency that the hydrophones are calibrated to, however there does not seem to be a physical filter with this cutoff present in the data. The 90 Hz cutoff is due to the digital filtering required to down-sample the acoustic data to a sampling frequency of 200 Hz. This cutoff is characterized by the response files available for specific hydrophones at `https://ds.iris.edu/mda/OO/`.

The description of ambient sound and analysis of long-term trends and seasonal patterns in this chapter is based on the computation of PSD estimates. To do so, the multi-year acoustic time series obtained from each hydrophone are divided into blocks of 4096 samples for the BB and 512 samples for the LF hydrophones, whereby adjacent blocks overlap by 50 %. Afterwards each block is multiplied by a Hann window data taper to reduce spectral leakage and the magnitude square of the fast Fourier transform is computed. That is, for each block a modified periodogram is estimated. A window length of 4096 samples for the BB data, combined with a median averaging as described below, was chosen. The window length was chosen as a trade-off between spectral resolution and robustness against interfering

Table 2.1: Name, identifier within the OOI data portal (ID), depth, geospatial coordinates, and type of the 9 OOI hydrophones used in this study.

hydrophone	ID	depth (m)	coordinates	type
Axial Base	MJ03A	2608	45°49′12.7″ N 129°44′12.2″ W	LF
Central Caldera	MJ03F	1527	45°57′16.8″ N 130°0′32.4″ W	LF
Eastern Caldera	MJ03E	1518	45°56′22.8″ N 129°58′25.6″ W	LF
Southern Hydrate	LJ01 B	774	44°34′9″ N 125°8′52.5″ W	LF
Oregon Slope	MJ01 A	2907	44°30′35.2″ N 125°24′18.8″ W	LF
Axial Base	LJ03A	2598	45°49′0.1″ N 129°45′15.3″ W	BB
Oregon Offshore	LJ01 C	582	44°22′9.9″ N 124°57′12.8″ W	BB
Oregon Shelf	LJ01 D	81	44°38′13.5″ N 124°18′21.1″ W	BB
Oregon Slope	LJ01 A	2888	44°30′54.3″ N 125°23′24.1″ W	BB

signals, particularly from Acoustic Doppler Current Profiler (ADCP) pings.

The resulting periodograms for each hydrophone are stacked together to obtain long term spectrograms. As the resulting amount of data is generally intractable for post-processing and evaluation, different temporal scales can now be achieved by averaging a certain number of periodograms together to achieve a single (compressed) PSD estimate. The averaging time applied varies depending on whether a "global" representation of the data or a detailed view on a specific acoustic feature was desired. For the long-term spectrogram in Fig. 2.3 and 2.4, for example, averaging was conducted over 15-min periods, which is equivalent to 28 124 and 702 periodograms for the BB and LF hydrophones, respectively. Furthermore, median averaging is always employed instead of mean averaging to mitigate the effect of outliers [125], which are particularly strong for the BB hydrophones due to ADCP pings. The resulting spectral estimates can therefore be regarded as Welch median PSD estimates [168, 125]. It is noted that the frequency dependent sensitivity correction and the median averaging over multiple periodograms is conveniently implemented in OOIPy.

Due to the size of the BB raw dataset, cloud computing was employed to compute the BB long-term spectrograms. Thereby, a separate Microsoft Azure virtual machine (Standard A2m V2 with 2 CPUs and 16 GB of RAM) has been used for processing a 3-month chunk of data. In total 18 machines were running concurrently and the processing time for each machine was between 2 - 5 days, depending on the data coverage within the respective 3-month time span.

2.3 Long-term spectrograms and Acoustic Features

Fig. 2.3 shows the long-term spectrograms for the four broadband (BB) hydrophones investigated in this chapter. A 15 minute Welch-median power spectral density (PSD) estimate is calculated with a Hann window, 4096 FFT points and 50 % overlap. Fig. 2.4 shows the long-term spectrograms for the low frequency (LF) hydrophones. A 15 minute Welch-median PSD estimate is calculated with a Hann window, 512 FFT points and 50 % overlap.

For all BB, long-term spectrograms shown in Fig. 2.3, spectral levels decrease with increasing frequency. Temporal patterns of the ambient sound, however, clearly differ between locations and also depend on the frequency band. Further investigation into the time dependence of spectral levels is presented in section 2.4.

The LF spectrograms shown in Fig. 2.4 display several notable features. Around 1 Hz, there is a spike of energy that is due to microseisms [166]. At 20 Hz, seasonal vocalizations of fin whales can clearly be seen at all 5 hydrophone locations. The high prevalence of fin whale signals in the LF hydrophones could lend itself to further studies of fin whale migration using acoustic monitoring. In April of 2015, the Axial Seamount Volcano erupted. This eruption can be seen in the Axial Base, Central Caldera and Eastern Caldera spectrograms as a BB spike. In July and August of 2019, there was a seismic reflection survey that was conducted directly over the Axial Seamount Volcano [113]. A spike in energy can be seen at all 5 locations, with the effect being much clearer for the Axial Base, Central Caldera, and Eastern Caldera locations.

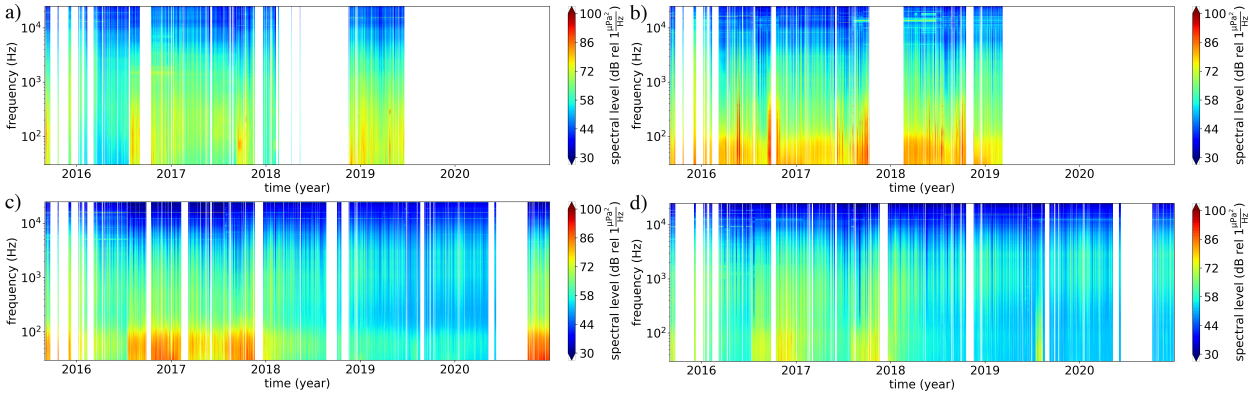

Figure 2.3: Six-year spectrograms computed with Welch median PSD estimate for broadband hydrophones (a) Oregon Shelf, (b) Oregon Offshore, (c) Oregon Slope, and (d) Axial Base.

2.3.1 Specific Acoustic Signals

Besides analyzing long-term patterns in ambient sound, many different specific acoustic features can also be observed in the OOI hydrophone dataset. Some examples of resolvable features include rain, wind, marine mammals, ships, earthquakes, and volcanic activity. This rich collection of many different types of acoustic features lends itself to many acoustic

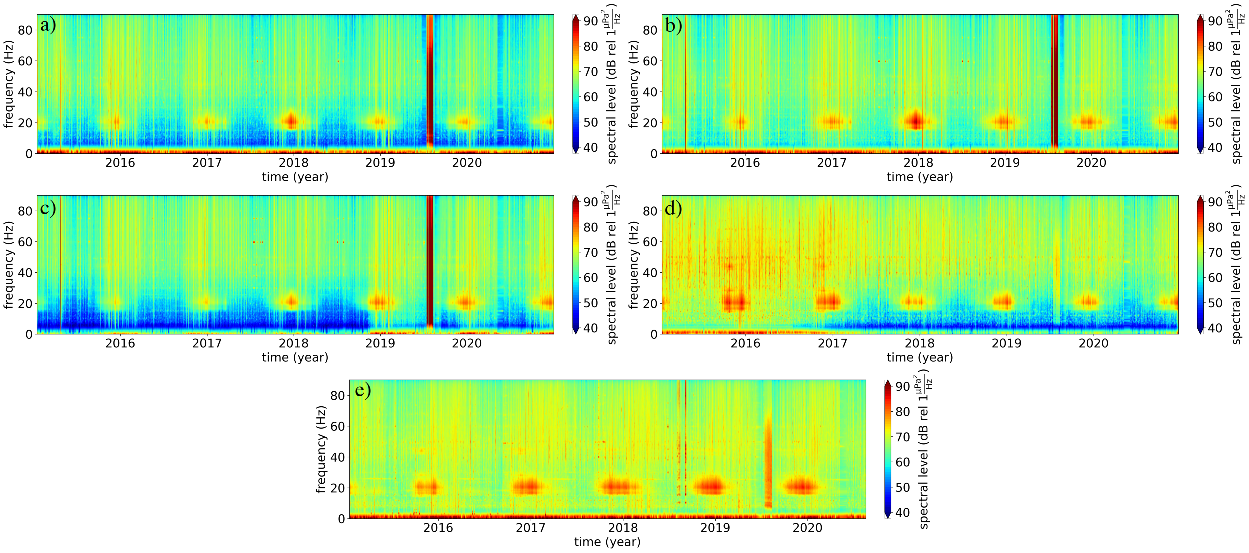

Figure 2.4: Six-year spectrogram computed with Welch median PSD estimate for low frequency hydrophones (a) Axial Base, (b) Central Caldera, (c) Eastern Caldera, (d) Oregon Slope and (e) Southern Hydrate.

monitoring applications. Examples of some prominent acoustic features shown in Fig. 2.5. Color scales for individual spectrograms are different.

An example of a ship passing directly over the Axial Base LF and BB hydrophones is shown in Fig. 2.5(a) and 2.5(b). Using AIS data, this ship was determined to be a cargo ship of length 189 m that passes within 4.839 km of the hydrophone with an approximate speed of 12 knots. The V-shape in the ship passage spectrogram described in [82] can be clearly seen in 2.5(b). At the time of nearest arrival, the recorded sound intensity at 50 Hz is 94.731 dB relative to $\frac{\mu Pa^2}{Hz}$. Using a simple spherical spreading model, the range of the ship at nearest arrival, and the depth of the hydrophone, the source level of this ship is estimated to be 169.54 dB relative to $\frac{\mu Pa^2}{Hz}$ at 50 Hz.

A spectrogram of four air-gun shots recorded by the Axial Base BB hydrophone from the 2019 seismic reflection survey [113] is shown in Fig. 2.5(c). The research vessel is 14.5 km from Axial Base hydrophone during the recording. The source level of the air-gun shots is approximately 225 dB at 1 m relative to $\frac{\mu Pa^2}{Hz}$.

Fig. 2.5(d) shows a sequence of individual fin whale calls and is recorded by the Axial Base LF hydrophone in December 2016. For a single call, the initial call and subsequent echos is visible in the spectrogram. In [79], a study of fin whale vocalizations reveals that different fin whales with different frequency signatures of their calls are likely interacting with each other. This could be an explanation for the alternating frequencies of the calls seen in 2.5(d). As seen in Fig. 2.4, 20 Hz energy from seasonal Fin whale vocalizations are present at all LF hydrophones locations. In chapter 3, it is shown that by using noise interferometry between the Eastern Caldera and Central Caldera LF hydrophones, a fin whale chorus can be detected with directionality pointed toward the Bearing Sea. Fig. 2.5(e) shows an example of unidentified marine mammal vocalizations recorded by the Oregon Offshore BB hydrophone in January 2019. As of the publishing of this article, presence of marine mammal vocalizations in the OOI BB hydrophone data remains unexplored. Previous studies have investigated the effects of air-gun experiments on marine mammal populations [58, 97, 79]. Since there is an airgun experiment conducted over OOI hydrophones and a large collection of marine mammal vocalizations, the OOI dataset provides the opportunity for further investigation into the effects of air-guns on marine mammals.

A rain event is shown in Fig. 2.5(f). The maximum rain rate during this spectrogram is 25 $\frac{\mathrm{mm}}{\mathrm{h}}$. Three consecutive events of strong wind are shown in Fig. 2.5(g). Peak wind speeds of those wind events reach values between approximately 13 - 15 $\frac{\mathrm{m}}{\mathrm{s}}$. Rain rates and wind speeds were obtained from surface buoys located in the vicinity of the hydrophones. [124] and [126] explore effects of rain and wind on the ambient sound using the OOI dataset.

Fig. 2.5(h) shows the eruption of the Axial Seamount volcano in April of 2015. Studies about the 2015 Axial Seamount eruption using OOI data include [17, 99, 171]. The average spectral density for April 24 between 07:30 and 10:00 UTC and between 1 and 90 Hz is 96.739 dB relative to $\frac{\mu Pa^2}{Hz}$. Using spherical spreading and the location of the fissures as reported by [99], the source level of the volcano for this frequency band and time segment is estimated to be 184.9 dB relative to $\frac{\mu Pa^2}{Hz}$. Fig. 2.5(i) shows a 6.2 magnitude earthquake that occurred 319 km from the Central Caldera hydrophone[‡]. The earthquake was located at (43°38′41.64″ N and 127°36′11.16″ W) and occurred at 9:31:47 UTC.

The OOI hydrophone dataset contains many diverse acoustic features that are observable due to its wide frequency range and spatial distribution. Future investigations that could take advantage of the features outlined here are discussed in more detail in section 2.8.

2.4 Median spectral level time series

In order to investigate long-term trends in the acoustic environment sampled by the OOI hydrophones, long-term median time-series for different spectral bands were investigated. Fig. 2.6 shows the times series of the monthly median spectral levels in the 100 Hz, 500 Hz, and 5 kHz one-third octave bands for the four broadband (BB) hydrophones. Fig. 2.7 shows the time series of the monthly median spectral levels in the 20 Hz and 50 Hz one-third octave bands for all five low frequency (LF) hydrophones. Median averaging is used for all time series plots to mitigate the effects of outliers such as the seismic reflection survey or axial seamount volcanic eruption. Additionally, 25th and 75th percentiles are plotted as shaded regions to communicate the range of possible values for a given month.

None of the BB median spectral level time series shows a significant seasonal pattern.

[‡] Earthquake data from https://ds.iris.edu/ieb

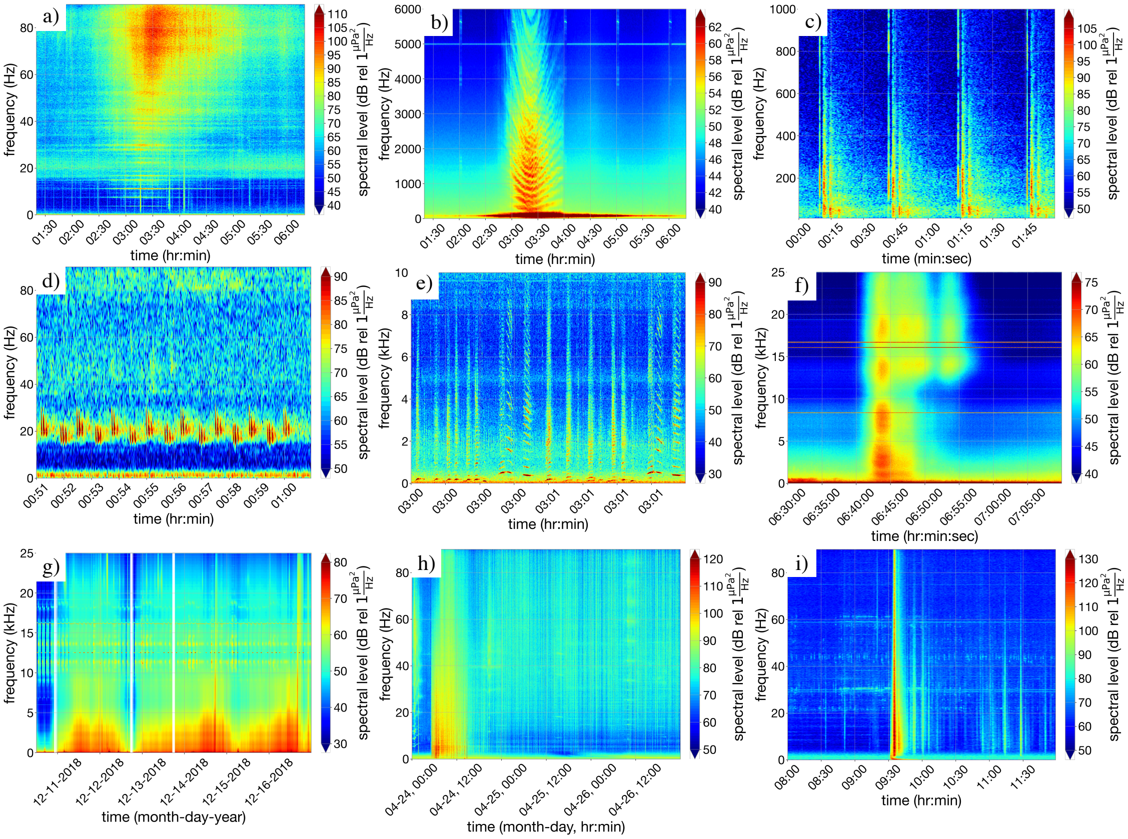

Figure 2.5: Spectrograms of notable acoustic features in the OOI dataset. Color scales vary between spectrograms. (a) spectrogram of a cargo ship passing within 5 km of the Axial Base low frequency (LF) hydrophone on June 5, 2016. (b) Same ship event recorded with the Axial Base broadband (BB) hydrophone. (c) Shots of an air-gun recorded on July 20, 2019 at 12:00 UTC [113]. (d) Fin whale vocalizations recorded by Axial Base seafloor LF hydrophone on December 15, 2016. (e) Marine mammal vocalizations recorded by the Oregon Offshore BB hydrophone on January 12, 2019. (f) a rain event recorded by the Oregon Offshore BB hydrophone on May 20, 2016 (peak rain rate: 25 $\frac{\mathrm{mm}}{\mathrm{h}}$), (g) a wind event recorded by the Oregon Offshore hydrophone on December 10-16, 2018 (peak wind speed: 13 - 15 $\frac{\mathrm{m}}{\mathrm{s}}$). (h) the eruption of the Axial Seamount volcano on April 24-26, 2015, recorded at the Axial Base seafloor LF hydrophone (i) a 6.2 magnitude earth-quake that occurred 319 km from the Central Caldera hydrophone on August 22, 2018

Linear trend lines were not computed for the BB hydrophone median time-series, because there is currently not enough data for an accurate estimate. Additionally, the large changes in spectral levels at the lower frequencies are concerning and potentially point to calibration issues with the hydrophones. Issues with calibration are discussed further in section 2.8. Most previous studies analyzing long-term ocean sound time series focus on frequencies well below 100 Hz. The few studies that have compared ambient sound levels at higher frequencies (typically 100 - 500 Hz) over multiple decades found that spectral levels in this frequency range remain largely constant over time [21, 80], which is consistent with our observations at 5 kHz.

In the LF time series plots, the large seasonal fluctuations in the 20 Hz band are due to the seasonal vocalizations of local fin whales. This seasonal variation was previously observed in [4]. Linear trend lines for the two spectral bands are reported. It should be noted that, due to the variation of ambient sound visualized by the 25th and 75th percentiles and the shorter time of six years that is analyzed, the slopes reported do contain error. Sound levels in the 20 Hz band for the Axial Base, Central Caldera, and Southern Hydrate locations see small increases over the six years with a linear slope of $0.34\,\frac{\mathrm{dB}}{\mathrm{yr}}$, $0.63\,\frac{\mathrm{dB}}{\mathrm{yr}}$, $0.64\,\frac{\mathrm{dB}}{\mathrm{yr}}$ respectively. The Eastern Caldera and Oregon Slope hydrophone locations see large changes in linear trends of $1.8\,\frac{\mathrm{dB}}{\mathrm{yr}}$, and $-1.1\,\frac{\mathrm{dB}}{\mathrm{yr}}$ respectively.

Energy in the 50 Hz band has contributions primarily from shipping noise [4, 169], and might also contain some fin whale vocalizations [133]. The 50 Hz trend line slopes for the Axial Base, Central Caldera, Eastern Caldera, Oregon Slope, and Southern Hydrate are $-0.57\,\frac{\mathrm{dB}}{\mathrm{yr}}$, $-0.055\,\frac{\mathrm{dB}}{\mathrm{yr}}$, $0.35\,\frac{\mathrm{dB}}{\mathrm{yr}}$, $-1.1\,\frac{\mathrm{dB}}{\mathrm{yr}}$, and $0.15\,\frac{\mathrm{dB}}{\mathrm{yr}}$. [4] reports a decade long trend in the 50 Hz band of $-0.26\,\frac{\mathrm{dB}}{\mathrm{yr}}$, for a hydrophone near 45 N (hydrophone h in their study). This trend was recorded by a hydrophone located on the continental shelf off of the coast of Oregon.

Our work suggests that, between 2015 and 2020, the linear trends of spectral levels in the 50 Hz band vary from location to location, but generally are around $\pm 0.5\ \frac{\mathrm{dB}}{\mathrm{yr}}$. The noted exception is the Oregon Slope location, which see's a large change of $-1.1\,\frac{\mathrm{dB}}{\mathrm{yr}}$. The spectral levels reports by [4] seem to be in a similar range for the different hydrophones that they study. However, these trend values should be considered within the context that the hydrophone calibration is imperfect and that hydrophone sensitivity drift for long-term deployments has been observed.

2.5 Distribution of Ambient Sound Spectral Levels

The distribution of ambient sound spectral levels can be described by spectral probability density functions (SPDFs) as initially proposed by [29] and formally defined by [87]. SPDFs are obtained from the long-term spectrograms of the broadband (BB) (Fig. 2.3) and low frequency (LF) (Fig. 2.4) hydrophones by computing histograms for each frequency bin. Plotting the histogram values as a function of frequency and spectral level gives the desired SPDFs, which are shown in Fig. 2.8 and Fig. 2.9 for the BB and LF hydrophones respectively.

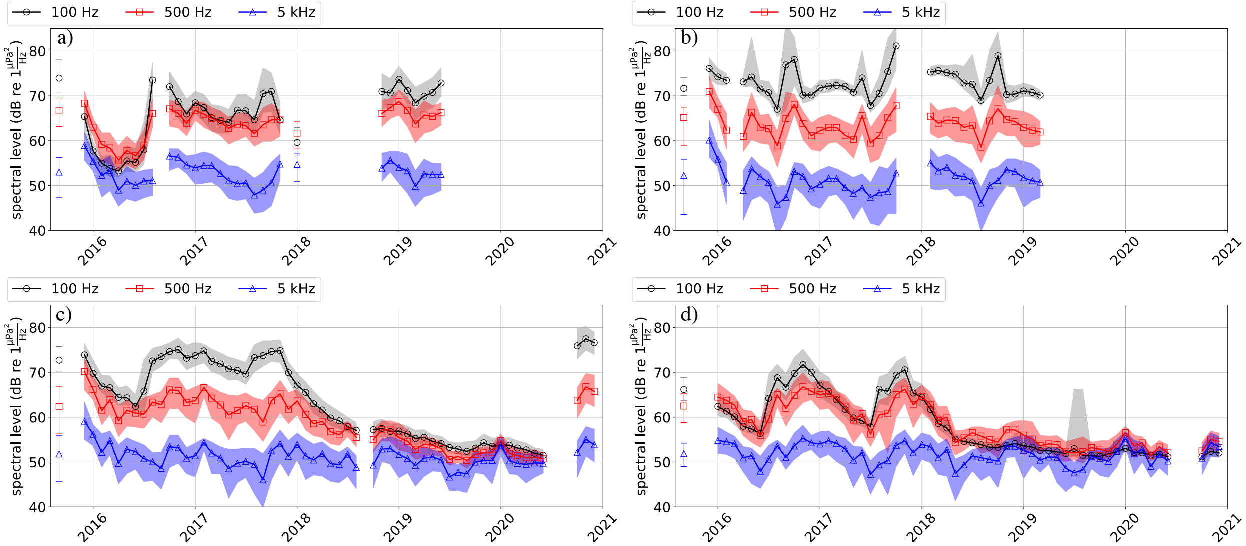

Figure 2.6: Time series of monthly average spectral levels for broadband hydrophones (a) Oregon Shelf, (b) Oregon Offshore, (c) Oregon Slope, and (d) Axial Base in three different one-third octave bands. Slopes of the regression lines are shown in parenthesis.

2.5.1 Broadband Hydrophones

The SPDFs for the Oregon Shelf, Oregon Offshore, Oregon Slope, and Axial Base location are shown in Fig. 2.8 along with various percentiles (black lines). A feature that all locations have in common is that spectral levels decrease with increasing frequency and the spread in spectral level (i.e., the difference between lowest and highest spectral level at a given frequency) is typically below 40 dB. However, the exact shape of the SPDFs and the trajectories of the corresponding percentiles differ significantly between the locations. The Oregon Shelf and Oregon Offshore percentiles have a similar trajectory as the wind noise spectral levels in Fig. 4 of [124]. This suggest that wind is the dominant factor in the general ambient sound. Other sound sources such as marine mammals and rain events can also impact the ambient sound distribution. However, as the SPDFs are generated from 15-min Welch median PSD estimates requiring a source to be present for at least 7.5-min to significantly effect the PSD estimate, we speculate that those sound sources have a rather small effect on the distribution.

For lower frequencies (below approximately 1 kHz) it is assumed that nearby ship passages and distant shipping activity have a significant effect on the SPDFs. While (infrequent) nearby ship passages would mainly effect the higher percentiles, the acoustic signature from distant shipping can also increase the spectral levels of the lower percentiles. This is most notable for the Oregon Offshore location where the 1st percentile spectral level around 50 Hz is about 15 - 20 dB higher compared to the other locations. Such a low frequency (LF) peak has

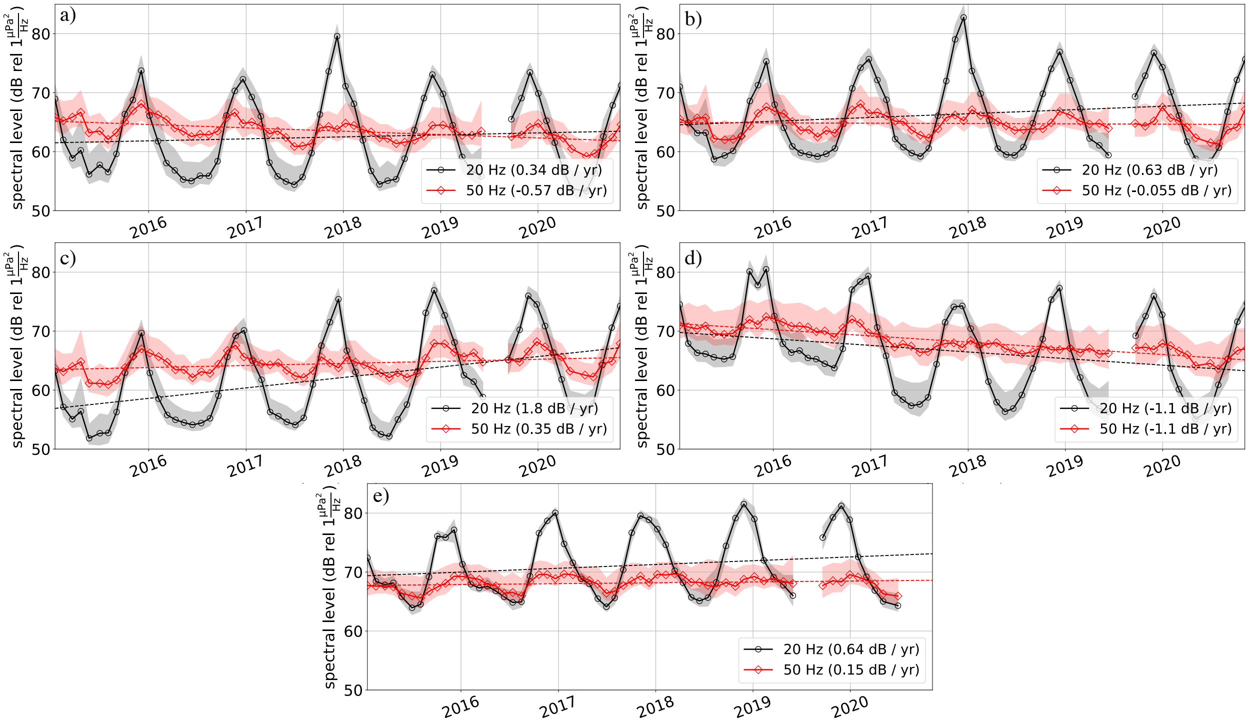

Figure 2.7: Six-year time-series computed for the 20 Hz one-third octave band and the 50 Hz one-third octave band for low frequency hydrophones. (a) Axial Base, (b) Central Caldera, (c) Eastern Caldera, (d) Oregon Slope and (e) Southern Hydrate. Linear trend slopes are given in parenthesis in the legend. Increased spectral levels for the Axial Base, Central Caldera, and Eastern Caldera hydrophones can be seen during the seismic reflection survey that occurred in 2019.

also been reported in other studies and is thought be a result of sound from distant shipping and high latitude winds that travels large distances via the deep sound channel[169, 3, 156, 6]. Therefore, a peak at low frequencies indicates that the location has access to the deep sound channel. While the Axial Base and Oregon Slope sound spectral levels show significant LF peaks only in the higher percentiles, the Oregon Offshore hydrophone exhibits a LF peak also in the lowest percentiles. This suggests that only Oregon Offshore has access to the deep sound channel year around, which is likely a result of the shape of the sound speed profile at this location.

2.5.2 Low frequency hydrophones

Fig. 2.9 shows the SPDFs for all six LF hydrophones along with various percentiles (black lines). Except for frequencies around 20 Hz, the SPDFs for all hydrophones are concentrated

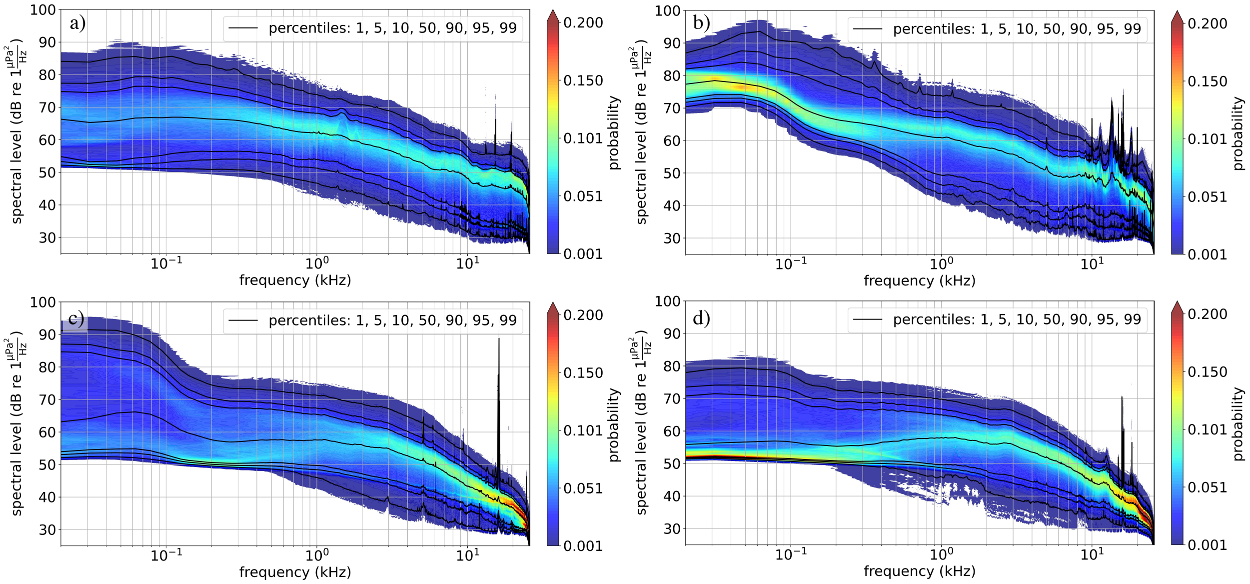

Figure 2.8: Spectral probability density function (SPDF) for broadband hydrophones (a) Oregon Shelf, (b) Oregon Offshore, (c) Oregon Slope, and (d) Axial Base.

around 60 - 70 dB with a spread (i.e., the difference between lowest and highest spectral level at a given frequency) of about 20 dB for most locations and frequencies. The more spread out densities around 20 Hz are caused by the seasonal fluctuations of local fin whale calls that can also be seen in the long-term spectrogram plots in Fig. 2.4. Furthermore, in July and August of 2019 there was a seismic reflection survey conducted directly over the Eastern Caldera, Central Caldera, and Axial Base hydrophones. This survey is also visible in Fig. 2.4. The seismic reflection survey is the cause of the 99th percentile having much larger values for these three hydrophones. If the seismic reflection survey is removed from the data, the 99th percentile for Axial Base, Central Caldera, and Eastern Caldera has similar values to the other two LF hydrophones.

It is noted that LF spectral levels at Oregon Slope are approximately 3 dB higher than BB spectral levels at the same location and comparable frequencies. We speculate that (1) differences in geometry of the ocean bottom and (2) the behavior of the Welch median estimator in the presence of outliers are responsible for this phenomenon. It can be shown that the Welch median estimator becomes increasingly biased when a larger percentage of periodograms are affected by outliers [123]. As the number of periodograms for each 15 min PSD estimate differs for the LF and BB data (see Section 2.2), a larger percentage of outliers in the LF PSD estimates could result in an overestimation of the LF spectral level. Additionally, imperfect hydrophone calibration may also bias the estimates.

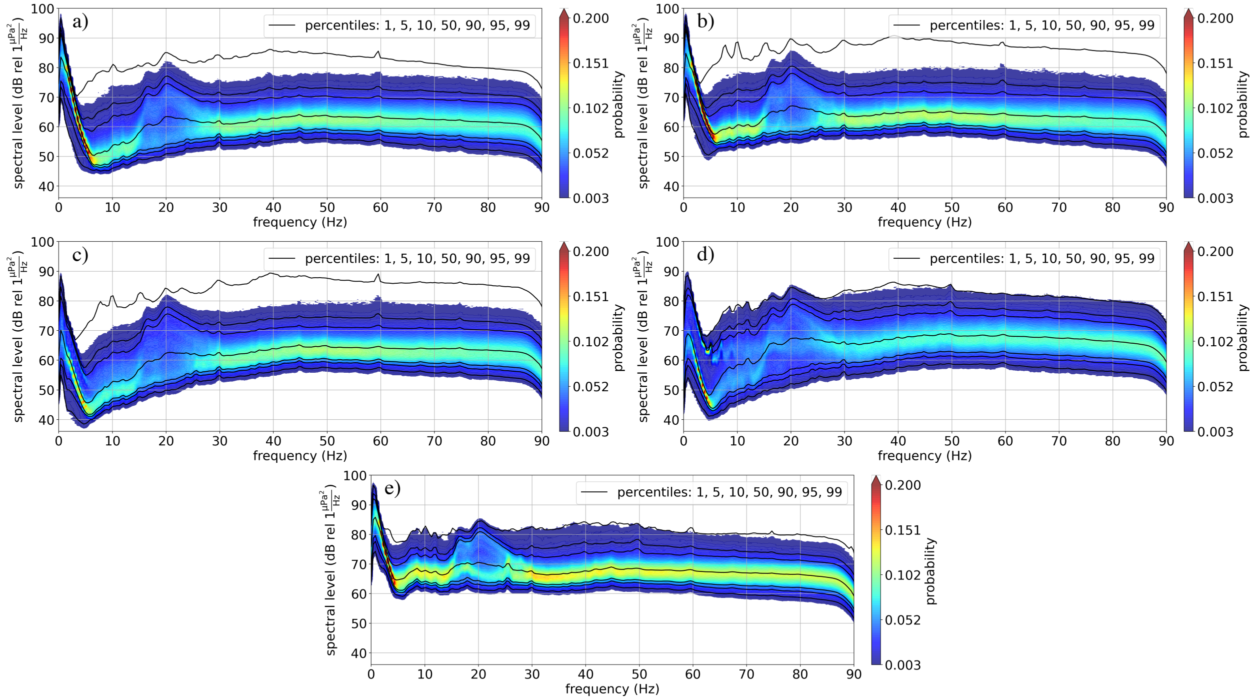

Figure 2.9: Spectral probability density function (SPDF) for low frequency hydrophones (a) Axial Base, (b) Central Caldera, (c) Eastern Caldera, (d) Oregon Slope and (e) Southern Hydrate.

2.6 Noise Floor

For frequencies between 1 - 800 Hz and depths of approximately 1 - 5 km, noise floor spectral levels (i.e., spectral levels in the absence of ships and marine life and when wind is low) in the eastern North Pacific have been recently analyzed by [8]. Instead of focusing on the spectral trajectory of the noise floor, the change in noise floor spectral levels change over time is explored. To do so, noise floor spectral levels are computed separately for each month during the measurement period that has a data coverage of at least 50 %. For this study, the noise floor is defined to be the 5th percentile of the SPDF which was defined in Section 2.5. That is, for each month the SPDF is calculated and the 5th percentile (i.e., noise floor) PSD is extracted. Afterwards, the noise floor PSDs were averaged into one-third octave bands and concatenated to obtain time series of the noise floor. The results for the broadband (BB) and low frequency (LF) hydrophones are shown in Fig. 2.10 and 2.11, respectively.

2.6.1 Broadband Hydrophones

Fig. 2.10 shows the noise floor time series for the 100 Hz, 500 Hz, and 5 kHz one-third octave bands at all four BB locations. One can observe that the trajectory of the noise floor time series generally follows the trajectory of the mean spectral level time series in Fig. 2.6. That is, the noise floor remains approximately constant for Oregon Offshore and the 5 kHz band at Oregon Shelf, Oregon Slope, and Axial Base. On the other hand, an increase (decrease) in noise floor can be observed for 100 Hz and 500 Hz at Oregon Shelf (Oregon Slope and Axial Base). Furthermore, no clear seasonal pattern, especially with a period of one year, can be observed. On average, noise floor spectral levels are lower than median spectral levels by about 4.4 dB, 7.9 dB, and 11 dB, at 100 Hz, 500 Hz, and 5 kHz, respectively. While those results can serve as a starting point to analyze the noise floor in the northeast Pacific Ocean, more data is necessary to draw better conclusions. Fortunately, the OOI will provide more BB hydrophone data in the upcoming years, which, together with the data shown in this work, can be used to obtain more definitive results.

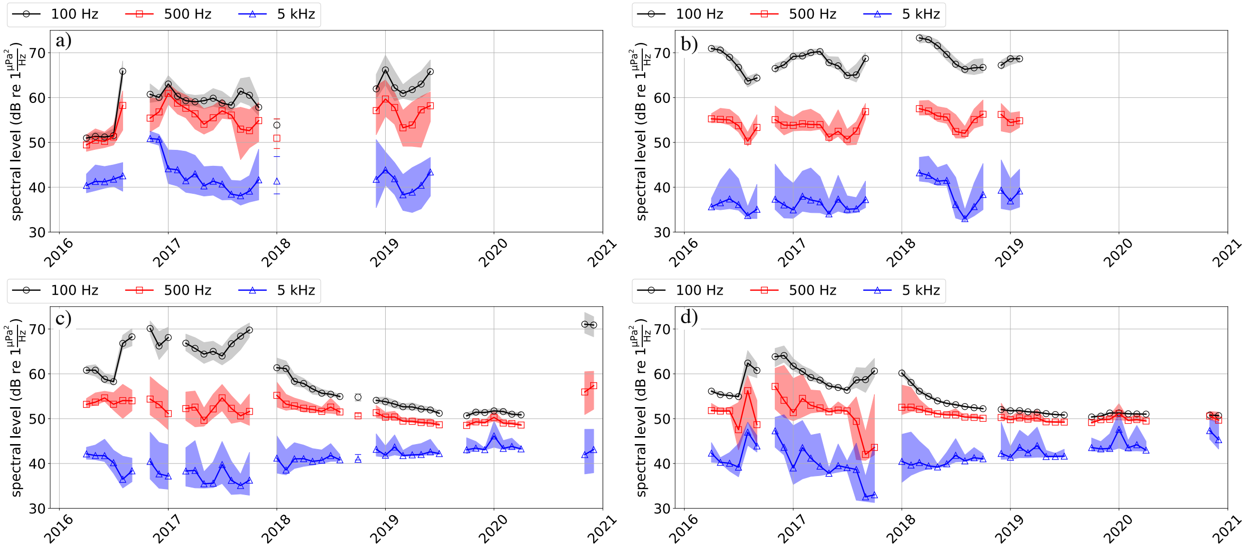

Figure 2.10: Time series of monthly noise floor for broadband hydrophones (a) Oregon Shelf, (b) Oregon Offshore, (c) Oregon Slope, and (d) Axial Base. The noise floor is defined as the 5th percentile of the SPDF in every given month of the measurement period that has at least 50 % data coverage. If a month has less than 50 % data coverage, no noise floor spectral level is computed resulting in a gap in the time series.

2.6.2 Low frequency hydrophones

Fig. 2.11 shows the noise floor time series for the LF hydrophones. The 20 Hz band still contains the primary fluctuations due to seasonal fin whale vocalizations. This indicates that when fin wales are present, they dominate the ambient sound by vocalizing throughout the entire time. The noise floor in the 50 Hz one-third octave band on the other hand, stays roughly constant around 60 dB with only weak seasonal fluctuations. Furthermore, some locations show weak seasonal trends in the 20 and 50 Hz one-third octave band. Those trends generally follow the pattern of the median spectral level time series in Fig. 2.7. That is, while spectral levels increase over time for the Axial Base, Central Caldera, Eastern Caldera, and Southern Hydrate, they decrease at the Oregon Slope.

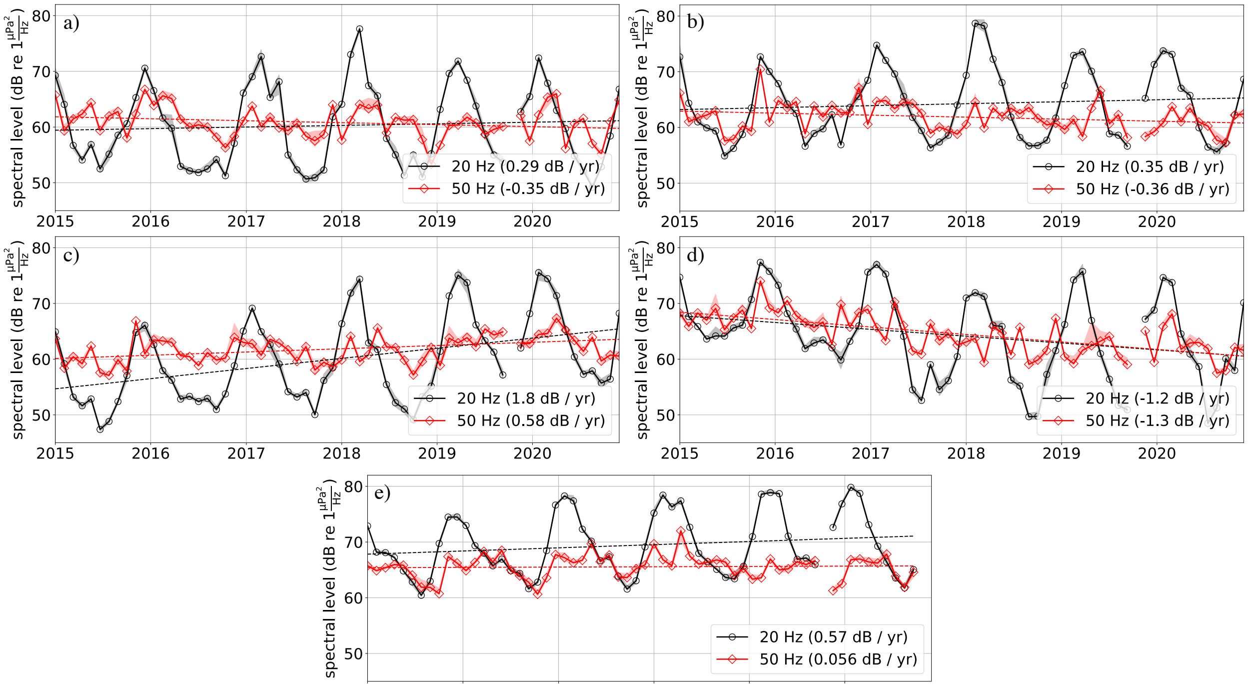

Figure 2.11: Time series of monthly noise floor for low frequency hydrophones (a) Axial Base, (b) Central Caldera, (c) Eastern Caldera, (d) Oregon Slope, and (e) Southern Hydrate. The noise floor is defined as the 5th percentile of the SPDF in every given month of the measurement period that has at least 50 % data coverage. If a month has less than 50 % data coverage, no noise floor spectral level is computed resulting in a gap in the time series.

2.7 Hydrophone spectrum correlations

Time series extracted from the long-term spectrograms in Fig. 2.3 and 2.4 are used to compute cross-correlations between different hydrophones. To do so, a time series at a single frequency bin from one hydrophone is correlated with the time series at the same frequency of another hydrophone. This process is repeated for all frequency bins and hydrophone combinations. The resulting frequency dependent cross-correlations averaged into one-third octave bands (using median averaging to mitigate the effect of outliers) are shown in Fig. 2.12. The distances between hydrophone pairs are given in parenthesis. Additionally, power spectrum cross covariance matrices are shown for the LF hydrophones locations in Fig. 2.13.

2.7.1 Broadband Hydrophones

Fig. 2.12 shows that the correlation of ambient sound levels between the different broadband (BB) hydrophones is highly frequency dependent. With the exception of the Oregon Slope - Axial Base combination, correlation values are usually highest between 1 - 10 kHz and increase with decreasing distance between the hydrophones. That is, the highest correlation for frequencies above 1 kHz can be observed between the Oregon Slope and Oregon Offshore hydrophone, which are separated by only 38 km. On the other hand, sound between Oregon Offshore and Axial Base as well as Oregon Shelf and Axial Base, which are separated by 411 km and 447 km, respectively, is less correlated. The question of which factors contribute the most to the cross-correlation curves in Fig. 2.12 is beyond the scope of this chapter. However, we speculate that a main contributor could be the (dis)similarity of wind conditions at different locations at the same time. It is known from [124] that spectral levels between 1 - 10 kHz are highly correlated to the wind speed and neighboring locations are more likely to have similar wind speeds at the same time.

For frequencies below 1 kHz, correlations are typically much lower than in the high frequency range. The only exception are the Oregon Slope and Axial Base hydrophone, whose correlation increases with decreasing frequency and assumes values above 0.6 for frequencies below 100 Hz despite a separation of more than 370 km. A possible explanation is that low frequency sound is able to propagate between these two locations without experiencing significant attenuation. As both hydrophones are located in depths of more than 2500 m, there could exists propagation paths that do not interact with the sea surface or only do so in a limited way, therefore resulting in less sound attenuation. Furthermore, the geometry of the seafloor at and between the two hydrophones may also crucially influence the sound propagation. However, investigating this behavior in more detail is beyond the scope of this chapter and left for future research.

2.7.2 Low frequency hydrophones

The cross-correlations for the low frequency (LF) hydrophones are shown in Fig. 2.12. Generally, the correlations increase with decreasing inter-hydrophone distance. High correlation values around 20 Hz can be traced back to the seasonal migration patterns of fin whales, which are also visible in the long-term spectrograms in Fig. 2.4 for all five LF locations. For frequencies at and below 1 Hz, the high correlation values can be attributed to the occurrence of microseisms that often effect the sound levels at multiple hydrophones at the same time. Between those frequency bands with high inter-hydrophone correlation, the correlation values dip and reach a minimum around 3 - 4 Hz for most hydrophone combinations. This suggest that there are no ubiquitous sound sources in this frequency range. As for the BB hydrophones, a more thorough analysis of the inter-hydrophone sound correlation remains a topic for future investigation.

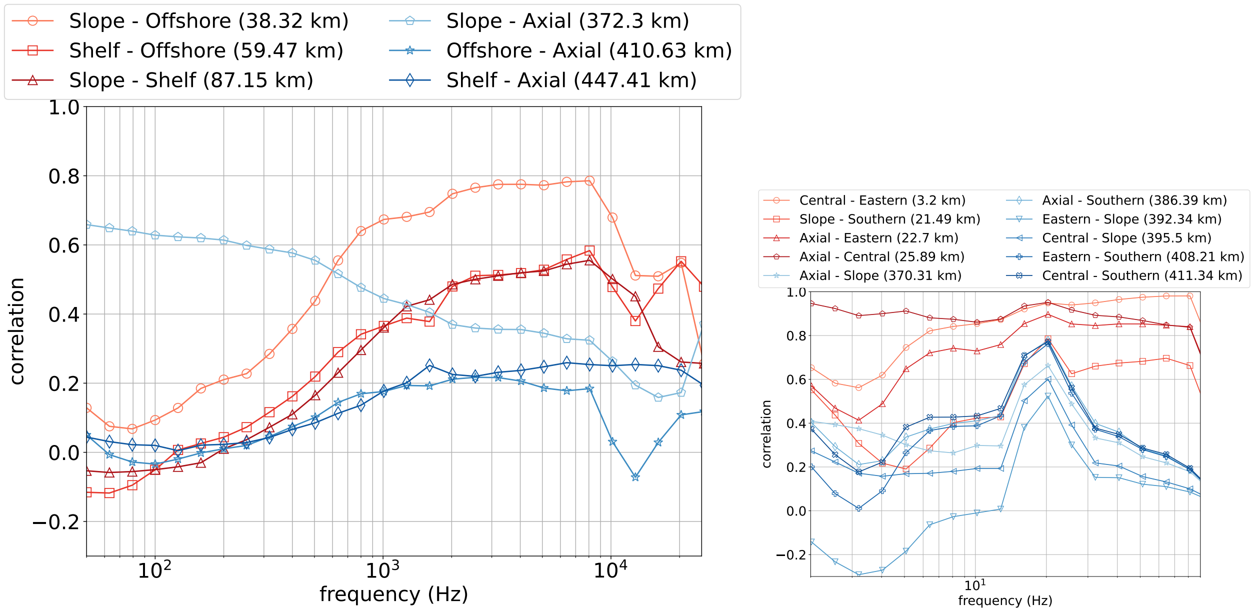

(a) (b)

Figure 2.12: Frequency dependent inter-hydrophone cross-correlation of ambient sound levels averaged into one-third octave bands for (a) broadband and (b) low frequency hydrophones. Hydrophone combinations separated by less than 100 km are colored in red. If the distance is larger, a blue coloring is used. Generally, the correlation increases as the inter-hydrophone distance decreases.

2.7.3 Power spectrum covariance matrix

In order to investigate the correlation between different frequency bins in the power spectral densities (PSDs) over the six years of data analyzed, the power spectrum density covariance matrices are computed and shown in Fig. 2.13. There is a large correlation between 15 - 25 Hz, which is expected due to fin whale vocalizations. Additionally, other frequencies don't seem to be correlated to the 20 Hz frequency band. This is likely explained by fin whale vocalizations dominating this frequency band and not vocalizing in other frequency bands. Frequencies between 40 - 90 Hz seem to have higher correlation which is expected due to shipping noise. Frequencies between 2 - 15 Hz have different levels of correlation depending on the location. The correlation in this frequency band could be caused by seismic or volcanic activity. Notably, the correlations in this frequency band are different for the Axial Base, Central Caldera and Eastern Caldera hydrophones which are located on the active Axial Seamount volcano, as compared to the Oregon Slope hydrophone and the Southern Hydrate hydrophones. There are several other notable features, which are not easily explained. There appear to be 'rays' of correlation with a slope not equal to one. These 'rays' are present in all hydrophones but are easiest to see in Fig. 2.13(d) and 2.13(e). These 'rays' indicate that sound levels at a single frequency are correlated with sound levels at a single, lower frequency. The correlation between single frequencies scales linearly, but not one to one. Additionally, there are diagonal lines just above and below the major diagonal for frequencies above 30 Hz. Further investigation into the power spectrum covariance matrices for different LF hydrophone locations is saved for future work.

2.8 Future Directions and Discussion

There are still many potential areas of research that can utilize the OOI data resources. Using some of the dataset features highlighted throughout this chapter, several areas of potential future investigation are discussed and several improvements that could be made to the OOI acoustic dataset are proposed.

Suggested improvements to OOI: The OOI hydrophone network provides a great opportunity for future development in the field of ocean acoustics. The author's would like to note several areas that would further the usefulness of this dataset for future consideration. ADCP pings contaminate a significant portion of the broadband data, and moving hydrophones to be farther away from these measurment devices could result in better quality data. Another major area of improvement that is needed from OOI is the calibration of the hydrophones. Documentation for hydrophone calibration is not easily available, and specific calibration sheets for individual LF hydrophones are not available. Future calibrations could also benefit long-term ambient sound research. The LF hydrophones are not calibrated below 2 Hz, but there appears to be useful information in the data that is present below 2 Hz. Additionally, re-calibrating the hydrophones over time could help long-term analysis compensate for calibration drift with time. Lastly, the addition of even more acoustic sensor types, such as directional arrays or distributed acoustic sensing, would allow for further scientific development using the OOI dataset.

Ship noise: In combination with ancillary datasets such as from the Automatic Identification System (AIS), the OOI low frequency (LF) and broadband (BB) hydrophone data

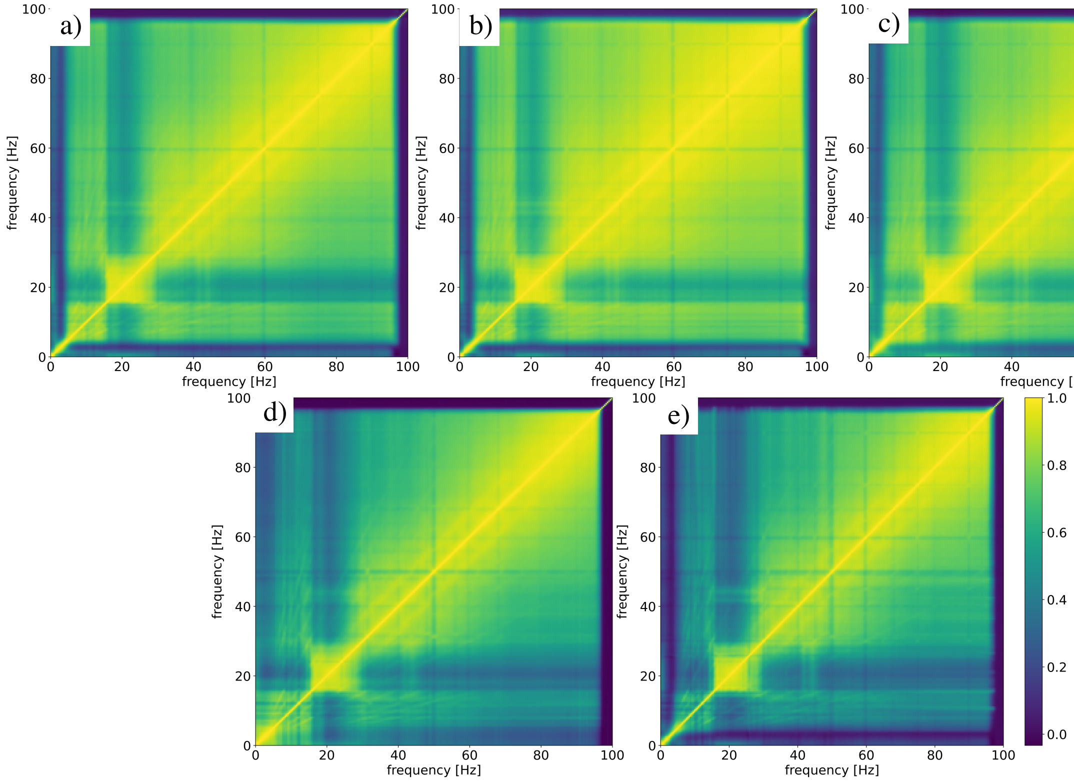

Figure 2.13: Power spectrum covariance matrix for low frequency hydrophones (a) Axial Base, (b) Central Caldera, (c) Eastern Caldera, (d) Oregon Slope and (e) Southern Hydrate.

can be used to study sound from commercial ships in greater detail. For example, the hydrophone data along with modern techniques from statistical and deep learning can be used to develop algorithms for ship classification and path tracking as shown by [98]. Furthermore, by comparing LF spectral levels associated with commercial shipping and other man made activity with past measurements such as from [4], the continuing impact of anthropogenic sources on underwater sound can be assessed and predictions for the future can be made. Additionally, the prevalence of ship passes in the data could provide the opportunity for further investigation into the feasibility of using ship passes for tomographic inversion.

Weather prediction: The OOI BB hydrophone data can be used to detect rain events and estimate wind speeds and rain rates from passive underwater acoustic recordings. Respective algorithms have been proposed by [76, 154], as well as more recent examples using machine learning [146, 148]. However, deep learning techniques have not yet been fully exploited for such tasks. In-situ wind and rain measurements at Oregon Shelf and Oregon Offshore can be used to evaluate existing algorithms developed using data at different locations, as well as to develop new deep learning algorithms for remote sensing of wind and rain as well as weather prediction applications.

Long-term analysis: As the OOI hydrophones will continue collecting data over the next years, the mean spectral levels and noise floor time series shown in this chapter can soon be extended to better assess long-term changes in ambient sound and noise floor levels. The amount of data in the OOI dataset can also be used for tasks such as time series forecasting with the goal of predicting future ambient noise levels. This has previously been studied by [1] using genetic algorithms on a small dataset collected in the Strait of Sicily, Italy. Expanding this approach to a larger scale using LF and BB OOI hydrophone data is a promising direction for future research. The low-frequency hydrophone calibration information is only available above 2 Hz. In future works, relative analysis similar to the analysis of [29] in combination with seismometers co-located with the LF hydrophones could be used to further study long-term trends of low frequency ambient sound that is below 2 Hz.

Linking to other ocean data: While we focus on hydrophone data in this chapter, the OOI provides a variety of other data products collected at the air-sea interface, water column, and seafloor. Therefore, the effects of environmental parameters such as temperature, salinity, conductivity, and others on the acoustic data can be studied using OOI data. Additionally, OOI acoustic data could be used in tandem with other ocean observatories data such as the Ocean Networks Canada (ONC) Neptune observatory [§], which also studies the north-east Pacific.

Noise Interferometry: Ambient noise interferometry is the method of using ambient sound to estimate the time domain greene's function between two points. Chapter 3 demonstrate the viability of using ambient noise interferometry between the Eastern Caldera and Central Caldera LF hydrophones to resolve direct and multi-path acoustic arrivals between the two hydrophones. Further developments using these hydrophones for ambient noise interferometry are presented in chapters 4 and 5 The viability of ambient noise interferometry is very dependent on the specific acoustic environment of the two hydrophones [134]. Since the OOI hydrophone network contains many different hydrophones with differing environments, the effects of the environment on ambient noise interferometry could be experimentally explored in greater detail using the OOI dataset.

Marine Mammals: As highlighted in section 2.3.1 and also in Figs. 2.4 and 2.5, marine mammal vocalizations are present throughout the entire OOI dataset. [167] have already used seismic data to study fin whale vocalizations in the region. The OOI dataset could be utilized to further investigate the behaviors of different marine mammal species in the north-east Pacific. Given the size of the OOI acoustic dataset, and the presence of marine mammal vocalizations throughout, this dataset could also lend itself to machine learning methods for learning more about marine mammal populations and the meanings of their vocalizations.

Spectral Correlation: In section 2.7, the inter-hydrophone cross-correlation for different spectral levels is explored. Explanations for the different correlations that are observed

---

[§] `https://www.oceannetworks.ca/`

are still largely unknown. Further investigation could help explain some of the correlations that are observed. Moreover, by computing power-spectrum covariance matrices for each individual hydrophones, it would be possible to study the frequency ranges of characteristic noise sources such as ships or marine mammals. Additionally, analyzing spectral correlations in time could potentially reveal time-delayed correlations of different spectral bands. This technique could possibly be used to study fin whale migration patterns.

Other machine learning applications: As machine learning tools become more popular and more powerful, the need for large amounts of data continues to grow. OOI provides a significant opportunity for developing machine learning tools within the field of ocean acoustics. Many specific areas that machine learning could be applied have been mentioned above. However, one of the largest limiting factors for machine learning in ocean acoustics is acquiring labeled datasets. Oftentimes labelling data in ocean acoustics is non-trivial and requires expert knowledge. A potential future area of investigation in machine learning for ocean acoustics is using unsupervised machine learning to learn dimension reductions for ambient sound, which could be used to learn complex patterns within data. This technique could then be used for applications such as ambient sound annotation, or remote sensing. This endeavor requires a large amount of data in order to be successful. Given the large size of the OOI acoustic dataset, it could potentially lend itself well to this type of investigation.

2.9 Conclusion

In this chapter, we have presented an overview of the publicly available OOI dataset. We have highlighted prominent features that are within the dataset. Long-term trends in the 50 Hz band, median spectral levels were found to vary significantly from hydrophone to hydrophone. The 20 Hz band showed strong seasonal patterns as previously observed by [4] and also had varying linear trends depending on the hydrophone site. Long-term trends in the 100 Hz, 500 Hz, and 5 kHz were found to vary significantly between hydrophone locations as well. Spectral probability density functions were used to show that ambient sound distributions highly depend on frequency band and location. Long-term noise floor analysis reveals that the trends observed in the median spectral level time series are similar to the trends for the 5^{th} percentile in the spectral bands that are investigated. Inter-hydrophone spectral correlations reveal that for broadband hydrophones, spectral levels between 1 kHz and 10 kHz show the highest level of correlation between hydrophones. Low frequency hydrophones see highest levels of inter-hydrophone correlations below 1 Hz and at 20 Hz due to microseisms and fin whale vocalizations respectively. In general, correlation between hydrophones is stronger for shorter distances. Lastly, potential future areas of investigation using the OOI dataset given the acoustic features presented throughout this work are discussed.

Chapter 3

LONG-TERM NOISE INTERFEROMETRY ANALYSIS IN THE NORTHEAST PACIFIC OCEAN

Abstract

Long-term noise interferometry analysis is conducted between 6 years (2015-2020) of data using two hydrophones on the Ocean Observatories Initiative Cabled Array. The two hydrophones are separated by 3.2 km and are bottom-mounted at 1500 m. We demonstrate the ability of ambient noise interferometry to reliably detect multi-path arrivals in the deep ocean from bottom-mounted hydrophones. An analysis of the multi-path arrival peak emergence is presented, as well as long-term trends of the signal-to-noise ratio of the arrival peaks. Lastly, it is shown that long-term ambient noise interferometry provides the opportunity for monitoring directional, coherent ambient sound such as the fin whale chorus. [*]

3.1 Introduction

Ambient noise interferometry is a well-developed method for passively estimating the time domain Green's function (TDGF) using ambient sound. It was first demonstrated by [163] and has been further developed by many other works in the field [164, 165, 116, 120, 117, 45, 47, 48]. Ambient noise interferometry has found many applications in seismology and oceanography. Some applications to seismology include the measurement of dispersion curves, characterizing basin resonance, estimating the source location of earthquakes, and estimating the surface wave velocity structure [7, 9, 31, 119]. Some applications to acoustic oceanography include measuring the ocean temperature, measuring ocean current velocities, and exploring time reversal techniques [38, 172, 13, 44, 54, 122].

Previous work in ambient noise interferometry has shown the possibility of estimating the TDGF in the shallow ocean [116, 12]. Noise interferometry has also been demonstrated

---

[*] An earlier version of this work has been published and is available as:
Ragland, J., Abadi, S., and Sabra, K. (2022). "Long-term noise interferometry analysis in the northeast Pacific Ocean," The Journal of the Acoustical Society of America, 151, 194–204. doi:10.1121/10.0009232

in the deep ocean by utilizing the Sound Fixing and Ranging (SOFAR) channel to measure the direct path [173]. Due to long-term measurement platforms like the Ocean Observatories Initiative (OOI), ocean ambient noise data has become more available in recent years. As a result, the opportunity to use this data along with ambient noise interferometry for global oceanographic monitoring is extremely promising. The configuration of hydrophones for these long-term measurement platforms usually include sparse arrays of bottom mounted hydrophones in the deep ocean, which have not been extensively investigated for applications in ambient noise interferometry. Specifically, multi-path arrivals in the deep ocean have not previously been distinguished using ambient noise interferometry. In this chapter, publicly available ambient noise data from bottom-mounted hydrophones in the OOI network will be used to estimate the TDGF. The feasibility of using ambient noise interferometry for a short range (3.2 km) and deep ocean (1500 m) to resolve multi-path arrivals will be demonstrated. Additionally, the quality of ambient noise interferometry for this specific hydrophone configuration and ambient noise source distribution will be quantified for six years of ambient noise data.

The TDGF estimate emerges from a noise cross-correlation function (NCCF), which consist of time averaged cross-correlations between the two receivers. The emergence of the TDGF in an NCCF can be intuitively explained by considering sound that travels through both hydrophones. Sound that is received by the first hydrophone, then propagates through the ocean between the two hydrophones, and is lastly received by the second hydrophone would produce a peak in the cross-correlation of the two signals. The location of this peak in the cross-correlation is the time it took the acoustic signal to travel through the ocean from the first hydrophone to the second hydrophone. Noise sources that contribute to these peaks are located in the endfire direction of the hydrophone array. If cross correlations are averaged together, contributions for sources not located in the end-fire direction of the two hydrophones are averaged out and the TDGF emerges in the NCCF [164, 120].

One of the primary contributors to ambient sound in the frequency band of 1 - 90 Hz is from shipping noise [152, 169], which originates near the surface of the ocean. It has been shown that with a spatially uniform surface distribution of sound sources, the derivative of the NCCF converges to an amplitude weighted TDFG [116, 120]. The TDGF can be approximated by Eq. 3.1, where τ is delay time, $C(\tau)$ is the NCCF, $D(\tau)$ is an approximation of the delta function and is dependent on the spectrum and spatial distribution of the ambient noise sources, and $G_{AB}(\tau)$ is the TDGF from node A to node B [12, 117].

$$\frac{\partial \mathrm{C}_{\mathrm{AB}}(\tau)}{\partial \mathrm{t}} \sim \mathrm{D}(\tau) \star [\mathrm{G}_{\mathrm{AB}}(\tau) - \mathrm{G}_{\mathrm{BA}}(-\tau)] \tag{3.1}$$

The emergence of the TDGF in the NCCF can be explained by acoustic signals from the same source physically passing through one hydrophone and then propagating through the ocean to the second hydrophone. [134] showed with simulation that the acoustic propagation environment plays a large role in whether a TDGF is discernible in an NCCF. Since the primary contributors to ambient sound in the frequency band of the experiment originate from the ocean surface, the sound contributing to the direct path propagation is likely from distant, surface sources. This has been demonstrated experimentally for hydrophones in the SOFAR channel [172]. Conversely, sound contributing to the emergence of multi-path acoustic arrivals originate from local surface sources with steep angles of propagation. This was demonstrated in the shallow ocean by using the coherent sound from a tropical storm [10]. This means that the sound sources contributing to the direct and multi-path arrivals are located in different places relative to the hydrophones. Therefore, the two main contributing factors to whether an experiment is suitable for direct and multi-path acoustic propagation measurement using ambient noise interferometry are if the acoustic propagation environment and the spatial distribution of coherent sound sources are favorable.

[12, 10] demonstrate the feasibility of measuring multi-path propagation paths between hydrophones in a shallow ocean environment. [172, 38, 122], demonstrates the feasibility of measuring the direct acoustic propagation in the deep ocean by utilizing the SOFAR channel. In this chapter, ambient noise interferometry will be explored for measuring direct, surface and surface-bottom reflected propagation paths for hydrophones located in the deep ocean (1500 m) and separated by ∼3.2 km. A study of the emergence of the TDGF will be presented and compared to previous theoretical and experimental results. The calculated NCCFs will then be stacked over six years and the effects on the NCCF stack from different occurrences in the ocean acoustic environment will be explored.

In section 3.2, the hydrophone environment will be described, the data processing methods used for ambient noise interferometry analysis will be discussed, and acoustic simulation of the environment will be presented. Section 3.3 analyzes the emergence of the TDGF in the NCCF, the long-term signal-to-noise ratio of different arrival peaks, and the long-term NCCF stack. Section 3.4 discusses several known occurrences in the ocean that are visible in the long-term NCCF stack as well as identifying unknown patterns that are present in the long-term NCCF stack. Lastly, section 3.5 summarizes the findings that are presented in this chapter as well as discusses the applications and future directions of this work.

3.2 Experimental Setup and Data Processing

In the following sections, the hydrophone geometries, acoustic environment, data processing methods and acoustic simulation will be presented.

3.2.1 Acoustic environment

Acoustic data from two hydrophones located on the Axial Seamount volcano were used for long-term noise interferometry analysis. These hydrophones are part of the OOI Cabled Array. The first hydrophone, referred to below as the *Central Caldera* hydrophone[†], is located at 45.95468 N, 130.00893 W and is on the seafloor at a depth of 1528 m. The second

---

[†] NSF Ocean Observatories Initiative Data Portal, https://ooinet.oceanobservatories.org Low-Frequency Acoustic Receiver (network:OO, station:AXCC1).Downloaded on 29 January 2021

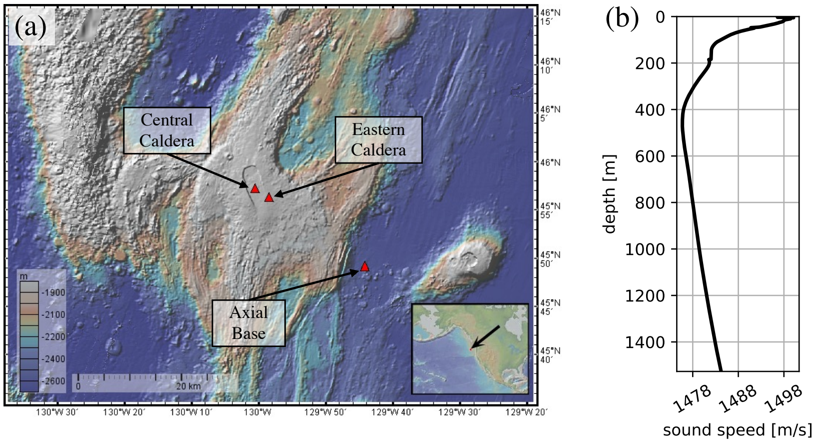

Figure 3.1: (a) Map of OOI Cabled Array sensor packages used in this chapter. Hydrophones used for noise interferometry are located at Eastern Caldera and Central Caldera sensor packages. CTD casts were used from the Axial Base sensor package. (b) 6 year average sound speed profile measured at the *Axial Base* location.

hydrophone, referred to below as the *Eastern Caldera* hydrophone[‡], is located at 45.93967 N, 129.97378 W and is on the seafloor at a depth of 1519 m. These two hydrophones are separated by 3.2 km. CTD data for acoustic simulation was used from the *Axial Base* ocean profiler, which is 24 km from the caldera hydrophones. A map of the hydrophones and CTD sensors, as well as a six-year average sound speed profile is shown in Fig. 3.1. Sound sources that contribute to the emergence of TDGF peaks are located in the endfire directions of the hydrophone array [70, 120]. Figure 3.2 shows the endfire directions ±10° for the *Central Caldera* and *Eastern Caldera* hydrophones. Acoustic data between January 2015 and December 2020 was used. Both hydrophones have a sampling rate of 200 Hz.

The ambient sound at both hydrophones was studied to better understand what sound sources contribute to the emergence of the TDGF estimate. Figure 3.3 shows the 6-year average power spectral density (PSD) for the *Central Caldera* and *Eastern Caldera* hydrophones, and common occurrences in spectrograms of ambient sound. The spectrograms and 6 year PSDs are created from 6 years of data where 15 minute, 512 point PSDs are estimated with the Welch median technique [125]. The spectrum of the ambient noise is fairly flat between 30 and 90 Hz. The peak at 20 Hz is due to seasonal vocalizations from fin whales [161]. The peak below 1 Hz is due to microseisms [166]. Individual ship passes can be seen throughout the 6 years of data with energy between approximately 5 and 90 Hz. Spectral levels above 90 Hz are attenuated by a physical filter on the two hydrophones. Seasonal fin whale vocalizations centered at 20 Hz are also present from approximately November to February.

[‡] NSF Ocean Observatories Initiative Data Portal, https://ooinet.oceanobservatories.org Low-Frequency Acoustic Receiver (network:OO, station:AXEC2).Downloaded on 29 January 2021

Figure 3.2: Endfire bearings ±10° for the *Central Caldera* and *Eastern Caldera* hydrophones.

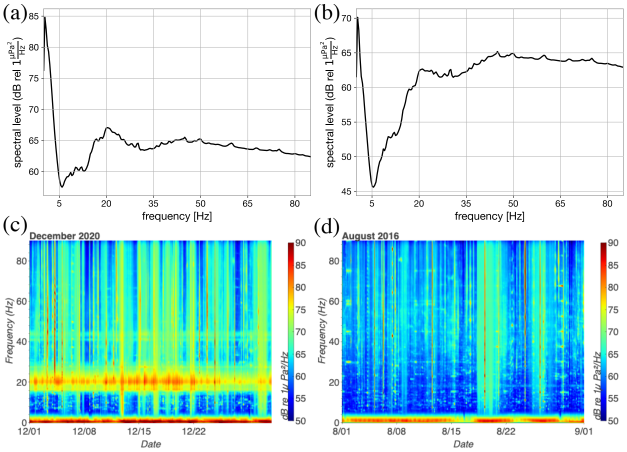

Figure 3.3: (a) 6-year PSD for the *Central Caldera* hydrophone. (b) 6-year PSD for the *Eastern Caldera* hydrophone. (c) Spectrogram containing fin whale vocalizations and shipping noise. Data is from *Central Caldera* and is from December 2020. (d) Spectrogram containing local shipping noise. Data is from *Central Caldera* and is from August 2016.

3.2.2 Acoustic data processing

The hydrophone data used for this chapter is archived at the Incorporated Research Institutions for Seismology Data Management System (IRIS)[§] and the Ocean Observatories Initiative (OOI) Data Portal. Acoustic data was downloaded from OOI and converted to a python ready format using the python package OOIPy [127]. The audio from each hydrophone was preprocessed to increase the coherent noise as much as possible and to decrease the effects of spurious events in the ocean. Different types of pre-processing are explored in depth in [55]. The pre-processing methods used in this chapter are similar to the techniques used in [173] and are described in detail below.

The uncalibrated audio data for each hydrophone was first broken up into 30 s segments (consisting of 6000 points) and filtered between 1 and 90 Hz using a 4th order, zero-phase Butterworth filter. A window length of 30 s was chosen to include relevant arrival times. The signals were then clipped to 3 times the standard-deviation of the signal for a given hour of audio recording to help mitigate the negative effects of spurious events on the emergence of the TDGF estimates. Lastly the individual signals were frequency whitened. To frequency whiten the signals, the time domain signal was windowed with a Hann window and then the 6000 point discrete Fourier transform was computed. The magnitude of the signal spectra is replaced with the magnitude response of an 8th order Butterworth filter (the same magnitude response as the filter used previously), and the inverse discrete Fourier transform of the signal is then computed. This preserves the phase information of the signal but makes the magnitude response flat for all relevant frequency. The pre-processing methods are outlined in Fig. 3.4, along with 30 seconds of time data before and after pre-processing. The preprocessed signals from the Central Caldera and Eastern Caldera hydrophone are then cross correlated, resulting in a 60 s, 11,999 point signal. These 60 s long correlations are then average together and normalized in amplitude to create an NCCF. Averaging times will be discussed in section 3.3.1.

3.2.3 Acoustic Simulation

Acoustic propagation between the *Eastern Caldera* hydrophone and the *Central Caldera* hydrophone was simulated using Kraken [104]. CTD data from the *Axial Base* location ($\sim$ 20 km from the caldera hydrophones) was used to create a 6 year average sound speed profile (see Fig. 3.1(b)). Studying the seasonal fluctuations of arrival times is left for future work.

Due to the short range between the two hydrophones, peak spreading due to modal dispersion is negligible for the simulated TDGF. Therefore, a single arrival time is estimated to quantifying the different arrivals. The arrival time is found by taking the argmax of each successive peak and using quadratic peak interpolation to get sub-time-bin resolution [136]. Table 3.1 shows the simulated arrival times for the first 4 propagation paths. To succinctly reference different TDGF peaks, the following naming convention will be adopted throughout

---

[§] http://ds.iris.edu/gmap/

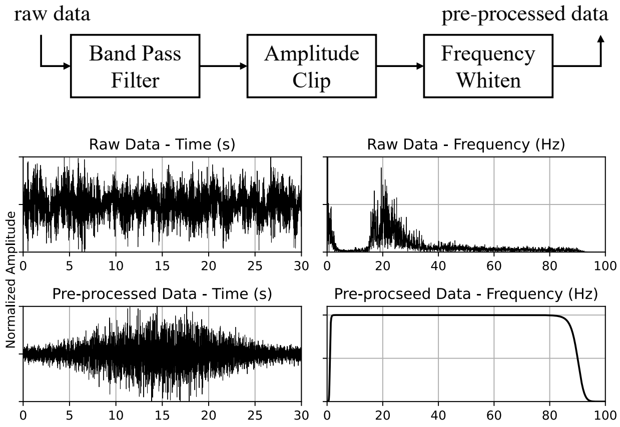

Figure 3.4: Block diagram of the pre-processing methods. A 30 s section of data is shown before and after pre-processing in the time and magnitude frequency domain

Table 3.1: Simulated arrival times between *Central Caldera* and *Eastern Caldera* and the number of surface and bottom reflection for each propagation path.

Path Label	Surface Reflections	Bottom Reflections	Simulated Arrival Time (s)
d	0	0	2. 142
s1b0	1	0	2.959
s2b1	2	1	4.620
s3b2	3	2	6.473

this chapter. Each peak will have a name code of sXbY, where X corresponds to the number of surface reflections and Y corresponds to the number of bottom reflections. For NCCF peaks, A or B will be added to the end to designate a lag or lead peak respectively. For the direct path peak observed in the NCCF (see sections 3.3.1) the code dA will be used.

3.3 Results

In the following sections, TDGF emergence, TDGF SNR, and the long-term NCCF stack is presented.

3.3.1 Time domain Green's function emergence

Figure 3.5 shows a 6-year average NCCF and the simulated arrival times given in table 3.1. The peaks that are seen in the NCCF match the simulated arrival times. The negative time, or lag section, of the NCCF corresponds to acoustic propagation from *Central Caldera* to *Eastern Caldera*, and the TDGF peaks emerge from sound sources located in the endfire axis that is pointed towards Alaska (Fig. 3.2). The positive delay, or lead, section of the

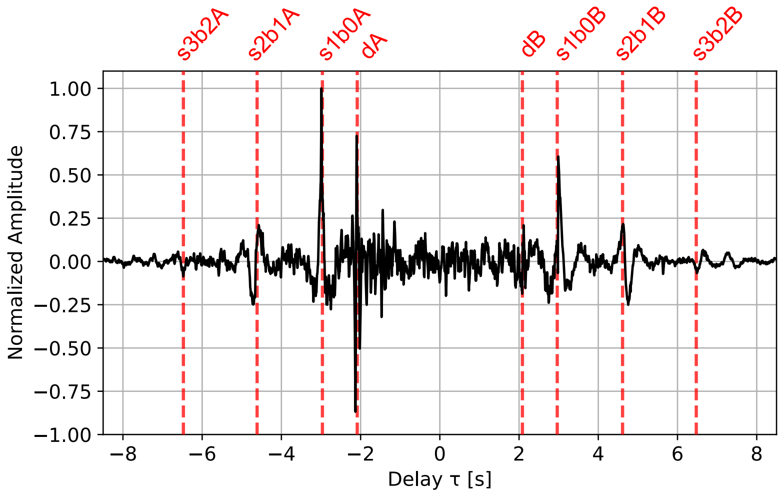

Figure 3.5: 6 year average NCCF. Dashed lines indicate simulated arrival times given in table 3.1. From left to right, the simulated arrival times shown correspond to s3b2A, s2b1A, s1b0A, dA, dB, s1b0B, s2b1B, s3b2B.

NCCF corresponds to acoustic propagation from *Eastern Caldera* to *Central Caldera*, and the TDGF peaks emerge from sound sources located in the endfire axis that is pointed towards the western coast of the United States (see Fig. 3.2). The peaks at ±2.9 s correspond to an acoustic propagation path that reflects off of the surface of the ocean. The peaks at ±4.62 s correspond to peaks that reflect off of the ocean surface twice and off of the ocean bottom once. The peak at -2.1 s corresponds to the direct path. The presence of the lag direct path peak and the absence of a lead direct path peak is likely due to the distribution of distant coherent sound sources.

In order to study the TDGF emergence, NCCFs were averaged for every month of the 6 years of data availability, resulting in 72 different emergence realizations. Figure 3.6 shows the TDGF emergence for all 5 distinguishable propagation paths. SNR is defined in Eq. 3.2 [173], where $\mathbf{Cpeak}(\tau)$ is the user defined window containing a specific peak, and $\mathbf{C_{noise}}(\tau)$ is defined as a window of the NCCF that contains only noise. Specifically, for the NCCF between *Central Caldera* and *Eastern Caldera*, $\mathbf{C_{noise}}(\tau)$ is defined as the NCCF between -15 and -10 s, and the noise window is multiplied by the inverse of the auto-correlated Hann window to undo the windowing from pre-processing (section 3.2.2).

$$\mathrm{SNR} = 20 \cdot \log\left(\frac{\max(\mathrm{C_{peak}}(\tau))}{3 \cdot \mathrm{std}(\mathrm{C_{noise}}(\tau))}\right) \tag{3.2}$$

A logarithmic curve (3.3) was fit to the mean emergence for all five peaks and is shown in Fig. 3.6. $\mathrm{T_{avg}}$ is the averaging time in hours and T_0 and A are constants. Theoretical studies show that the emergence of the impulse response should follow Eq. 3.3 for $A = 10$ under

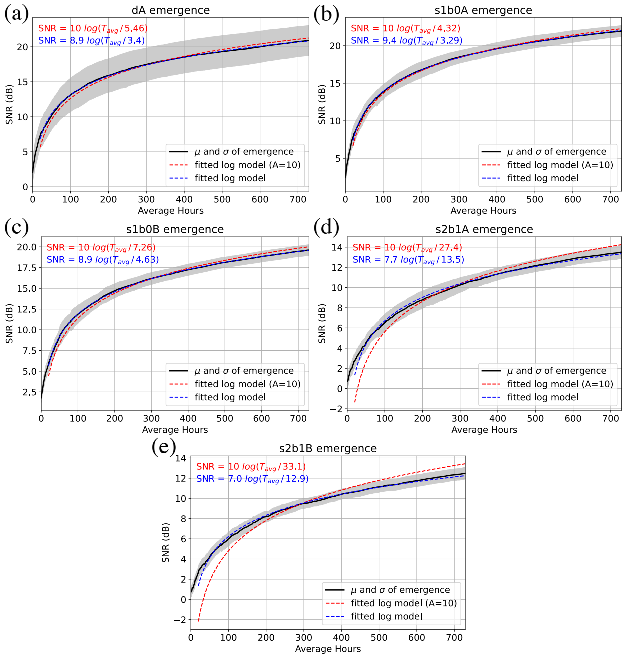

Figure 3.6: (a)-(e) TDGF emergence in the NCCF for specific acoustic propagation paths. The mean emergence is shown with the solid black line. The standard deviation of the emergence is shown with the shaded gray area. The red dashed line shows the least-squares fit curve for Eq. 3.3 and $A = 10$. The blue dashed line shows the least-squares fit curve for Eq. 3.3. The least-squared fit equations are given in the top left of each plot.

idealized conditions [165], because coherent energy grows like T_{avg}^2 and incoherent energy grows like T_{avg}. In Fig. 3.6, the least squares fit is given for both Eq. 3.3 and for Eq. 3.3 with A fixed at 10. [12] observe that with their data and hydrophone geometries, the emergence roughly follows Eq. 3.3 for $T_0 = 12$ hours and $A = 10$. For our data, hydrophone geometry, and sound distribution, T_0 values for *dA*, *s1b0A*, and *s1b0B* for $A = 10$ around 3.5 or 4.5 hours are observed. For the *s2b1* peaks and $A = 10$, T_0 values of around 30 hours are observed. However, the assumption of $A = 10$ does not seem to be particularly valid for the *s2b1* peaks with A values in the least-square fit being close to 7. This indicates that the ratio of coherent to incoherent noise actually grows like $T_{avg}^{0.7}$ instead of T_{avg} for the *s2b1* peaks.

$$\mathrm{SNR} = \mathrm{A} \cdot \log_{10}\left(\frac{\mathrm{T_{avg}}}{\mathrm{T_0}}\right) \tag{3.3}$$

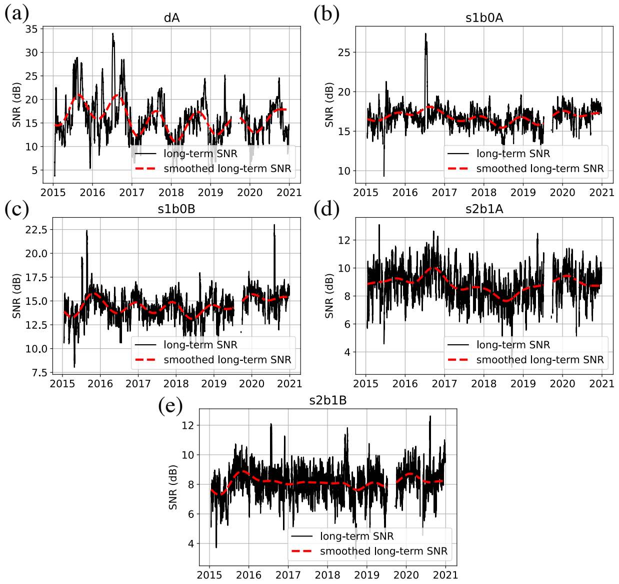

Figure 3.7: (a)-(e) Long-term SNR for every resolvable propagation path (solid line) and 150 day smoothed long-term SNR (dashed line) for 201 hours of averaging.

3.3.2 Long-term signal-to-noise ratio

Figure 3.7 shows the long-term SNR and the 150-day smoothed, long-term SNR for each of the 5 distinguishable peaks with 201 hours of averaging. There is a large seasonal pattern in the long-term SNR for the *dA* peak where larger SNR is seen in the summer months. This is caused by the seasonal 20 Hz feature described in section 3.3.4. This is also the cause of the larger standard deviation of the emergence shown in Fig. 3.6(a). The *s1b0* peaks show a small annual fluctuation in the long-term SNR (Fig. 3.7). This could be due to the changing ocean environment or seasonal fluctuation in coherent sound sources distributions.

3.3.3 Long-term NCCF stack

Figure 3.8(a) shows the long term NCCF stack between the *Central Caldera* and *Eastern Caldera* hydrophones. Each NCCF consists of 201 hours of average data comprised of the 100 hours before and after the recorded time. The average time was selected using Fig. 3.6. However, due to non-constant data availability, each NCCF sample does not necessarily contain exactly 201 hours of averaged ocean data. Figure 3.8(b) shows the actual number of average hours used for each sample. Using the TDGF emergence information in Fig. 3.6, a threshold of 100 average hours (shown by the dashed line) is set and any sample below this threshold is considered invalid. The color bars in Fig. 3.8 indicate events occurring in the ocean including the axial seamount volcano eruption, fin whale vocalizations visible in the spectrograms of hydrophone data and an airgun experiment that happened directly over the

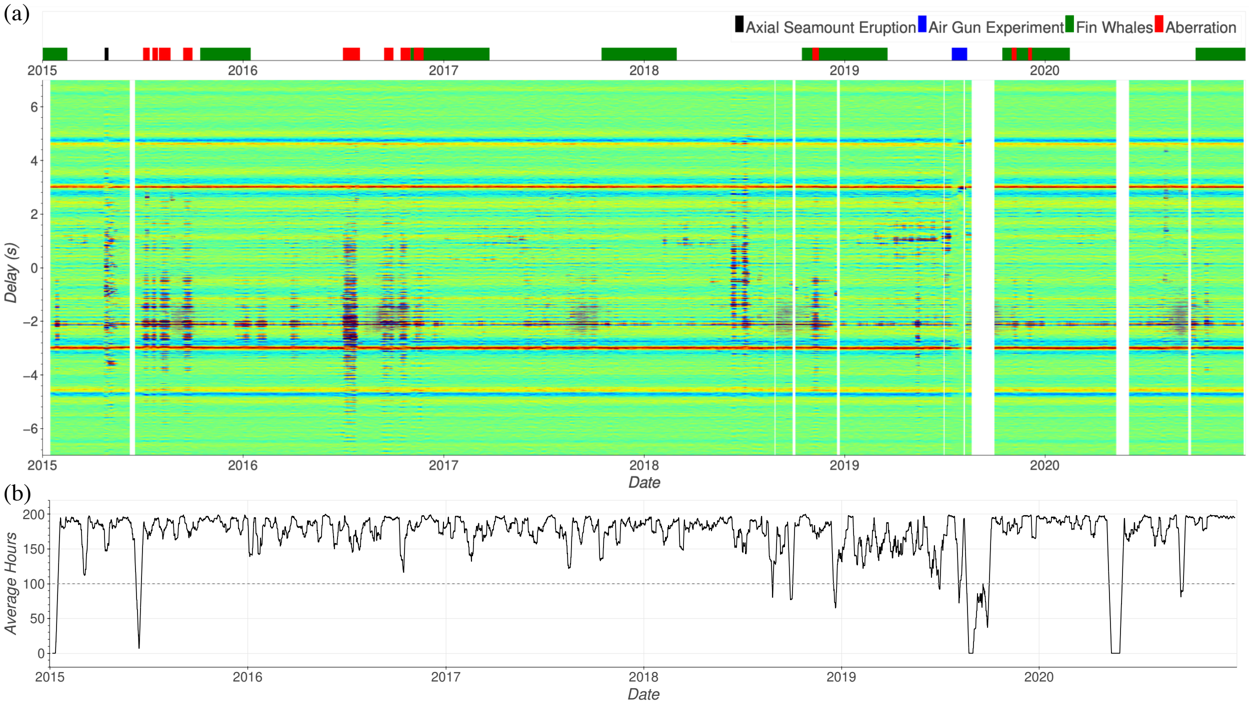

Figure 3.8: (a) 6 year NCCF stack with average time of 201 hours and stride of 1 hour. Single NCCFs are considered invalid and shown as white if there are less than 100 hours available for any given time during the six years. Important occurrences in the ocean are annotated above in color. (b) Plot of the number of available hours for any given NCCF sample and the valid NCCF threshold.

hydrophones.

3.3.4 Fin whale chorus

There is an annual feature in the long-term NCCF stack (Fig. 3.8) that is centered on the dA peak around -2 s. The feature is about 1 second long in delay time and is present for roughly five months every year. Figure 3.9 shows a slice of a single NCCF while the feature is present. The frequency content of this feature is narrow band and is centered at 20 Hz. Figure 3.10 shows the a spectrogram of the NCCF when the 20 Hz feature is and isn't present. The energy at 7 Hz is present year-round, but the 20 Hz energy is seasonal. Due to the seasonal nature of this feature and the fact that it is 20 Hz, it is most likely caused by fin whales.

Interestingly, the annual pattern of the 20 Hz feature in the NCCF and the presence of 20 Hz fin whale calls in the spectrograms of ambient sound don't perfectly line up. Figure 3.11 compares the spectrum time-series of the two hydrophones to the spectrum time-series of the NCCF stack in the 20 Hz, one-third octave band. The spectrum time-series of the

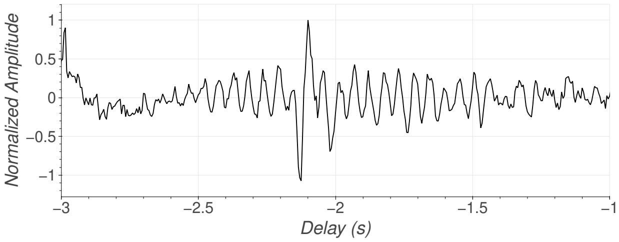

Figure 3.9: Section of single NCCF when 20 Hz feature is present at the dA peak (-2.1 s). This NCCF is from 09-01-2017 00: 00:00.

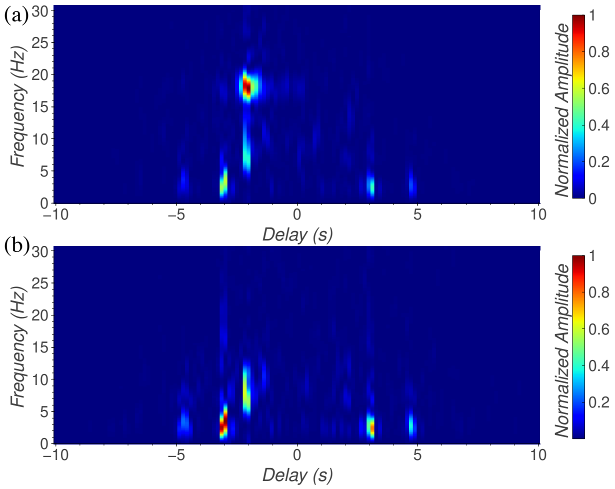

Figure 3.10: Spectrograms of NCCF when 20 Hz feature is present and not present. The spectrograms were calculated with a power spectral density estimate and the squared amplitude was normalized between zero and one. (a) Spectrogram of the NCCF when 20 Hz feature is present at the dA peak (-2.1 s). This NCCF is from 09-01-2017 00: 00:00. (b) Spectrogram of NCCF when 20 Hz feature is not present. This NCCF is from 01-01-2018 00: 00:00.

two hydrophones is created by taking the 601 hour median of 15 minute, 512 point PSD estimates and then averaging over the 20 Hz, one-third octave band. The NCCF time series is created by taking the discrete Fourier transform of the entire 601 hour average NCCF and then averaging over the 20 Hz, one-third octave band.

Our hypothesis to explain this difference in timing is that the fin whale calls that are visible in the spectrogram and the 20 Hz signal in the NCCF are caused by different acoustic phenomena that both originate from fin whales. Sound that contributes to the dA peak is propagating horizontally in the water column and is located in the end-fire direction of the two hydrophones that is pointed towards Alaska (Fig. 3.2). Due to the horizontal propagation of the sound, it is likely from distant sources. [85] document the presence of a fin whale chorus, in which the calls of many fin whales combine to a constant 20 Hz hum. In the fin whale chorus there are no discernible discrete fin whale calls. This distant chorus is believed to contribute to the 20 Hz energy in the NCCF stack, and is not clearly discernible in the spectrograms of ambient sound because it is buried in louder, local noise. When fin whale calls are visible in the spectrogram of ambient sound, individual calls are present in the signal and the calls likely originate from local fin whales. The pre-processing techniques outlined in 3.2.2 are specifically designed to attenuate components of the received signal that have a large amplitude relative to the rest of the signal and components that have a strong, narrow frequency band. Both of these characteristics are representative of the fin whale calls that are visible in the spectrograms of ambient sound. This is why the contributions of local fin whale vocalizations are not visible in the NCCFs. The 20 Hz energy in the long-term NCCF stack and in the spectrograms of ambient sound are both likely due to fin whales. However, the 20 Hz energy in the NCCF stack is likely due a distant fin whale chorus with a rough directionality pointed towards Alaska. The 20 Hz energy in the ambient sound are likely due to local fin whale calls, where individual calls from single whales are visible. Very little is known about fin whale migration patterns, but they have been documented migrating from higher latitudes in the summer to lower latitudes in the winter [91]. This movement would be consistent with the patterns seen in the NCCF, where the energy in the dA peak is present in the summer/fall months.

3.4 NCCF Features

Throughout the 6 years of the long-term NCCF stack, there are several notable occurrences in the NCCF stack that effect the quality of the TDGF estimate. Descriptions and explanations of some of these features are presented below.

Axial seamount volcanic eruption In April 2015, the Axial Seamount volcano that the hydrophones are located in erupted [171]. This eruption is clearly visible in the NCCF stack and is shown in Fig. 3.12. During the eruption, discrete peaks are visible in the NCCF that are between the two direct path delay times of ±2.1 s. This is likely due to the directionality of coherent arrivals of impulsive sound sources that were emitted from the fissures [171].

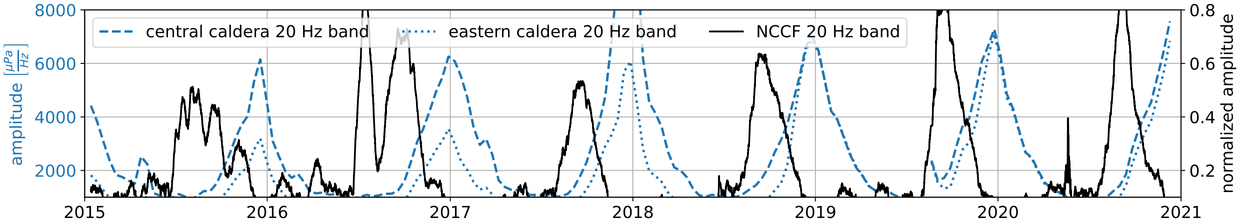

Figure 3.11: Timeline of fin whale vocalizations visible in the acoustic data and the 20 Hz feature visible in the long-term NCCF. There is a notable lag between energy in the NCCF and energy in the ambient sound that the NCCF is computed from. The 20 Hz energy in the NCCF is likely due to a distant fin whale chorus with directionality pointed toward Alaska, while the 20 Hz energy in the ambient sound is likely from local fin whale vocalizations.

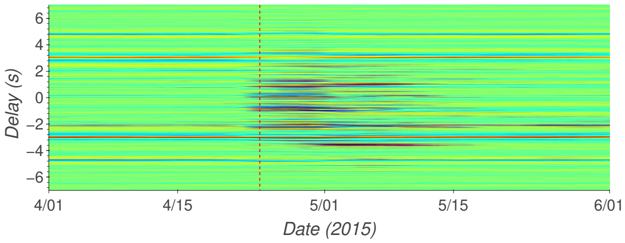

Figure 3.12: NCCF stack during Axial Seamount eruption in April 2015. Dashed line indicates the beginning of the eruption. Effects in the NCCF before dashed line are due to average time window.

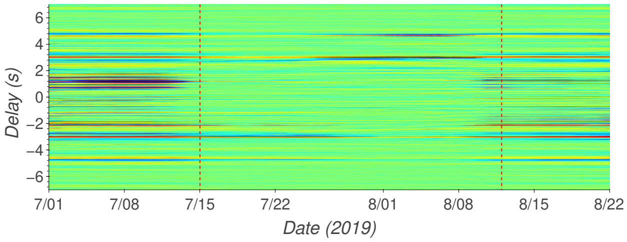

Figure 3.13: NCCF stack during the seismic reflection experiment during July and August 2019. Dashed lines indicate the beginning and end of the experiment. Effects in the NCCF before or after the dashed line are due to the average time window.

Air-gun experiment In July and August of 2019, there was a seismic reflection survey that happened directly over the *Central Caldera* and *Eastern Caldera* hydrophones[¶]. Figure 3.13 shows the NCCF during this experiment. The noise in the NCCF decreases significantly during the air gun experiment. The actual incoherent noise levels in the ocean that are contributing to the noise levels in the NCCF are not expected to change during the duration of the air-gun experiment. The change in noise levels measured by the NCCF are due to the normalization that occurs in the frequency whitening step during pre-processing. The amplitude of the dA peak decreases during the course of the air gun experiment because the coherent sources that contribute to the dA peak are distant source and are being drowned out by the local air gun sound sources. Different TDGF peaks fluctuate in amplitude over the course of the experiment. This is likely due to the changing location of the research vessel as it surveys the ocean floor. In future work this data of opportunity could be used to experimentally explore the effect of local surface sound sorces on multi-path arrivals.

Sporadic 7 Hz aberration Another common aberration in the long-term NCCF stack is present sporadically throughout the 6 years of data, but is more present in 2015 and 2016. Occurrences of this aberration are annotated as *Aberration* in Fig. 3.8(a) This feature is also centered around the dA peak and varies in relative amplitude and delay time length. The 1-hour average, long-term NCCF stack reveals that the NCCF aberration turns on and off with an approximate period of 7 hours (Fig. 3.14(a)). The FFT of the one hour NCCF stack (Fig. 3.14(b)) reveals that the frequency content of this aberration has a peak around 7 Hz and tapers off above around 20 Hz. Figure 3.14(c) shows the spectrogram of the acoustic data from *Eastern Caldera* during this aberration. The 7 Hz sporadic aberrations are centered around the *dA* peak. This corresponds to a directionality of the sound sources causing these phenomena to be in the endfire axis that is pointed towards Alaska (see Fig. 3.2). The cause of this aberration in the NCCF stack is still unknown. Some possible explanations include distant acoustic surveying experiments, other unknown anthropogenic contributions, or seismic activity.

[¶] Cruise DOI: 10.7284/908292

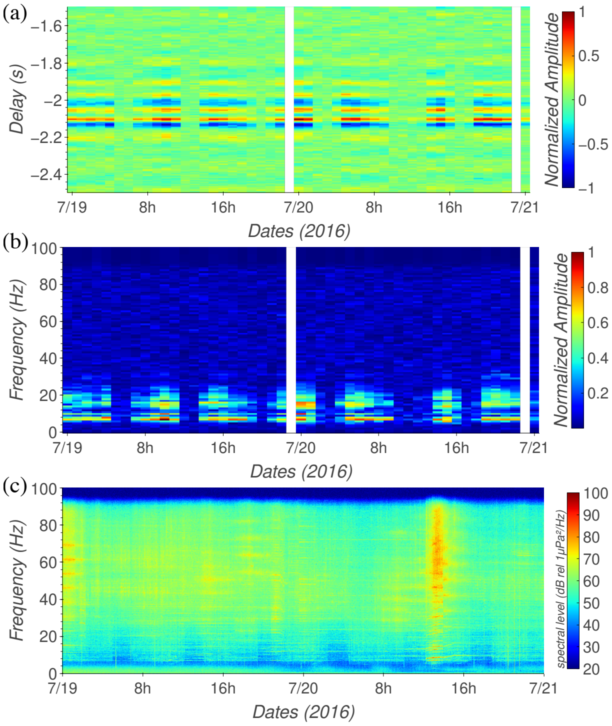

Figure 3.14: (a) 1-hour average NCCF during occurrences of 7 Hz NCCF aberration. Data is from July 19-21 2016. (b) Magnitude of the FFT of the NCCF window shown in a. (c) Spectrogram of hydrophone data from the *Eastern Caldera* hydrophone during the 7 Hz aberration.

3.5 Conclusion

In conclusion, noise interferometry was successfully used to estimate arrival times between two bottom-mounted hydrophones in the OOI Cabled Array separated by 3.2 km at an ocean depth of 1500 m. With an averaging time of 100 hours or larger, direct, surface, and surface bottom reflected acoustic propagation paths are distinguishable throughout the six years of data. Further investigation shows that the direct path peak SNR fluctuates seasonally due to distant fin whale vocalizations. The single surface reflection propagation paths display a small seasonal variation. For *dA*, *s1b0* and *s2b1* peaks, the SNR is stable throughout the six years of data that is analyzed. A long-term noise cross correlation (NCCF) stack was constructed for 6 years of available data to assess the quality of the NCCF. Effects on the NCCF stack were observed from the Axial seamount volcano, a local seismic reflection survey, and seasonal fin whale vocalizations. A fin whale chorus is shown to be detectable with the NCCF that is separate from the local fin whale vocalizations that are present in power spectral time-series of individual hydrophones.

Given the size of the dataset and the quality of multi-path arrivals in the NCCF throughout the six years of data, there are many opportunities for future explorations using this data. Some potential future directions are discussed below.

There is some relevant information contained in the NCCF stack that is unrelated to the TDGF estimate. For some loud features in the ocean, such as the Axial Seamount volcanic eruption, directional information could be inferred from the NCCF stack. The effects of fin whale vocalizations on the NCCF stack could also potentially be developed into new ways to monitor fin whale population and migration. We were able to measure energy from the fin whale chorus that was not clearly visible in individual spectrograms of raw data. Similarly, while there is still no clear explanation for the 7 Hz sporadic aberration described in section 3.3, it is interesting that this coherent sound source is able to be clearly detected even though it is not as clearly visible in the PSD of either hydrophone. In future developments, these features of the NCCF could be leverage to learn information about the ocean.

The results in this chapter lay the necessary ground work for developing long-term ocean monitoring techniques using multi-path arrivals estimated with ambient noise interferometry. Since multi-path arrivals traverse the entire water column, they can be used to infer information about the entire water column. This is an advantage over direct path propagation which can only characterize ocean properties along the eigenray connecting the two nodes. Demonstrating the ability to reliably distinguish the TDGF with hydrophones in an ocean observatory with bottom-mounted hydrophones in the deep ocean also points towards to possibility of scaling up these techniques for global ocean monitoring. According to [93, p. 197], the root-mean-squared-error of an arrival time estimate is a function of the SNR. In future works, models can potentially be developed to invert arrival time estimates to estimate oceanographic variables such as water column sound speed. The analysis presented in this chapter can be used to assess the error bounds of these model predictions.

The seismic reflection survey conducted in 2019 directly over the two hydrophones provides a unique opportunity for further investigation into the technique of noise interferometry. Several chapters have developed simulation techniques to analytically observe the effects of different sound distributions [70, 134, 120]. Since the airgun is an impulsive sound source, this data of opportunity could lead to experimental evidence on how local sound sources contribute to the multi-path arrivals. This is explored in chapter 4.

The quality of the long-term NCCF stack and the reliability of distinguishing multi-path arrivals throughout the six years of data shows promise for future developments in ocean monitoring applications, and is a promising direction of future investigations.

Chapter 4

EXPLORING SURFACE SOURCE CONTRIBUTIONS TO OCEAN AMBIENT NOISE INTERFEROMETRY WITH AIRGUN SHOTS

Abstract

A seismic reflection survey conducted directly over two bottom-mounted hydrophones in the north-east Pacific ocean is used to explore how surface source locations effect ambient noise interferometry for the two hydrophones. The airgun shots are used as an approximation of an impulsive sound source at a discrete location, which allows us to investigate spatial contributions to the cross-correlation between the two hydrophones. Simulated and experimental results are presented. The contributions to the cross-correlations are explained by different reflections off of the surface or bottom of the ocean, and a discussion about what can and cannot be inferred about the emergence to the Green's function is presented. [*]

4.1 Introduction

The goal of ambient noise interferometry is to use ambient sound to infer information about acoustic propagation without any prior knowledge of the ambient sound statistics or sound source distribution. It has been shown in free space that for an isotropic sound source distribution that is uncorrelated in space and time, the derivative of the correlation between two sensors will be the time domain Green's function between the two sensors [117, 164, 137]. Unfortunately, sound sources in the ocean are neither isotropically distributed or uncorrelated in space and time. Knowing how individual sound source locations contribute to the correlation between two sensors is important for understanding how the convergence to the time domain green's function will be effected for arbitrary sound source distributions

---

[*] An earlier version of this work has been published and is available as:
Ragland, J., and Abadi, S. (2022). "Exploring surface source contributions to ocean ambient noise interferometry with airgun shots," The Journal of the Acoustical Society of America, 152, 3069–3077. doi:10.1121/10.0015231

or propagating environments. In this work, a seismic reflection survey that was conducted directly over two bottom-mounted hydrophones in the north-east Pacific ocean will be utilized to experimentally characterize the spatial source contributions to the correlation between the sensors.

For a homogeneous medium with attenuation and an isotropic noise source distribution, the Green's function can be recovered from the cross-correlation between two sensors [117]. This work was then expanded to the case of an oceanic wave guide [120]. Specifically, it was shown that for a Pekeris oceanic waveguide and a surface distribution of noise sources, the cross-correlation function between two sensors converges to an amplitude shaded estimate of the Green's function. Sources located along acoustic ray paths that connect the two sensors contribute to the empirical Green's function estimate and therefore constructively add together when cross-correlations are averaged together [46].

Ambient noise interferometry in the ocean has been experimentally demonstrated for a variety of propagating environments and sound sources, and has been successfully used for passive acoustic tomography. In [116], the frequency band dominated by shipping noise was used to measure the empirical Green's function. In [40], the frequency band dominated by croaker fish vocalizations is utilized for ambient noise interferometry, and empirical Green's functions matched simulated results well. In [10], a tropical storm is utilized for ambient noise interferometry. [46] use vertical line arrays in the north Pacific to estimate the empirical Green's function and are able to successful infer information about the sound speed structure. Utilizing data collected off of the coast of Florida, emperical Green's functions were successfully recovered and were used for inferring modal dispersion, flow velocity estimation, estimating bottom properties, and time reversal [49, 12, 13, 44, 142, 177]. Utilizing deep sound propagating channels and ice breaking events, the temperature of the deep ocean has also been measured using ambient noise interferometry [173, 172, 38]. Dispersion curves for the first three modes have been passively measured for a highly dynamic, shallow ocean, using a horizontal line array off the coast of New-Jersey [143, 141]. Ambient noise interferometry has also been demonstrated for bottom-mounted hydrophones in the deep ocean with strong contributions from multi-path arrivals [110].

The effects of anistropic noise source distributions have been explored by several works. [46] demonstrates that if the noise source distribution varies gradually in space, travel times can be accurately estimated using ambient noise interferometry. [162] derive a correction factor for estimated arrival times given a directionality of ambient sound. [14] uses the ambient noise model proposed by [27, 28] to study the model's effects on the vertical and horizontal wave coherence between two sensors. This model consists of a uniform distribution of sound sources at the surface of the ocean with no bottom. [158] expand this work to additionally include a non-isotropic horizontal distribution of noise sources. [158] find that, given a non-isotropic distribution of noise sources, horizontal coherence between two sensors still contains information about the Green's function between the two sensors, but that the derivative in time of the coherence does not explicitly equal the Green's function between the two sensors. [159] investigates the effects of anisotropic noise on how wave coherence constructively and destructively interferes. Specifically, [159] show that even for heavily directional ambient sound, only sound that travels through both sensors contributes significant energy to the coherence between the two sensors.

Recently, numerical methods have been used to explore the effects of complex refracting environments on ambient noise interferometry [134, 135]. A method is developed to numerically simulate the cross-correlation between two sensors, given a distribution of sound sources [134]. They discover that there are sound speed profiles and hydrophone geometries that do not result in the convergence of the cross-correlation to the emperical Green's function, given a uniform surface distribution of sound sources. This is because, for certain propagation environments and hydrophone geometries, acoustic ray paths that connect both hydrophones do not intersect with the surface. [135] develop a metric called the sensitivity kernel that evaluates how a source located at a specific point in space effects the cross-correlation at specific delay times.

In this chapter, a seismic reflection survey will be used to experimentally characterize the spatial contribution of sound sources on the cross-correlation function. Two hydrophones that are part of the Ocean Observatories Initiative (OOI), separated by 3.19 km, and are bottom mounted at a depth of 1500 m will be used. The sensitivity kernel described by [135] will be experimentally measured and compared to simulated results. The patterns that are observed in the experimental and simulated results are then explained and related to different reflections off of the surface or bottom of the ocean using the method of images. Lastly, what can and can not be learned from the sensitivity kernel will be discussed.

In section 4.2, information about the experiment and details about the data processing are presented. In section 4.3.1, a review of the sensitivity kernel is presented. Section 4.3.2 presents the simulated results and section 4.3.3 presents the experimentally measured sensitivity kernel using the airgun. An explanation for these results is presented in section 4.4.1 and 4.4.2. Lastly, a discussion and conclusion of the findings are presented in section 4.5.

4.2 Experimental Setup

In the following section the hydrophone and airgun experiment geometries will be described as well as the data processing that was completed for the subsequent analysis.

We are using two hydrophones that are 270 km off of the Oregon coast and are part of the Ocean Observatories Initiative (OOI) network. Ambient noise interferometry has previously been demonstrated for these two hydrophones [110]. The two hydrophones that are used are the *Central Caldera*[†] and *Eastern Caldera*[‡] hydrophones, which are separated by 3.186 km, are bottom mounted at depths of 1527 m and 1518 m respectively, and both have a sampling

---

[†] NFS Ocean Observatories Initiative Data Portal, https://ooinet.oceanobservatories.org Low-Frequency Acoustic Receiver(network:OO, station:AXCC1) Downloaded on March 1, 2022

[‡] NFS Ocean Observatories Initiative Data Portal, https://ooinet.oceanobservatories.org Low-Frequency Acoustic Receiver(network:OO, station:AXEC2) Downloaded on March 1, 2022

rate of 200 Hz. Acoustic data is downloaded using the python package OOIPy [127]. The seismic reflection survey that is are utilized is the MGL1905 cruise[§]. The location of the vessel and experiment logs are publicly available. This seismic reflection survey included 36 airguns that are towed behind the research vessel at a depth of 12 m and 230 m behind the research vessel. For this analysis the assumption is made that the airgun array is a point source. Spectrograms of airgun shots recorded by OOI hydrophones are reported in [107].

For the subsequent analysis in section 4.3, a single noise cross-correlation function (NCCF) needs to be associated with a point in space where the airgun was fired. In this chapter, the term NCCF will be used to describe the physically processed data that includes a finite averaging time and any other data processing. The term cross-correlation will refer to the expectation of the correlation between two sensors.

During a line of the experiment, the time between airgun shots is approximately 18 s, and the average speed of the vessel is approximately 4.2 knots The location of the vessel and the NCCFs are averaged to the same time grid with an averaging time of 2 min. This means that each calculated NCCF contains approximately 6 airgun shots, and the distance covered by the research vessel is approximately 270 m. For the sake of this analysis, the distance traveled by the research vessel during the 2 min averaging time and the length of the airgun lines behind the research vessel are considered to be negligible. Data is only kept during lines of the airgun experiment and when acoustic data from both hydrophones exist. Additionally, data from the last 4 lines of the experiment are discarded because of the non-symmetric path of the ship and higher source levels of the airgun. This resulted in 304 h of acoustic data. Figure 4.1 shows a map of the 2 min average airgun locations that have associated NCCFs. The two hydrophones are labeled (*Eastern Caldera* and *Central Caldera*) as well as the location of the CTD cast used for analysis (*Axial Base*).

To calculate the NCCFs, acoustic data is downloaded from OOI using the python package OOIPy [127], separated into 30 s segments and filtered between 1 and 90 Hz using a 4th order, zero-phase, Butterworth filter. The 30 s data segments from each hydrophone are then cross-correlated and averaged together for 2 minutes.

The latitude and longitude coordinates of the research vessel are transformed into a Cartesian coordinate system in km, where the origin is the midpoint between each hydrophone and the x axis is the axis connecting the hydrophones. Therefore, the coordinate of the *Central Caldera* hydrophone is (-1.59, 0) km and the coordinate of the *Eastern Caldera* hydrophone is (1.59, 0) km. The latitude and longitude coordinates are transformed by calculating the range from the hydrophone midpoint and the bearing from the hydrophone midpoint assuming a spherical and transforming these polar coordinates to Cartesian coordinates.

[§] Cruise MGL1905 on research vessel Marcus G. Langseth DOI: 10.7284/908292
https://www.rvdata.us/search/cruise/MGL1905, accessed on March 1, 2022

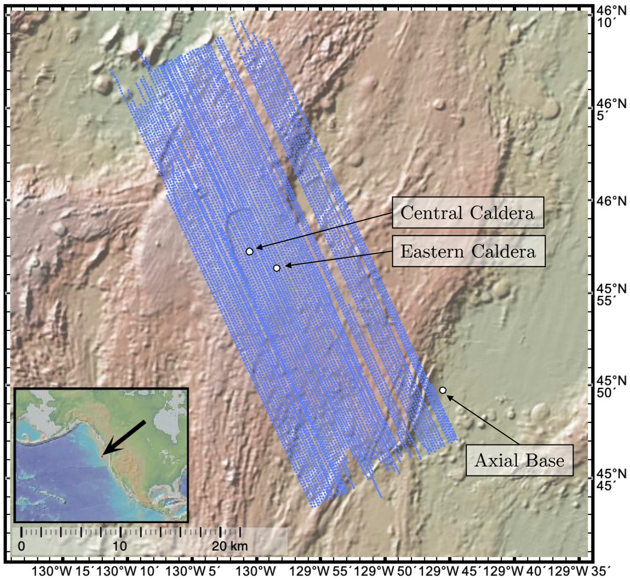

Figure 4.1: Map of the 2 min average airgun locations that have associated NCCFs and the locations of the two hydrophones that are used to calculate the NCCFs. The hydrophone on the left is the *Central Caldera* hydrophone and the hydrophone on the right is the *Eastern Caldera* hydrophone.

4.3 Results

In the following section, the theoretical formulations of the sensitivity kernel and how it relates to airgun measurements is reviewed. The sensitivity kernel is simulated for the given hydrophone geometry and presented. Lastly, the measured results that utilize the airgun shots are presented.

4.3.1 Theoretical background

The sensitivity kernel [135] for ambient noise interferometry is defined in equations 4.1 and 4.2, where $K(\mathbf{x}, \tau; \mathbf{x_1}, \mathbf{x_2})$ is the cross-correlation sensitivity kernel, $S(\mathbf{x})$ is the source distribution density, $H(\omega)$ is the receiver response, $\mathbf{x_1}$ and $\mathbf{x_2}$ are the location of the two sensors, and $G(\omega; \mathbf{x_1}|\mathbf{x})$ is the Green's function at location $\mathbf{x_1}$ due to a source located at $\mathbf{x}$.

$$C_{1,2}(\tau) = \iiint_V K(\mathbf{x}, \tau; \mathbf{x_1}, \mathbf{x_2}) \cdot S(\mathbf{x}) dV(\mathbf{x}) \tag{4.1}$$

$$
\begin{gathered}
K(\mathbf{x},\tau;\mathbf{x_1},\mathbf{x_2}) = \\
\frac{1}{2\pi}\int_{-\infty}^{\infty} \left|H(\omega)\right|^2 G(\omega;\mathbf{x_1}|\mathbf{x})G^*(\omega;\mathbf{x_2}|\mathbf{x})e^{j\omega\tau}d\omega
\end{gathered}
\tag{4.2}
$$

From inspection, the Fourier transform of the sensitivity kernel can be written as Eq. 4.3

$$
\begin{gathered}
K(\mathbf{x},\omega;\mathbf{x_1},\mathbf{x_2}) = \\
\left|H(\omega)\right|^2 G(\omega;\mathbf{x_1}|\mathbf{x})G^*(\omega;\mathbf{x_2}|\mathbf{x})
\end{gathered}
\tag{4.3}
$$

The sensitivity kernel is a function of both space and time and is a metric that evaluates what locations contribute to a cross-correlation between the two sensors for different delay times.

Looking at Eq. 4.3, one can see that the sensitivity kernel is composed of the frequency response of the sensors and the cross-correlation in time of the green's functions between $\mathbf{x_1}$ and $\mathbf{x}$, and the green's function between $\mathbf{x_2}$ and $\mathbf{x}$. Therefore, given a uniform sensor response, the sensitivity kernel is the cross-correlation between two sensors with a single, impulsive point source located at $\mathbf{x}$. For the frequency band investigated in this chapter, an airgun shot is a good approximation of an impulse function. This allows us to experimentally measure the sensitivity kernel. For this analysis, I assume that the airgun shot is an isotropic point source and I also ignore airgun shot variations.

4.3.2 Numerical Results

The sensitivity kernel in Eq. 4.2 can be numerically simulated using any wave-theoretic method to solve for the two Green's functions. For this analysis, the Green's functions are calculated using normal mode propagation and are solved using KRAKEN [104]. The oceanic wave-guide is assumed to be range independent with a depth of 1523 m. The two hydrophones are placed at a depth of 1522 m. The sound speed profile used for simulation is measured by the *Axial Base* ocean profiler from OOI, located approximately 20 km from the two hydrophones (see Fig. 4.1). A single, average sound speed profile that was measured between July 15, 2019, and August 15, 2019 will be used for all analysis. Figure 4.2(a) shows the sound speed profile used for simulation and 4.2(b) shows the simulated time domain Green's function between the two hydrophones using normal mode propagation. The Green's function is simulated in the frequency band 0 to 100 Hz for 0 to 30 s with a sampling rate of 200 Hz. The Green's function is then multiplied in the frequency domain by the response of the digital filter described in section 4.2. All subsequent Green's functions that are simulated in the following analysis are calculated using this same method. Figure 4.2(c) shows the first 4 eigen rays at a frequency of 50 Hz (simulated with BELLHOP[130]). At this frequency, ray-theoretic methods are not an accurate solution to the wave equation, but they do provide intuition into how the waves are propagating and will provide helpful context for further discussions. The peak in Fig. 4.2(b) at 2.9 s is due to the ray path that bounces off of the surface once and the peak at 4.6 s is due to the ray path that bounces off of the surface twice and the bottom once.

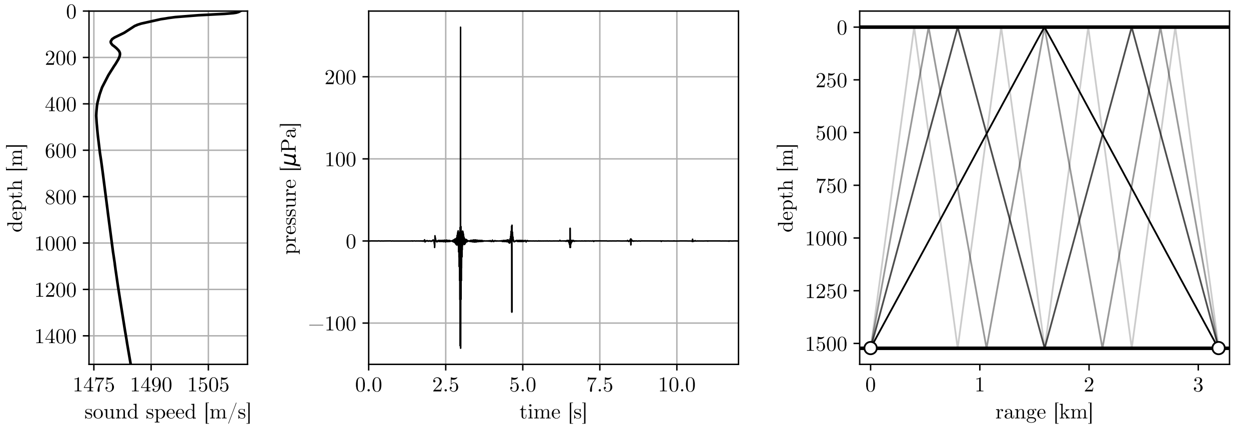

(a) (b) (c)

Figure 4.2: (a) average sound speed profile measured by the *Axial Base* ocean profiler from OOI during the airgun experiment. (b) The simulated, band-limited, time domain green's function between the two hydrophones. This was simulated with normal modes and using the Kraken code to solve for the modes [104] (c) The first 4 eigen-rays between the two hydrophones solved with BELLHOP [130] for f = 50 Hz.

Figure 4.3 shows the horizontal slice at a depth of 12 m of the simulated sensitivity kernel as defined in equation 4.2 for several delay times (plotted in blue). The slice is simulated at a depth of 12 m because this is the depth of the airguns. The amplitudes are plotted in dB relative to the maximum value at $\tau = 0$ s. The lines plotted in red are described in detail in section 4.4.1. In this analysis, the positive delay times which characterizes acoustic propagation from *Eastern Caldera* to *Central Caldera* are presented. If the flow velocity of the water is assumed to be negligible, then the sensitivity kernel will be symmetric along the y-axis for negative delay times.

In Fig.4.3(a) the sensitivity kernel is shown for the delay time of $\tau = 0.1$ s. The vertical line at $x = 0$ km represents sources that are equidistant from each hydrophone and therefore contribute to the cross-correlation at a delay time of $\tau = 0$. The other vertical lines are caused by reflections off of the bottom or surface of the ocean. In Fig.4.3(b), the sensitivity kernel is shown for delay time $\tau = 1.8$ s. In Fig.4.3(c), the sensitivity kernel is shown for delay time $\tau = 2.6$ s. For both $\tau = 1.8$ s and $\tau = 2.6$ s there are no arrivals in the TDGF between the two hydrophones. This means that sources that contribute to this delay time will average out of the cross-correlation, given an isotropic noise source distribution. Figure

4.3(d) shows the sensitivity kernel for delay time $\tau = 2.96$ s. This is the arrival time of the surface reflection peak as seen in Fig.4.2(b). In the frequency band where ray-theoretic formulations are valid solutions to the wave equations, sources that contribute to arrival times in the cross-correlation are located along rays that connect the two sensors [45]. The ray path associated with an arrival at $\tau = 2.96$ s is the darkest ray path plotted in Fig. 4.2(c) and reflects off of the surface of the ocean once. Sources along this ray path extension that are located on the surface of the ocean would be expected to be at discrete ranges separated by the distance of the two hydrophones. Figure 4.3(e) shows the sensitivity kernel for delay time $\tau = 4.0$ s. This delay time, similar to the delay times of 1.8 s and 2.6 s does not correspond to an arrival time in the TDGF. Figure 4.3(f) shows the sensitivity kernel for the delay time $\tau = 4.60$, which is the time of the second arrival in the TDGF. This arrival time is associated with the ray path that reflects off of the surface twice and the bottom once. The hot spots visible in Fig.4.3(f) correspond with the intersections of this ray extension with the surface of the ocean. Further investigation into the curves seen in the sensitivity kernel for different delay times will be presented in section 4.4.1.

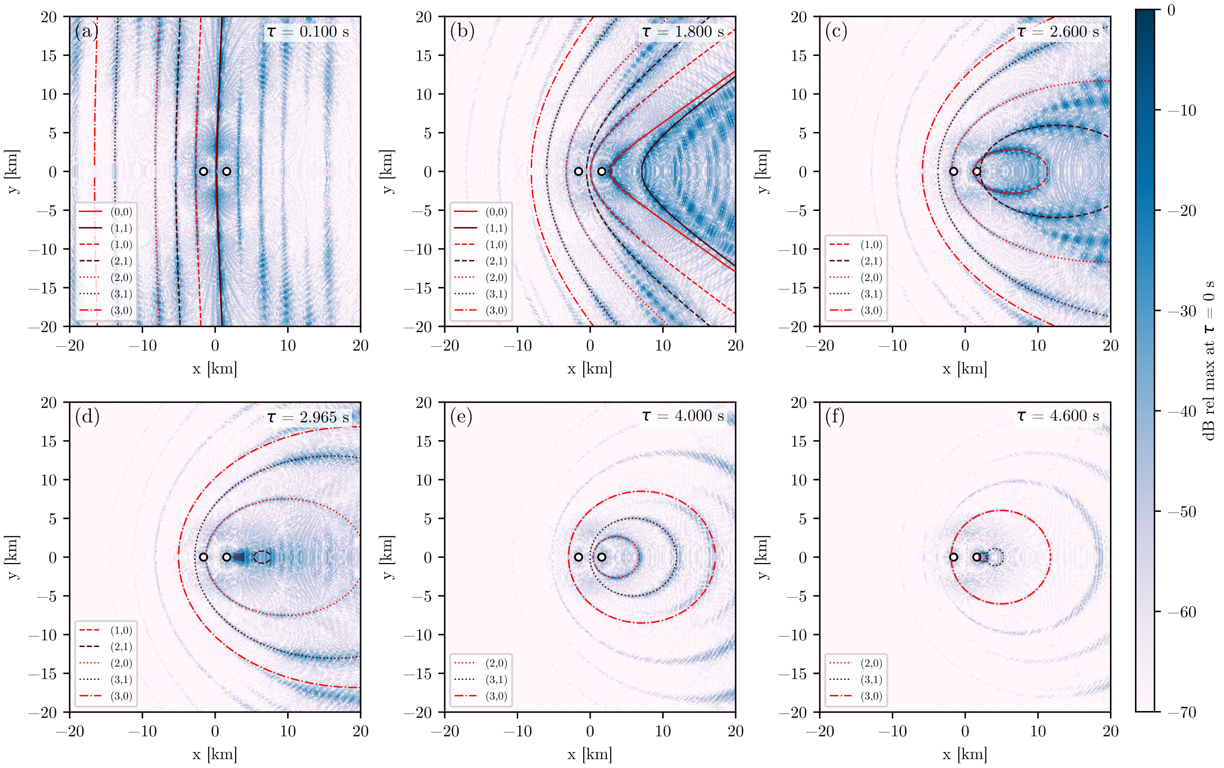

Figure 4.3: (a)-(f) Horizontal slice of the simulated sensitivity kernel at a depth of 12 m for different delay times. The sensitivity kernel is plotted in blue. The red lines are slices of hyperboloids that explain the different patterns as described in section 4.4.1.

4.3.3 Experimental Results

Figure 4.4 shows the experimentally measured sensitivity kernels for different delay times (plotted in blue). To reduce noise, the root mean squared amplitude of the cross-correlation is presented for a window length of 0.02 s centered around the reported delay time. The red lines are described in detail in section 4.4.1. The simulated and measured results are in good agreement. The measured results have more attenuation due to surface or bottom reflections. This discrepancy is likely due to the environmental parameters chosen for the simulated environment not perfectly matching the physical bottom properties of the ocean.

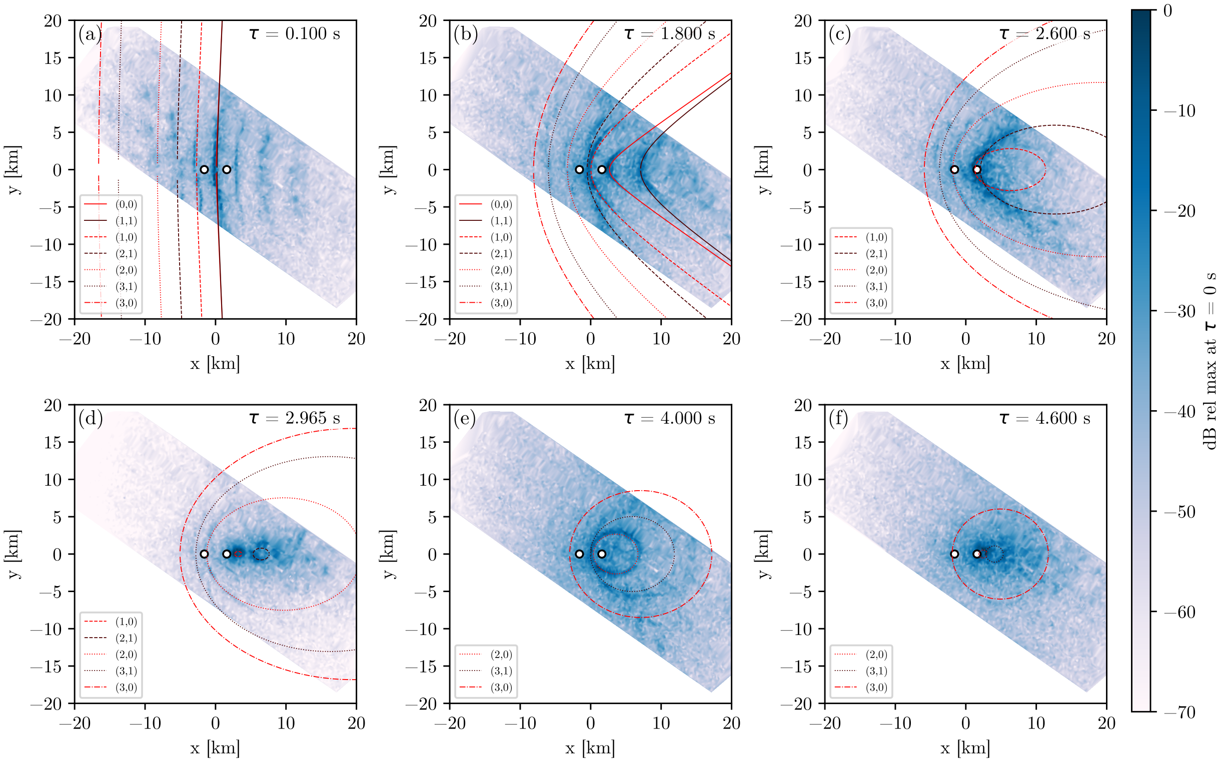

Figure 4.4: (a)-(f) Horizontal slice of the experimentally measured sensitivity kernel using airgun shots. The NCCFs are plotted for different delay times and airgun locations in blue. The red lines are slices of hyperboloids that explain the different patterns as described in section 4.4.1.

4.4 Discussion

In the following sections, an explanation of the patterns that are seen in Figs.4.3 and 4.4 is presented, the reasoning why the sensitivity kernel has non-endfire contributions is discussed.

4.4.1 Explaining patterns in the sensitivity kernel

For the case of free space propagation in a homogeneous medium, different delay times in the cross-correlation are caused by sources located on the surface of a hyperboloid [117]. The hyperboloid is defined by a constant difference in range between the two sensors and a given point in space. For the case of a homogeneous medium, this constant difference in range corresponds to a constant difference in propagation time. The two sensors are located in the foci of the hyperboloid. Different delay times correspond to how 'open' the hyperbola is, where a delay time corresponding to 0 s corresponds to a constant line in the broadside of the two sensors. This represents sources that are equidistant from both sensors. A delay time equal to D/c, where D is the distance between the hydrophones and c is the speed of wave propagation in the medium, corresponds to a line pointing in the end-fire direction of the sensors. This has also previously been utilized in time difference of arrival beam-forming, where an approximation of the bearing of a source is a function of delay time and is also derived by utilizing hyperbolas [18].

As can be seen in Fig. 4.2(c), due to the small separation of the hydrophones, refraction does not effect the ray paths significantly. Therefore, a constant sound speed equal to the average sound speed of the water column can be used to approximate acoustic wave propagation in this environment. The boundary conditions of the oceanic wave-guide can be accounted for by using the method of images. Given these assumptions, equations for hyperboloids that correspond to different pairs of hydrophones or hydrophone images can be derived. The method of images has previously been used to prove that a uniform distribution of surface sources results in the convergence of the cross-correlation to an amplitude shaded Green's function for a Pekeris wave-guide [120].

The source locations that contribute to the cross-correlation for our (simplified) environment, therefore lie on the surfaces of hyperboloids formed by different image orders of sensor 1 and sensor 2. The sources that contribute to the cross-correlation along the plane defined by a constant depth of 12 m can therefore be explained by a horizontal slice of these hyperboloids at a depth of 12 m.

Figure 4.5 gives a schematic of this problem formulation. Different image orders are referenced numerically where 0 indicates the physical hydrophones and 1 would indicate the first image. A specific hyperboloid is referenced using the image index of each sensor that is used to define the foci of a hyperboloid. For instance, the light red (dashed line) hyperbola shown in Fig. 4.5 is referenced by the index pair (0,0). This means that the foci of the hyperboloid are located at the physical location of sensor 1 and the physical location of sensor 2. The dark red (solid line) hyperbola shown in Fig. 4.5 is referenced by the index pair (2,1). This means that the foci of the hyperboloid are located at the second image order location for sensor 1 and the first image order location for sensor 2.

The plotted lines in Figs. 4.3 and 4.4 are these hyperboloid slices for some of the relevant hydrophone image pairs. Hyperboloid slices with the same dash pattern correspond to hydrophone image pairs that have parallel axes. For instance, the solid lines correspond to (0,0) and (1,1). The color of the lines corresponds to the image pair of the sensor on the

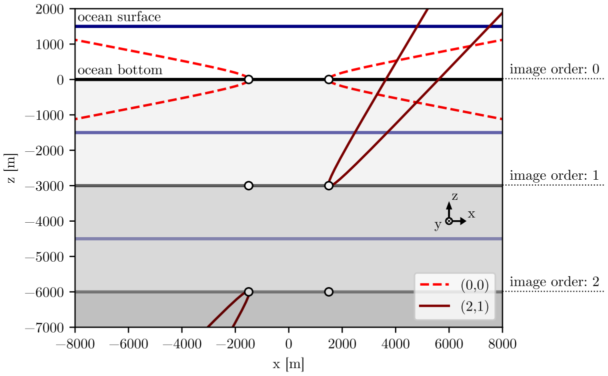

Figure 4.5: Schematic of the hyperboloids that are formed using the method of images. Each hyperboloid is indexed by the image order of the two hydrophones that are used to define the hyperboloid. The hydrophones are located in the foci of the hyperbola, but appear to be located on the hyperbola due to the scale.

right. For instance the light red lines correspond to hyperboloid slices that correspond to the physical sensor on the right, while the brown lines correspond to hyperboloid slices that correspond to the first image of the hydrophone on the right. Not every hyperboloid slice that shows up in the sensitivity kernel is plotted. For instance, in Fig. 4.3(b), the curves in the sensitivity kernel that are to the right of the two solid lines correspond to image pairs of (2,2) and (3,3). In Figs 4.3 and 4.4 it can clearly be seen that the patterns seen in the sensitivity kernel have good agreement with the geometrically derived hyperboloid slices. The concentric circle patterns (most clearly seen for delay times greater that $\tau = 2.6$ s) are explained by hyperboloid slices formed by hydrophone image pairs that have parallel axes. The circles get smaller for greater delay times because of the hyperboloids closing. The analytical expressions for all plotted hydrophones are provided in appendix A.

4.4.2 Sensitivity kernel and Green's function emergence

In Figs 4.3 and 4.4, energy that is not in the end-fire direction and more specifically, not along ray path extensions that connect the two hydrophones is clearly present. Off end-fire energy is even present during delay times that correspond to arrival times in the time domain Green's function between the two sensors (see Figs. 4.4(d) or 4.4(f)). As explained in section 4.4.1, patterns in the sensitivity kernel are caused by hyperboloid slices created by different surface or bottom reflections, but why do we see energy in the sensitivity kernel that doesn't contribute to the TDGF?

The sensitivity kernel represents the locations in space that contribute energy to different delay times between two sensors. As mentioned in section 4.3.1, the sensitivity kernel can be interpreted as the cross-correlation between two sensors located at $\mathbf{x_1}$ and $\mathbf{x_2}$ for a single, impulsive sound source located at $\mathbf{x}$. Since the sensitivity kernel considers a single point in space, the amplitude of the sensitivity kernel does not include information about how sources will constructively or destructively interfere when integrated over a given source distribution. This means that the amplitude of the sensitivity kernel will not be larger along ray path extensions, or in the end-fire direction at arrival times. This explains why energy is seen in the sensitivity kernel for all delay times, and why at arrival times, the sensitivity kernel contains energy from other hydrophone image pairs. The sensitivity kernel, therefore, does not characterize which sources contribute to or degrade in the emergence of the time domain Green's function between the two hydrophones. The effects of a single impulsive source and a distribution of sound sources on the amplitude of the cross-correlation is demonstrated well in Figs. 4 and 5 in [134].

The sensitivity kernel is a useful tool for providing intuition about how a specific source location will affect the cross-correlation between the two sensors. However, the amplitude of the sensitivity kernel should not be confused as containing information about how a cross-correlation will converge to the empirical Green's function for an arbitrary source distribution. The constructive and destructive interference is determined by the volume integral in equation 4.1.

4.5 Conclusion

In conclusion, the sensitivity kernel for two bottom mounted hydrophones is simulated and experimentally measured using a seismic reflection survey as data of opportunity. Given the geometry and propagating environment of the two hydrophones, strong multi-path arrivals are present in the Green's function between the two hydrophones. This significantly effects the patterns that are seen in the horizontal slices of the sensitivity kernel. Using a model of a constant sound speed throughout the water column, the shapes in the sensitivity kernel can be geometrically explained by using the method of images and taking horizontal slices of the hyperboloids that are formed by different hydrophone image combinations for a specific delay time. Lastly, this specific hydrophone geometry and propagating environment illuminates how the sensitivity kernel does not exclusively contain information about how a specific source location will contribute to the empirical Green's function between the two hydrophones.

Chapter 5

ESTIMATING DEEP WATER COLUMN TEMPERATURE WITH OCEAN AMBIENT NOISE INTERFEROMETRY

Abstract

Measuring the temperature changes of the deep ocean will be critical to understanding how the system will respond to climate change. In this work, we present a method for measuring the depth-averaged, deep ocean temperature at local ($\sim 3\,\text{km}$) spatial scales using passive estimates of acoustic propagation. These passive acoustic estimates of deep ocean temperature can be used with existing and future passive acoustic monitoring infrastructure to provide complimentary observations of the ocean to in situ measurements, and could be particularly useful in areas of poor ocean observation coverage. Using eight years of ambient sound data, we demonstrate that the passive estimates agree with global ocean models and measurements by Argo floats. The rms difference between the HYCOM ocean model is shown to be 0.13 °C, and the root-mean-squared difference between ARGO measurements is shown to be 0.086 °C.*

5.1 Introduction

Increased concentrations of anthropogenic greenhouse gases result in an Earth energy imbalance, where more heat is being trapped in the system than being radiated into space. Most of this excess heat (89 %), is being stored in the ocean, with 46 % being stored in the upper 700 m and 25 % being stored from 700 - 2000 m [155]. How and where this additional heat is stored will affect a new climate equilibrium, and observing the deep ocean will play a critical role in a well managed future. The deep ocean is one of the least understood and observed regions of the ocean, and the increased ability to reliably observe the deep ocean will play a critical role in monitoring and understanding changes to the system due to anthropogenic forcing [72]. In this work, we demonstrate the feasibility of using cabled, bottom mounted hydrophones deployed for passive acoustic monitoring (PAM), to observe

---

*A version of this chapter is under review for publication in Geophysical Research Letters.

local, depth-averaged, deep ocean temperatures. We utilize the diffuse sound field and the technique of ambient noise interferometry to estimate the acoustic Green's function with a high enough accuracy to see sub-seasonal changes in the integrated deep ocean temperature, at a local ($\sim 3\,\text{km}$) spatial scale.

Ambient noise interferometry is a technique that utilizes diffuse ambient sound to passively illuminate acoustic propagation between sensors [114, 163, 116, 137, 160, 164]. This estimate of acoustic propagation can be used alongside acoustic tomographic methods to estimate environmental parameters. This technique has been used extensively in the seismic community for understanding and imaging the Earth's crust [119, 129, 7, 31], and shows promise for being used to make observations of the interior of the ocean.

For perfectly diffuse, stochastic ambient sound, the expectation of the time derivative of coherence between two sensors is the two directional, band-limited Green's function [177, 137, 120]. In ocean environments, sound sources are often distributed on the surface, which means that the ambient sound field is not perfectly diffuse. In this case, the time derivative of the coherence converges to an approximation of the Green's function, referred to as the empirical Green's function (EGF). The EGF may have different amplitudes than the actual Green's function but, if the diffuse sound sources adequately illuminate the acoustic propagation, the phase information will be preserved [43, 120, 158, 134]. Since mode phases or arrival times are often the acoustic features used in acoustic tomography, it is still possible to estimate environmental parameters from the EGF. Equation 5.1 expresses the relationship between wave coherence and the two EGFs. $\langle C_{12}(\tau)\rangle$ is the expectation of the cross-correlation between sensors 1 and 2. $\hat{G}_{12}(\tau)$ is the EGF characterizing acoustic propagation from location 1 to 2. $D(\tau)$ is a band-limited impulse function that represents sound source illumination. $D(\tau)$ is a function of sound source statistics and if the sound sources are delta correlated in time and space, then $D(\tau)$ is the auto-correlation of the sound source random process.

$$\left\langle \frac{dC_{12}(\tau)}{d\tau} \right\rangle = D(\tau) * \left[\hat{G}_{12}(\tau) - \hat{G}_{21}(-\tau)\right] \tag{5.1}$$

In the ocean, ambient noise interferometry has been experimentally demonstrated to estimate the Green's function for a diverse set of environments and illuminating sound sources [116, 10, 40, 12, 173, 73, 110]. Estimating oceanographic variables with ambient noise interferometry requires the accurate estimation of the Green's function between the sensors and also solving the inverse estimation problem that can estimate environmental parameters from acoustic features. Ambient noise interferometry has been used for several applications in acoustic oceanography. In shallow water environments, acoustic mode shapes [177, 13], bottom properties [145, 142, 143], sound speed [73], and flow velocity [49] have been estimated. In the deep ocean, long-range acoustic propagation in the sound channel has been used to estimated changes in water temperature along the sound channel [172].

In this work, we use the cross-correlations of eight years of ambient sound data, recorded by the Ocean Observatories Initiative (OOI) [100, 101], to reliably observe sub-seasonal fluctuations in acoustic arrival times of the surface reflected path at a spatial scale of $\sim$

3 km. These arrival time fluctuations can then be used to estimate depth-averaged water temperature. The passive acoustic estimates of depth-averaged water temperature are shown to be consistent with ocean model outputs and ARGO float data.

5.2 Estimating Empirical Green's function from ambient noise

This chapter utilizes the Central and Eastern Caldera hydrophones that are part of the OOI cabled array. The two hydrophones are bottom mounted at depths of 1519 m and 1511 m, are separated by 3.186 km, and have a sampling rate of 200 Hz. Information about the sensor responses can be found on the IRIS website[100, 101]. For this chaper, we consider the ambient sound data recorded from 2015 through 2022. Figure 5.1(a) shows a map of the hydrophones, located in the caldera of the Axial Seamount volcano, which is approximately 270 km off the west coast of Oregon.

It has previously been shown that, due to the small sensor separation relative to the depth of the water column, ray-based methods provide relevant context to acoustic propagation for this environment [110, 108]. The first three acoustic rays are shown in figure 5.1(b), which are simulated with Bellhop [105] using a sound-speed profile computed from HYCOM. Figure 5.1(c) shows a single complex envelope of a, 601 h cross-correlation calculated from ambient sound and the simulated time-domain Green's function using a HYCOM sound speed profile. The time-domain Greene's function is simulated with the method of normal modes. For more information about the acoustic simulations used in this work, see section 5.3.1.

The ambient soundscape at these hydrophones is dominated by wind, shipping, and fin-whale vocalizations [111]. It has been experimentally demonstrated that the sound sources that contribute to the multi-path empirical Green's function arrivals are local surface sources [107]. Because of this, the dominant illuminating sound source is likely local surface wind noise, which at the spatial scale of the hydrophone array will result in diffuse surface illumination. This means that there should be no arrival time bias between the empirical Green's function and the actual Greene's function [120, 43]. Spectral content of wind generated noise has previously been studied [78]. The cross-correlations of ambient sound for these specific hydrophones have previously been demonstrated to consistently converge to the empirical Green's function between the hydrophones over six years of studied ambient sound [110]. These passive estimates of the Green's function have multiple acoustic arrivals that correspond to multi-path propagation through the water column. Direct path peaks can be seen at ± 2.1 s. There may also be peaks between ± 2.1 s that correspond to acoustic propagation through the seafloor.

For this chapter, we estimate the arrival times of the single surface reflection path using a 601 hour of average ($\sim$ 25 days). These estimated arrival times are accurate enough to sense the small, seasonal fluctuations in the averaged acoustic arrival time. We focus on the arrival time of the single surface reflected acoustic arrival at about 3 s (Fig 5.1(b)). This arrival has the highest SNR and traverses the entire water column. Therefore, the time of this arrival represents an observation of the integrated sound speed along the ray path. Fluctuations in the integrated sound speed are almost completely linearly related to local fluctuations in the depth-averaged water temperature [93, 173].

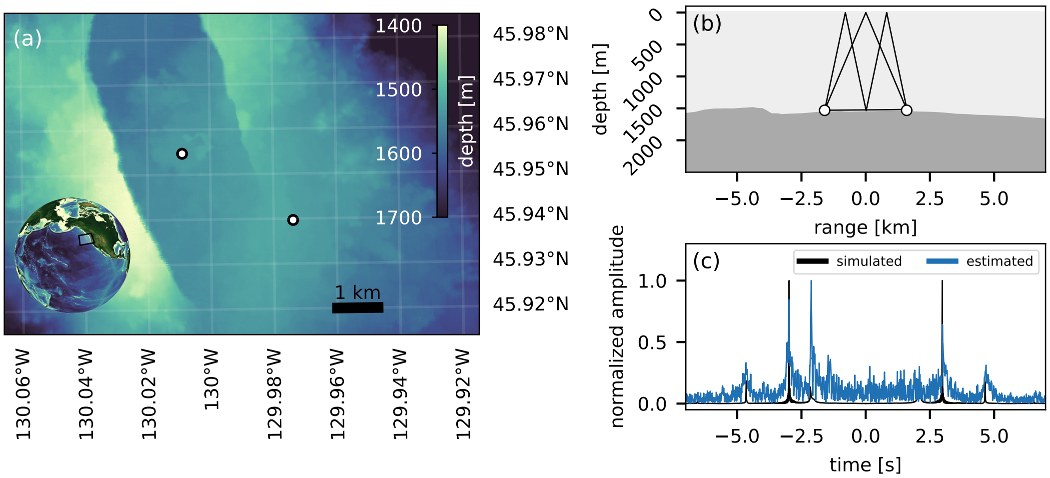

Figure 5.1: (a) Map of axial seamount volcano and hydrophone placement. The hydrophones are separated by 3.186 km, and bottom mounted at depths of 1519 m and 1511 m. Bathymetric data from [19] (b) The first three simulated acoustic eigenrays that connect the two, bottom mounted hydrophones. The dark gray represents the seafloor and the light gray represents the water column. (c) Simulated time-domain Green's function (black) using the sound speed from July 1, 2017 and the EGF (blue), estimated from 601 h of ambient sound cross-correlations from July 1, 2017 to July 25, 2017.

The acoustic data from both hydrophones is pre-processed and the 601-hour average cross-correlation is computed throughout the eight years of data analyzed. For an averaging time of 601 hours, the effects of tides on the arrival times is negligible. The surface reflection arrival time is estimated from both the lag and lead time in the ambient sound cross-correlation, estimating the acoustic propagation in both directions. The peak location is estimated using a window of 1 second around the expected peak arrival time. Given the two independent observations of acoustic arrival time, the maximally likely arrival time is computed, assuming no current.

5.2.1 Signal processing methods

Since the ambient sound field is not perfectly diffuse and spurious loud events, such as single fin whale calls, can corrupt the correlations' emergence to the empirical Green's function, several processing steps are used to improve the convergence to the EGF. The processing steps for estimating the cross-correlation are similar to those used in [110]. A diagram of the signal processing steps used to compute the noise cross-correlation function (NCCF) and estimate acoustic arrival times is shown in figure 5.2.

The uncalibrated ambient sound data from both hydrophones is filtered between 1 - 90 Hz using a fourth order, zero-phase, Butterworth filter. Then the data is clipped to ± 3 standard deviations for a given hour of ambient sound data. The data is then frequency whitened by replacing the magnitude of the signal in the frequency domain with the magnitude response of the same Butterworth filter used previously (retaining only the phase information). These preprocessed signals from each hydrophone are then cross-correlated in the time domain and stacked to a one-hour average noise cross-correlation function (NCCF). To remove high-energy, coherent sound from non-diffuse sound sources, 1 hour NCCFs that have a total signal energy greater than 3.4 standard deviations of the ensemble are removed. The outlier threshold was hand tuned to give the most robust estimate of the arrival time over the 8 years of data analyzed. The one hour NCCFs are then averaged to 601 hours. The time derivative of the NCCF is numerically computed by using numpy gradient [56], which uses the second order accurate central differences to estimate the derivative.

Each NCCF that converges to the EGF has two different peaks corresponding to the surface reflection acoustic path. These two arrival times characterize acoustic propagation in both directions. These arrival times will differ if there is a current along the acoustic path [67]. For the time scales we are considering (601 h), we assume that differential changes in arrival time due to currents will be negligible. The lag and lead, surface-reflection arrival times are estimated by taking a 1-second window around the expected time of the arrival, and using quadratic peak interpolation [136] on the magnitude of the analytical signal. The standard deviation of the lag and lead arrival times is estimated using equation 5.2 [93, p. 197].

$$\sigma_\tau = [(\Delta\omega_{\text{rms}}) \times \text{SNR}]^{-1} \tag{5.2}$$

The SNR of the peak is estimated with equation 5.3, where $C_{12}(\tau)$ is the estimated cross-correlation between the sensors, and $C_{12}([\tau_{n1}\ \tau_{n2}])$ is a slice of the cross-correlation containing no EGF peaks. For this specific geometry, the noise slice is taken from -1 to 1 second.

$$\text{SNR} = \frac{C_{12}(\tau_{\text{peak}})}{\text{std}(C_{12}([\tau_{n1}\ \tau_{n2}])} \tag{5.3}$$

The signal rms bandwidth, $\Delta\omega_{\text{rms}}$, is estimated for each cross-correlation peak with equations 5.4 - 5.6, where $S_{12}(\omega)$ is the power spectra given by $S_{12}(f) = |\mathcal{F}\left\{C_{12}(\tau)\right\}|^2$, and $\mathcal{F}\left\{\cdot\right\}$ denotes the Fourier transform [93, p. 186].

$$(\Delta\omega_{\text{rms}})^2 = \overline{\omega^2} - \overline{\omega}^2 \tag{5.4}$$

$$\overline{\omega} \equiv \frac{\sum_i \omega_i \times |S_{12}(\omega_i)| d\omega}{\sum_i |S_{12}(\omega_i)|} \tag{5.5}$$

$$\overline{\omega^2} \equiv \frac{\sum_i \omega_i^2 \times |S_{12}(\omega_i)| d\omega}{\sum_i |S_{12}(\omega_i)|} \tag{5.6}$$

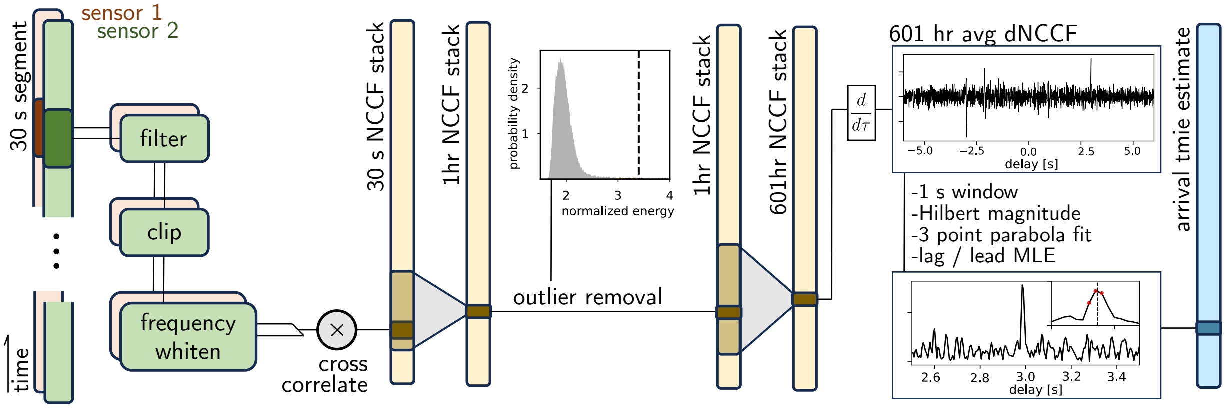

Figure 5.2: Signal processing block diagram for computing the cross-correlation of ambient noise and estimated the arrival time of the surface reflection acoustic path

Assuming that current is negligible, the lag and lead estimates of the acoustic arrival time represent two independent observations of the acoustic arrival time. In the following section, we derive an estimator that gives the maximally likely value of the arrival time given two independent observations, with given standard deviations, of the arrival time. A diagram of the problem is shown in figure 5.3. In figure 5.3, the orange and blue curves represent the probability distribution of the two arrival time estimates. The black dashed line represents the new distribution for arrival time given the two observations.

The estimated lag arrival time can be modelled as a Gaussian random variable with mean τ_1 and standard deviation σ_1. The estimated lead arrival time can be modelled as a single observation of a Gaussian random variable with mean τ_2 and standard deviation σ_2. The individual probability distribution functions are given in equations 5.7 and 5.8

$$f_{\tau_1} \sim \mathcal{N}(\tau_1, \sigma_1) = \frac{1}{\sqrt{2\pi}\sigma_1} e^{\frac{-(\tau-\tau_1)^2}{2\sigma_1^2}} \tag{5.7}$$

$$f_{\tau_2} \sim \mathcal{N}(\tau_2, \sigma_2) = \frac{1}{\sqrt{2\pi}\sigma_2} e^{\frac{-(\tau-\tau_2)^2}{2\sigma_2^2}} \tag{5.8}$$

Given a single observation τ_1 and τ_2, the log-likelihood function of the arrival time, is $L = \ln(f_{\tau_1} \times f_{\tau_2})$, and is given in equation 5.9. The maximally likely value of τ can be solved by maximizing equation 5.9. Since L is concave, the maximum is equal to when $\frac{\partial L}{\partial \tau} = 0$, which gives the equation for the maximally likely arrival time in equation 5.10

$$L(\tau, \tau_1, \tau_2, \sigma_1, \sigma_2) = \log\left(\frac{e^{-\frac{(-\tau+\tau_1)^2}{2\sigma_1^2}}}{\sqrt{2\pi}\sigma_1}\right) + \log\left(\frac{e^{-\frac{(-\tau+\tau_2)^2}{2\sigma_2^2}}}{\sqrt{2\pi}\sigma_2}\right) \tag{5.9}$$

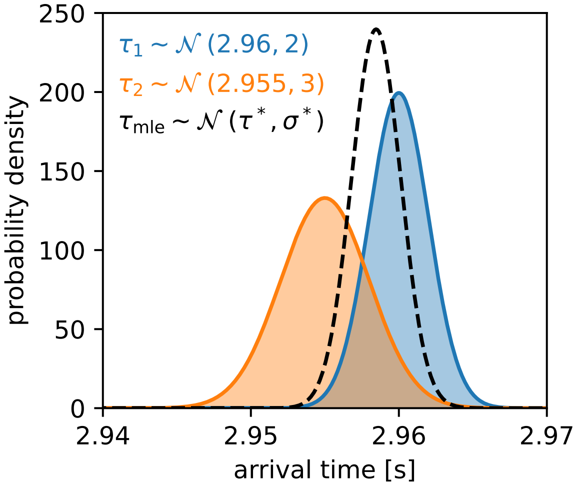

Figure 5.3: Diagram of the maximum likelihood estimator. The blue distribution represents the possible values that the lag arrival time could be, and the orange distribution represents the possible values that the lead arrival time could be. When the information from both observations is combined, you get the distribution represented by the black dashed line. The Gaussian distributions are represented with the notation $\sim \mathcal{N}(\mu, \sigma)$, where μ is the mean and σ is the standard deviation. For τ_1 and τ_2, the mean is given in seconds and the standard deviation is given in milliseconds.

$$\tau^* = \frac{\sigma_1^2 \tau_2 + \sigma_2^2 \tau_1}{\sigma_1^2 + \sigma_2^2} \tag{5.10}$$

The fisher information of the maximum likelihood estimate is given by equation 5.11

$$I = -E\left[\frac{\partial^2 L(\tau, \tau_1, \tau_2, \sigma_1, \sigma_2)}{\partial \tau^2}\right] = \frac{1}{\sigma_1} + \frac{1}{\sigma_2} \tag{5.11}$$

From the Cramér–Rao bound, the lower bound on the variance of the estimator is given by the inverse of the Fisher information. Since these are Gaussian processes, the variance of the estimator is therefore given by the inverse of the Fisher information [71, p. 419]. So the standard-deviation of the arrival time estimate is given in equation 5.12.

$$\sigma_\tau^* = \sqrt{\frac{1}{I}} = \frac{\sigma_1 \sigma_2}{\sqrt{\sigma_1^2 + \sigma_2^2}} \tag{5.12}$$

5.3 Comparing estimated acoustic arrivals to simulation

5.3.1 Simulation methods

Acoustic propagation between the two hydrophones is simulated using the method of normal modes [67] and is calculated with KRAKEN [104]. The environment is simplified to be range independent, with the two hydrophones located at the same depth. The ocean depth is set to 1525 m, and the two hydrophones are placed at 1524 m, and separated by 3.186 km. The Green's function is simulated for frequency bins corresponding to a sequence 30 seconds long, sampled at 200 Hz in the time domain. The resulting time-domain Green's function is filtered between 1-90 Hz. The arrival time is estimated with quadratic peak interpolation [136] of the analytical signal magnitude. To simulate the effect of temperature and salinity changes in the water column, the 1-day average sound speed profile was calculated from HYCOM temperature and salinity data at (45.944335 -129.990713), which is 325 m from the midpoint between the two hydrophones. Figure 5.4(a) shows the daily surface-reflected arrival time simulated with HYCOM sound speeds and the method of normal modes.

The two hydrophones are located in the caldera of an active volcano, that inflates and deflates with eruptions [20, 99]. To simulate the effect of depth changes, the time-domain Green's function was simulated for depth changes of 1 to 5 meters for each hydrophone and a fixed sound speed. The arrivals times from this simulation are shown in 5.4(b). Since the changes to depth are small relative to the hydrophone separation and ocean depth, the effect of depth changes is linear. A linear regression model is fit to the simulated changes in arrival time with an R2 score of 0.9956. This allows for the individual pressure measurements from each sensor to be used to characterize the change in arrival time due to changes in depth for the two hydrophones. Pressure sensors that are collocated with the hydrophones are used to measure the depth of the two hydrophones [102, 103]. These depth measurements are shown in figure 5.4(c). The simulated surface-reflection arrival time is updated using the linear model. The 601-hour average, simulated arrival time with and without the depth adjustment is shown in 5.4(d). The simulated arrival times used in the main text include the depth adjustment.

5.3.2 Estimated acoustic propagation

The single surface-reflection acoustic arrival time is estimated with ambient sound and compared to simulated acoustic arrival times. The simulated acoustic arrival times use daily sound speed information from the HYCOM ocean mode [66]. The simulated arrival times are then re-averaged to 601 hours to match the estimated arrival times from ambient sound. Figure 5.5(a) shows the empirical probability density of the difference between the simulated acoustic arrival and the estimated acoustic arrival, and a Gaussian distribution fit to the data to minimize least squares. There is a constant offset of 3.63 ms, which corresponds to an acoustic path length difference of 5.4 m. This discrepancy is likely due to imperfect knowledge of the hydrophone geometries. Figure 5.5(b) shows the surface reflection arrival

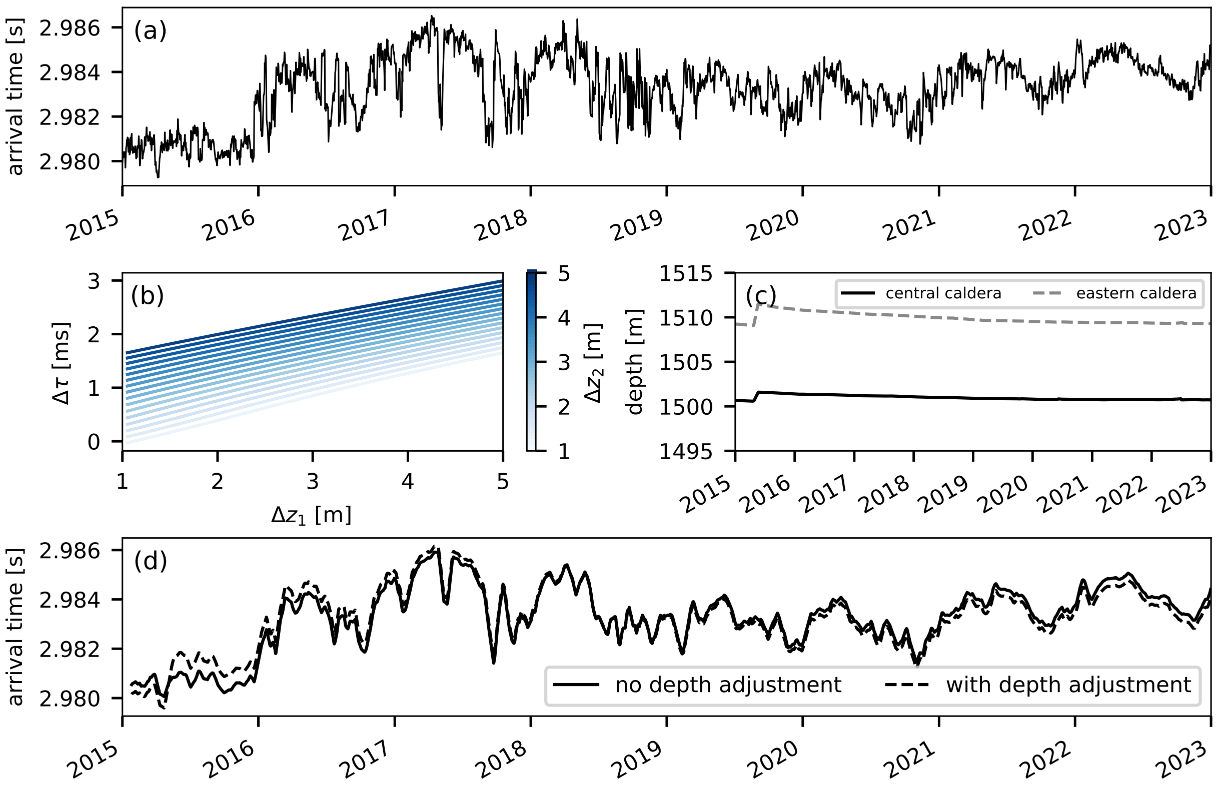

Figure 5.4: (a)Daily surface-reflected arrival time simulated with the method of normal modes. (b) Changes in surface reflection arrival time due to changing depths of the two sensors. (c) 601 hour averaged depth of the two sensors, measured by colocated pressure sensors. (d) 601 hour surface reflected arrival time with and without depth adjustment.

time estimated from ambient sound and the simulated arrival time from 2015 to 2023. The constant offset of 3.63 ms is removed from the simulated data. The color shading represents the standard deviation of the measurement, estimated from the signal-to-noise ratio, signal bandwidth, and maximum likelihood estimator (see section 5.2.1 for more information). The estimated standard-deviation of the arrival time estimate considers the estimation of the arrival time in noise, but does not include any considerations to arrival time offsets due to non-diffuse sound source distributions. The root-mean-squared difference, between the simulated and estimated acoustic arrival time is 1.06 ms.

The simulated and estimated acoustic arrival times are highly consistent, with the standard deviation of the difference, (figure 5.5(a)), being 1 ms. In 2015, there is a faster arrival (corresponding to a warmer water column), in both the simulated and estimated arrival times. This is consistent with the 2015 north-east pacific marine heat wave [32, 60]. Additionally, the decreased arrival time fluctuations between 2019-2021 seem to be represented

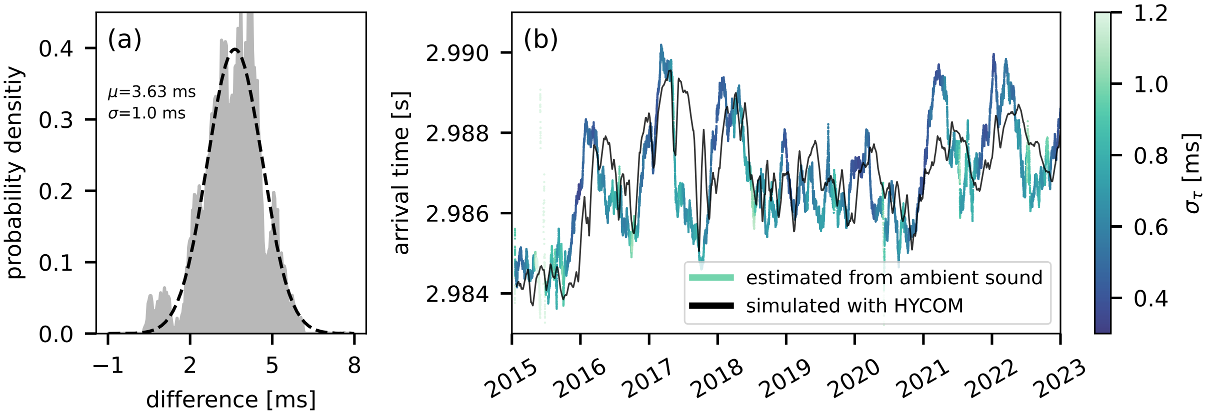

Figure 5.5: (a) distribution of the difference between passive arrival time estimates from ambient sound and simulated arrival times using HYCOM and the method of Normal Modes. (b) Arrival times estimated from ambient sound (blue) and simulated with the HYCOM ocean model (black) with the constant offset removed. Shading in the estimated arrival time represents the standard deviation of the estimate.

by both HYCOM and the passive estimate of the acoustic arrival time. There are also times when the simulated and estimated arrivals are not consistent. In the second half of 2017, the HYCOM arrival time and passive acoustic arrival diverge, and between 2021 and 2023, there seems to be more fluctuation in the passively estimated arrival time than in HYCOM. Since we don't have a perfect ground truth measurement of the ocean state, it is impossible to know if these discrepancies are due to errors in HYCOM, errors in the passive estimate of the acoustic arrival time, or both.

5.4 Passive acoustic thermometry

Changes in the surface reflection arrival time correspond to an observation of changes in the integrated sound speed along the acoustic ray path, which is almost entirely linearly driven by water temperature [77]. As shown in figure 5.1(b), due to the small sensor separation relative to the ocean depth, refraction of the acoustic rays is negligible. Because of this, for this specific geometry, the integrated water temperature along the acoustic ray path is equivalent to the depth-averaged water temperature.

We propose a linear inversion model that relates the change in surface reflection arrival time to the change in the depth averaged water temperature. We use the acoustic simulation described in appendix section 5.3.1 to design and evaluate this model. Figure 5.6(a) shows the simulated surface reflection arrival times for daily HYCOM sound speed profiles plotted against the depth-average water temperature. The red line shows the linear model that is fit to the data, which as an R2 score of 0.987, meaning that 98.7 % of the variance in arrival time changes is driven by linear fluctuations in the depth averaged water temperature. To evaluate the inversion model, the depth-averaged water temperature is estimated from the simulated surface-reflected acoustic arrival time, and compared to the actual HYCOM depth-averaged water temperature used to simulate the acoustic arrival time. This is shown in figure 5.6(b).

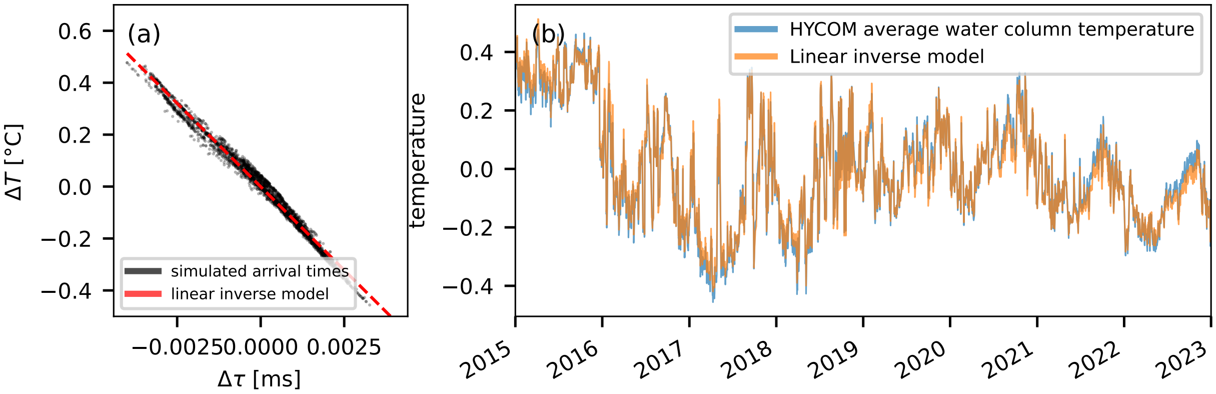

Figure 5.6: (a) simulated surface reflection arrival time fluctuation (x-axis) plotted against the depth-averaged water temperature fluctuation (y-axis).The simulated data is shown in black, and the proposed linear inverse model, fit to the data, is shown with the dashed red line. (b) depth-averaged water temperature from HYCOM (blue) and the estimated depth-averaged water temperature, estimated from the simulated acoustic arrival time and proposed linear inverse model (orange)

Figure 5.7(a) shows the depth-averaged water temperature estimated from the ambient sound field, the depth-averaged water temperature from HYCOM, and the depth-averaged water temperatures measured by ARGO floats when one is near the hydrophones. Figures 5.7(b)-(d) show three different zoomed in sections of the time series. The estimates of the depth-averaged water temperature from ambient sound represent a 601-hour average of the water column temperature (corresponding to the integration time required for the EGF to emerge from the cross-correlations). The HYCOM depth-averaged water temperature is also averaged to 601 hours. Because of the sparse nature of the ARGO data, these measurements are not averaged in time. The RMS difference between the passive acoustic estimate of depth-averaged water temperature and the ARGO float measurements is 0.086 °C. The RMS difference between the ambient sound estimate and ARGO measurements is estimated for the times that an ARGO float is nearby. The RMS difference between the passive acoustic estimate of depth-averaged water temperature and the HYCOM water temperature is 0.13 °C. The RMS difference between HYCOM water temperature and the ambient sound estimate is calculated using the full eight years of data. The RMS difference between the ARGO data (which is assimilated into HYCOM), and the HYCOM data is 0.053 °C. Interestingly, in figure 5.7(b) and 5.7(c), the ARGO measurement seems to follow HYCOM more closely, but in figure 5.7(d) the ARGO measurement seems to follow the ambient sound estimate more closely.

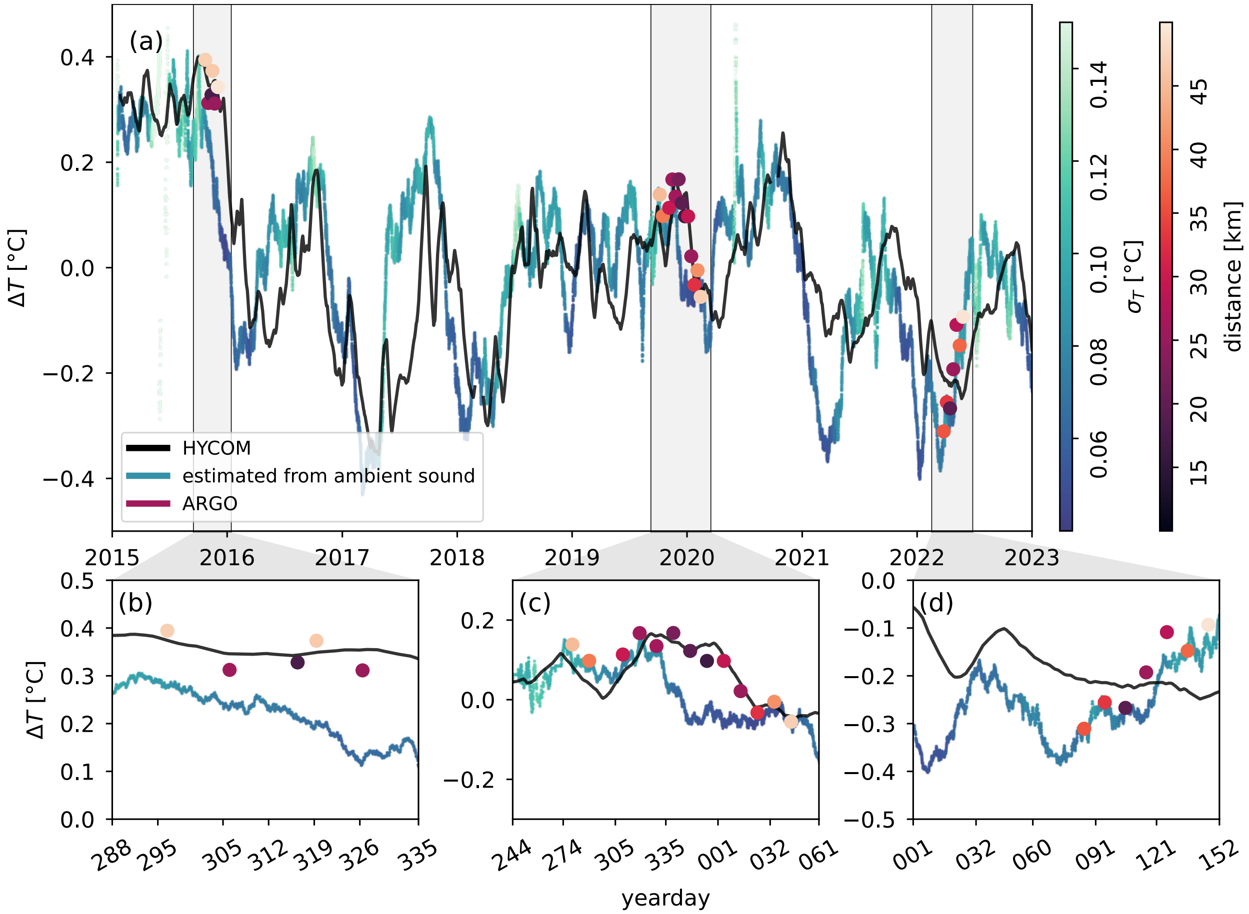

Figure 5.7: Depth-averaged water temperature estimated from ambient sound (blue), HYCOM (black), and measured by ARGO floats (red). The shading of the ambient sound estimate in blue indicates the standard deviation of the estimate in degrees Celsius. The shading of the ARGO temperature data in red indicates the distance of the ARGO float profile measurement from the midpoint of the hydrophones. (a) Shows the depth-averaged temperature from 2015-2023. (b)-(d) show zoomed in sections of the time-series when ARGO data is present.

The averaging time used for the passive acoustic water temperature estimation is 601 h, or about 25 days. This was chosen to resolve timescales approximately on the order of 1 month. Figure 5.8 shows the accuracy of arrival time and depth-averaged water temperature as a function of averaging time. This indicates this method could reliably resolve timescales on the order of 150 h, depending on the desired accuracy.

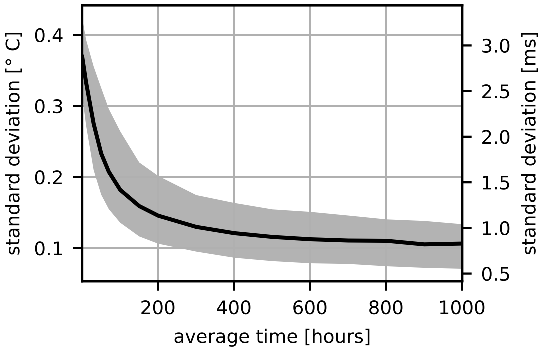

Figure 5.8: Standard deviation of the estimate of depth-averaged temperature (left axis) and surface reflection arrival time (right axis) estimated from ambient sound at different average times. The solid black line represents the 50th percentile of the standard deviation for the 8 years of arrival times. The shaded region represents the 10th and 90th percentiles.

5.5 Conclusion

In this work we have demonstrated the feasibility of using ambient sound and bottom mounted hydrophones to observe changes in depth-averaged deep ocean water temperature, using surface reflected acoustic paths between closely spaced ($\sim 3\,\text{km}$), bottom-mounted hydrophones. We are able to estimate the acoustic travel time with high accuracy ($\sim$ 1 ms) and can resolve sub-seasonal changes in the water column. Additionally, our estimates are consistent with the HYCOM ocean model and ARGO measurements. The RMS difference between ARGO measurements and the passive acoustic estimates of water column temperature are 0.086 °C, and the RMS difference between the HYCOM ocean model and the passive acoustic estimates of water column temperature are 0.13 °C. With the demonstration that this is feasible, further experimental work is needed to better evaluate the accuracy and robustness of ambient noise interferometry for local, deep ocean acoustic thermometry. Passive acoustic based observations are a complimentary method of observing the ocean to in-situ based measurements such as ARGO floats. Passive acoustic measurements of local, deep ocean temperature, such as those presented in this work, have less accuracy than ARGO measurements, but have a significantly higher time resolution and represent measurements for a fixed sensing configuration. These measurements could eventually be used alongside in-situ measurements for data assimilation into global ocean models such as HYCOM, notably in areas not well sampled by ARGO floats such as coastal or polar regions.

There are several areas of further investigation that present the possibility of increasing the accuracy and robustness of this technique for measuring deep ocean temperature. The work presented here uses a single pair of hydrophones, but by using arrays of hydrophones, it is possible to significantly increase the accuracy of the measurements and reduce the integration time required for the emergence of the EGF [173, 38, 94]. It has also recently been shown that vector acoustic sensors can dramatically decrease the averaging time needed for accurate estimates [95]. Additionally, further work in developing processing algorithms that selectively filter diffuse sound [144, 84, 74], could increase accuracy, decrease averaging time, and provide more accurate error bounds on oceanographic variable estimates.

Ambient sound has been named an essential ocean variable [150, 149], and there is increased interest and support to increase the global coverage of passive acoustic monitoring (PAM) of the ocean. With further developments in ambient noise interferometry, this technique could be leveraged with existing and proposed cabled ocean observatories and the proposed SMART cable sensors [63, 118] to measure oceanographic variables, which would increase the spatial and temporal density of deep ocean observations. Using the technique of ambient noise interferometry with existing and future PAM arrays would allow for the simultaneous measurement of acoustic soundscapes, critical to understanding anthropogenic sound and biology such as marine mammals, and oceanographic variables such as seawater temperature, critical to our ability to understand and appropriately react to the changing climate.

Chapter 6

OCEAN BASIN ACOUSTIC RECEPTIONS WITH THE KAUAI BEACON AND OOI HYDROPHONES

Abstract

Acoustic receptions from the Kauai Beacon (KB), measured by the open-access Ocean Observatories Initiative (OOI) hydrophones are explored in this work. The OOI cabled ocean observatory has 11 hydrophones that record the ambient sound scape and have the potential to be used along with ocean basin acoustic transmissions to measure ocean basin acoustic propagation, which can be used to infer information about oceanographic variables, such as deep ocean temperature. The acoustic arrivals at all of the OOI hydrophone locations are simulated and compared to the receptions over the first year of regular Kauai Beacon transmissions, from March of 2023 to March of 2024. The coherence of specific acoustic arrivals is presented over the course of a single transmission and a single day. Lastly, a discussion of the potential use of the KB with OOI hydrophones is discussed.

6.1 Introduction

The Kauai Beacon (KB) is a source off the coast of Kauai that transmits a maximum length sequence (MLS) encoded signal. Previous work has demonstrated that ocean basin acoustic transmissions can be used to observe ocean basin temperature and other oceanographic variables [34, 26, 36, 174]. With the KB transmitting a 20 min signal every four hours every fourth day, it stands to serve as a data of opportunity for any passive acoustic monitoring infrastructure located within acoustic paths from the source. In this chapter, positive receptions of the KB by Ocean Observatories Initiative (OOI) hydrophones are analyzed for the first year of transmissions. The vertical structure of simulated acoustic arrivals for various OOI hydrophone locations is studied, and positive receptions are compared to simulated arrivals for the first year of operation. Lastly, the coherence of specific acoustic arrivals during a 20 min transmission and throughout a day is discussed.

Much of the previous work exploring ocean basin acoustic propagation and its utility to-

Table 6.1: Table of OOI hydrophone depths, great circle distance from the Kauai beacon, simulated transmission loss, and if a positive reception is seen in the data. The transmission loss is averaged over the bandwidth of the beacon (37.5 - 112.5 Hz). The type of hydrophone indicates if it samples at 64 kHz (BB) or 200 Hz (LF).

hydrophone	abbreviation	depth (m)	range (km)	type	TL [dB]	reception
Central Caldera	AXCC1	1527	3739.6	LF	105.39	yes
Axial Base	AXBA1	2608	3748.6	LF	107.79	yes
Eastern Caldera	AXEC2	1518	3740.9	LF	104.75	yes
Southern Hydrate	HYS14	774	3988.4	LF	102.28	yes
Oregon Slope Base	HYSB1	2907	3967.2	LF	108.50	no
Axial Base	LJ03A	2598	3747.2	BB	107.79	yes
Axial Base (200m)	PC03A	190	3747.2	BB	105.53	yes
Oregon Offshore	LJ01C	582	3992.2	BB	103.09	yes
Oregon Shelf	LJ01D	81	4051.5	BB	102.41	no
Oregon Slope Base	LJ01A	2888	3968.6	BB	108.45	no
Oregon Slope Base (200m)	PC01A	195	3968.6	BB	106.18	yes

wards ocean acoustic thermometry has made use of large hydrophone arrays (either vertical or or horizontal line arrays) [175, 24, 36, 34]. In this chapter, I focus on single hydrophone observations. Using single hydrophones reduces the possible processing gain and subsequently the signal-to-noise ratio of receptions. Additionally, any spatial information about the reception, such as depth structure or arrival angle is lost. However, single hydrophone observations significantly reduce the complexity of the hardware required for receptions, and could allow for a vast network of acoustic receivers, which could contribute larger spatial sampling of the environment.

6.2 Ocean Observatory Initiative Hydrophones

The Ocean Observatories Initiative (OOI) has eleven cabled hydrophones that are continuously measuring the ambient soundscape. The top panel of figure 6.1 shows the locations of the 11 hydrophones and the abbreviations used within this chapter. The lower panel of figure 6.1 shows the transmission loss from the Kauai Beacon to the central caldera hydrophone, which is 3739 km from the KB source. For more information on the acoustic modelling methods, see section 6.3.2. Table 6.1 gives the hydrophone names, depths, simulated transmission loss, and whether there are positive receptions of KB for every OOI hydrophone.

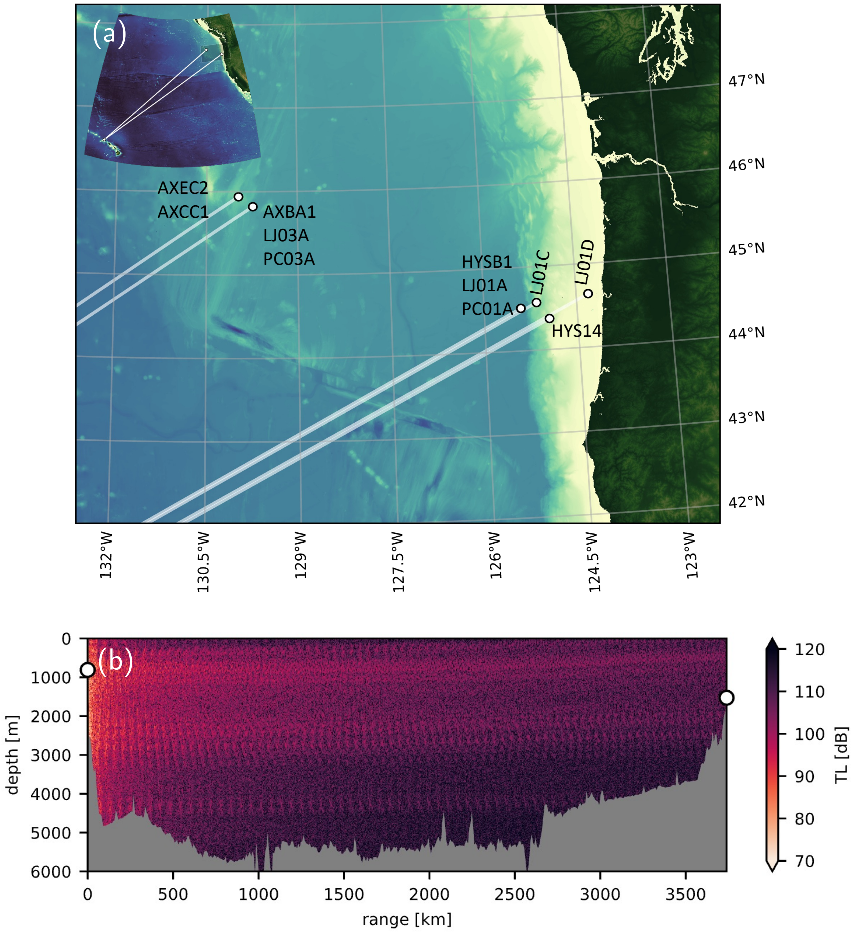

Figure 6.1: (a) Map of OOI hydrophones, in relation to the Kauai Beacon. (b) Simulated transmission loss from the Kauai beacon to the central caldera hydrophone, simulated with the parabolic equation. Transmission losses for other OOI hydrophones have similar structure.

6.3 Methods

In the following sections, the signal processing and acoustic modelling methods used in the following analysis are described.

6.3.1 Signal processing

For every transmission of the KB, two hours of ambient sound data is pulled from each of the eleven OOI hydrophones. For broadband hydrophones, the acoustic data is decimated to a sampling rate of 500 Hz. The data is then zero-meaned and clipped to ± 4 standard deviations for a specific 2-hour data segment. This helps remove large spurious events such as colocated sensor noise or nearby fin whale vocalizations that might degrade the KB reception. Then, each acoustic data stream is matched filtered with the MLS signal replica, and the data is converted to an analytical signal using the Hilbert transform.

An approximate absolute arrival time, (T_0), is estimated using the integrated, range-dependant group-velocity, which is solved for using the method of normal modes, and sound speed profiles from WOA climate temperature and salinity profiles [77, 112]. For section 6.5, all the complex, match filtered, 27.28 s data segments between T_0 and $T_0 + 1200s$ (20 min) are averaged together, to create a single 20 min average reception. For section 6.6, a moving average of 5, 27.28 s segments is used.

For a specific reception, peaks are estimated from the data using the complex envelope of the signal and a simple peak fitting algorithm* that looks for local maxima. The signal-to-noise ratio of the peak is estimated with equation 6.1, where $\tilde{p}(t)$ is the Hilbert transform of the match filtered and circular stacked reception, $\tilde{p}_{noise}(t)$ is a 5 s slice of $\tilde{p}(t)$ containing no receptions, and rms is the root-mean-squared value. The noise slice region for each location is hand chosen to not include the reception.

$$\text{SNR} = \frac{|\tilde{p}(T_{\text{peak}})|}{\text{rms}(\tilde{p}_{noise}(t))} \tag{6.1}$$

6.3.2 Acoustic simulation

The acoustic simulations in this chapter were computed using the parabolic equation (PE) method [22], which is numerically simulated with a modified version of RAM†. The bathymetry data used is from GEBCO 2023 and the sound speed data is computed from the WOA 2023 climate model. The acoustic arrivals were simulated using PE and Fourier synthesis. The time domain arrivals were simulated with a time width of 10 s, a sampling rate of 300 Hz, and a bandwidth between 37.5 - 112.5 Hz, which is the same bandwidth of the KB signal. The PE runs were conducted with a range step of 10 m ($\sim \frac{\lambda}{2}$), and a depth step of 2 m ($\sim \frac{\lambda}{10}$). The vertical structure is simulated using the WOA climate model, and the arrival dot plots throughout the year are simulated using the WOA monthly profiles.

6.4 Simulated vertical arrival structure

In this section, the vertical structure of the acoustic arrivals for all the OOI hydrophone locations is simulated, which provides a greater context to which parts of the acoustic basin transmission are received by the different hydrophone locations and depths.

The arrival structure for long-range acoustic propagation in the deep ocean varies significantly for the specific source, receiver geometry and environmental sound speed structure. In

---

[*] see python function scipy signal findpeaks

[†] `https://oalib-acoustics.org/models-and-software/parabolic-equation/`

general however, deep ocean receptions (where there is limited interaction with the bottom for the receiver), the earliest arrivals will correspond to steeper angle (higher mode order) propagation. The higher modes have a higher group velocity and include energy in shallower waters, which will fluctuate more with seasonal temperature changes. The later arrivals correspond to shallow angle receptions (lower mode order) propagation. This energy will, in general, be less sensitive to seasonal temperature fluctuation than the shallower waters sampled by the steeper angle propagation [175]. Of the 11 OOI hydrophones, only two are moored within the water column (PC01A and PC03A). The rest of the hydrophones are bottom mounted at various depths. This results in the acoustic receptions containing various levels of bottom interaction at the receiver, which will complicate the structure of the arrival pattern.

Figure 6.2 shows the simulated acoustic arrivals for the different OOI hydrophone locations. For a detailed description of how the acoustic arrivals were simulated, see section 6.3.2. The time axis of figure 6.2 is the circular time, which spans from 0 - 10 s and repeats. The horizontal lines represent the depths of the OOI hydrophones.

The arrival structure for the Axial Base and Oregon Slope Base (figure 6.2(b)(c)) consist of typical deep ocean receptions, with limited bottom interaction at the receiver. The central caldera hydrophones, which are mounted at the top of the Axial Seamount at a depth of $\sim 1500\,\text{m}$, contain later receptions (after about 5 seconds), which are consistent with the lower modes of long-range, deep ocean propagation. The receptions between 3 and 5 seconds is characteristic of bottom interacting acoustic energy. The Oregon Offshore (LJ01C), Oregon Shelf (LJ01D), and Southern Hydrate (HYS14) are located at various depths on the continental shelf. The Oregon Offshore and Southern Hydrate locations are close in depth to the sound speed minimum, and thus will receive the lower order modes, but also contain significant interaction with the bottom at the receiver location.

The simulated arrivals in figure 6.2, are simulated using the WOA 2023 climate model, which does not contain seasonal fluctuations in temperature or salinity. Additionally, the simulation does not include perturbations in the sound speed due to internal tides. Internal tides can have a significant effect on long-range, low-frequency acoustic propagation in the ocean [23, 25]. Specifically, they can scatter acoustic energy between modes. This increases the complexity of separating lower order modes and estimate the channel group velocities because energy received in mode 1 receptions may have spent some time propagating in a different mode [175]. Exploration of the effects of internal tides for OOI hydrophone locations and how they might affect ocean basin tomography is left for future work.

6.5 Arrivals measured by OOI hydrophones

Figure 6.3 shows a dot plot of measured and simulated acoustic arrivals for all the OOI hydrophones that have positive receptions. The simulated arrivals are computed with the parabolic equation and Fourier synthesis (using a time width of 10 s). For more information about the acoustic modelling, see section 6.3.2. The arrivals are simulated for each monthly

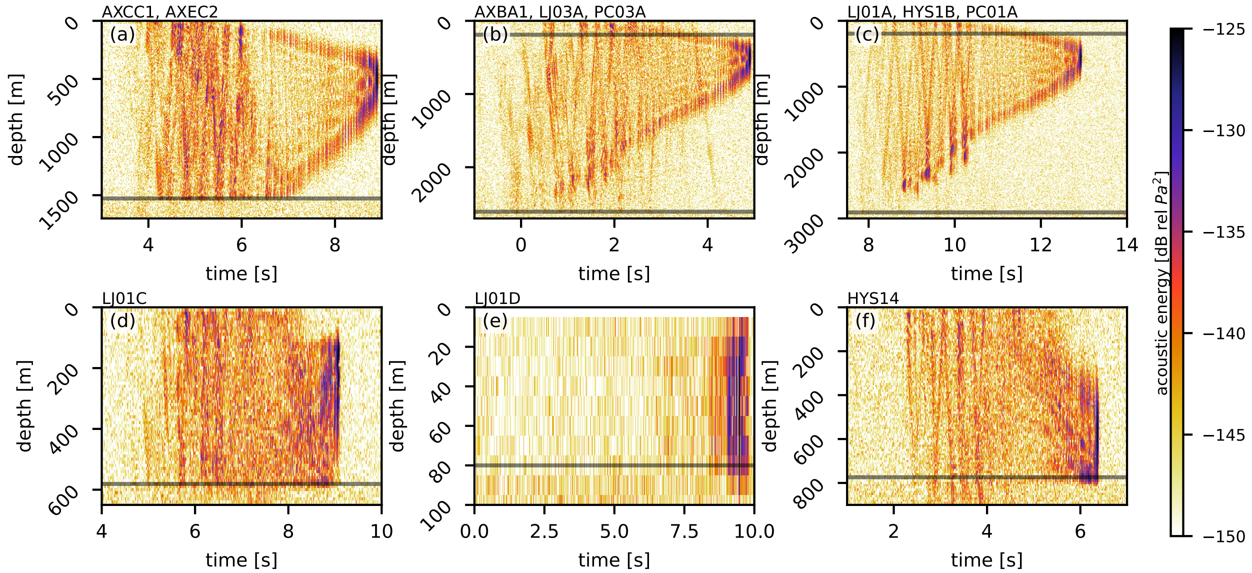

Figure 6.2: (a)-(f) Simulated vertical arrival structure for OOI hydrophone locations. The horizontal grey lines represent the depths of OOI hydrophones.

profile in WOA, and the associated dots are repeated 8 times a month, corresponding to the number of days a month that the KB transmits. The size of each dot is proportional to the signal-to-noise ratio for the measured receptions, and the reception amplitude for the simulated arrivals. The SNR / amplitude scaling is adjusted for each figure so that the receptions are visually the most clear. For each location, the y-axis corresponds to circular time. Due to the MLS pulse compression, the circular time of the actual receptions repeats every 27.28 s. The PE simulated arrivals repeat every 10 s. Except for the Southern Hydrate (HYS14) location, the circular time scaling between the measured and simulated arrivals is consistent. However, several of the simulated and measured acoustic arrivals have an offset in circular time. This could be caused by differences between the actual ocean state and the WOA climate model, or some other acoustic phenomena. Exploring these discrepancies is left for future work.

All the positive receptions in figure 6.3 share the feature that the later arrivals in circular time, corresponding to lower mode order acoustic propagation, consist of scattered energy, where there is limited or no distinct peaks over the course of the year of receptions. However, several of the hydrophone locations are able to distinguish consistent acoustic paths that are present in some or all of the first year of transmissions. These peaks can be found for the central and eastern caldera hydrophone between 2.5 and 4 seconds, between 21 and 23 seconds for the slope base (200m) location and between 7.5 and 9 seconds for the axial base (200m) location. The axial base (lf) hydrophone is bottom mounted and is behind the Axial Seamount relative to the Kauai Beacon. Even though the received acoustic energy is less at the Axial Seamount bottom mounted hydrophones, the ambient sound levels are also quieter (see chapter 2), which makes the reception possible. Between June and December, there was an issue with the OOI broadband hydrophone data, which made this data partially or completely unusable. It is not completely known if the decrease in reception SNR at the two 200m moored hydrophones after December 2023 is due to a physical decrease in SNR, or a corruption of the OOI data. The Southern Hydrate hydrophone consistently gets a high SNR reception, but a clock drift issue can clearly be seen in figure 6.3(g). If this hardware issue could be resolved, the Southern Hydrate hydrophone could also be utilized for receptions of the Kauai Beacon.

The consistent acoustic arrivals that are visible in figure 6.3(a)(b)(e)(f) have the potential to be used for conventional acoustic tomography methods, such as those previously used in the northeast Pacific [35]. Even though the later arrivals consist of scattered acoustic energy, where separating individual modes is obscured by scattering caused by internal tides [175], they do still carry information about the ocean basin. In future work the full arrival structure (including scattered regions) could potentially be used along with statistical estimation techniques to invert for information about the ocean basin.

6.6 Coherence time of specific arrivals

In section 6.5, 20 min average receptions of the KB are considered over the course of the first year of KB operation. In this section, the reception variability over the course of a single transmission and day is explored. Figure 6.4 shows the receptions by the Oregon Offshore hydrophone for two separate days (4/23/2023, and 5/1/2023). Each dot represents a reception with 2.3 min of averaging (5 MLS lengths). The different rows represent the different transmissions throughout the day and the color of the dots represents the SNR of the reception.

Over the course of a 20 min transmission, some acoustic arrivals are coherent during the full reception and some come into or out of coherence. Additionally, for a coherent arrival, the arrival time fluctuates throughout the 20 min. Since both the KB and the LJ01C hydrophone are bottom mounted, the fluctuations in arrival time are caused by a change in integrated sound speed during the 20 min transmission.

Additionally, the locations of strong SNR acoustic arrivals are not consistent between adjacent receptions (separated by 4 hours). As shown in figure 6.3, some OOI hydrophones do see some consistent arrivals throughout the year (most clear at the Central and Eastern Caldera hydrophones). But, even at these locations, most of the receptions appear stochastic within the reception window of several seconds. This is consistent with previous experimental results, and simulated acoustic propagation [36, 175].

One of the unique aspects of ocean basin acoustic tomography is its ability to measure vast spatial scales with high time resolution. Better understanding the small time scale fluctuations of acoustic arrivals due to internal tides or other mechanism is a promising area of future exploration.

6.7 Conclusion

After an approximate 20-year hiatus, the Kauai Beacon has begun regularly transmitting a thermometry signal once again. Since 2005, there has been a significant increase in open-access, passive acoustic monitoring infrastructure such as OOI, Ocean Networks Canada[‡], and CTBTO hydrophones[§]. Existing and future PAM infrastructure can be leveraged alongside the KB to further our understanding of long-range acoustic propagation and be used to make integrated ocean basin temperature observations. In this chapter, a year of receptions by OOI hydrophones is presented and compared to simulated receptions.

Receptions are simulated as a function of depth and time to better understand how the depths of the OOI hydrophones sample the arrival structure. Consistent receptions of the KB are observed by 8 of the 11 OOI hydrophones, over the first year of transmissions. Coherent arrivals, which correspond to the simulated arrival structure can be seen in the Eastern Caldera, Central Caldera, Slope Base (200m), and Axial Base (200 m) hydrophones. Lastly, the coherence of individual acoustic paths over the course of a 20 min transmission and across a single day are presented. For the timescale of 20 min, acoustic arrivals show clear coherence. At time scales of 4 hours to 1 days, the vast majority of single peak arrivals are not coherent. However, some paths are coherent on longer timescales (up to 1 year and longer) as seen in figure 6.3. This work lays the necessary foundational analysis to use the KB as a source of opportunity along with OOI hydrophones to further study long-range acoustic propagation and its utility towards estimating oceanographic variables such as deep ocean temperature.

[‡] https://www.oceannetworks.ca/

[§] https://www.ctbto.org/our-work/monitoring-technologies/hydroacoustic-monitoring

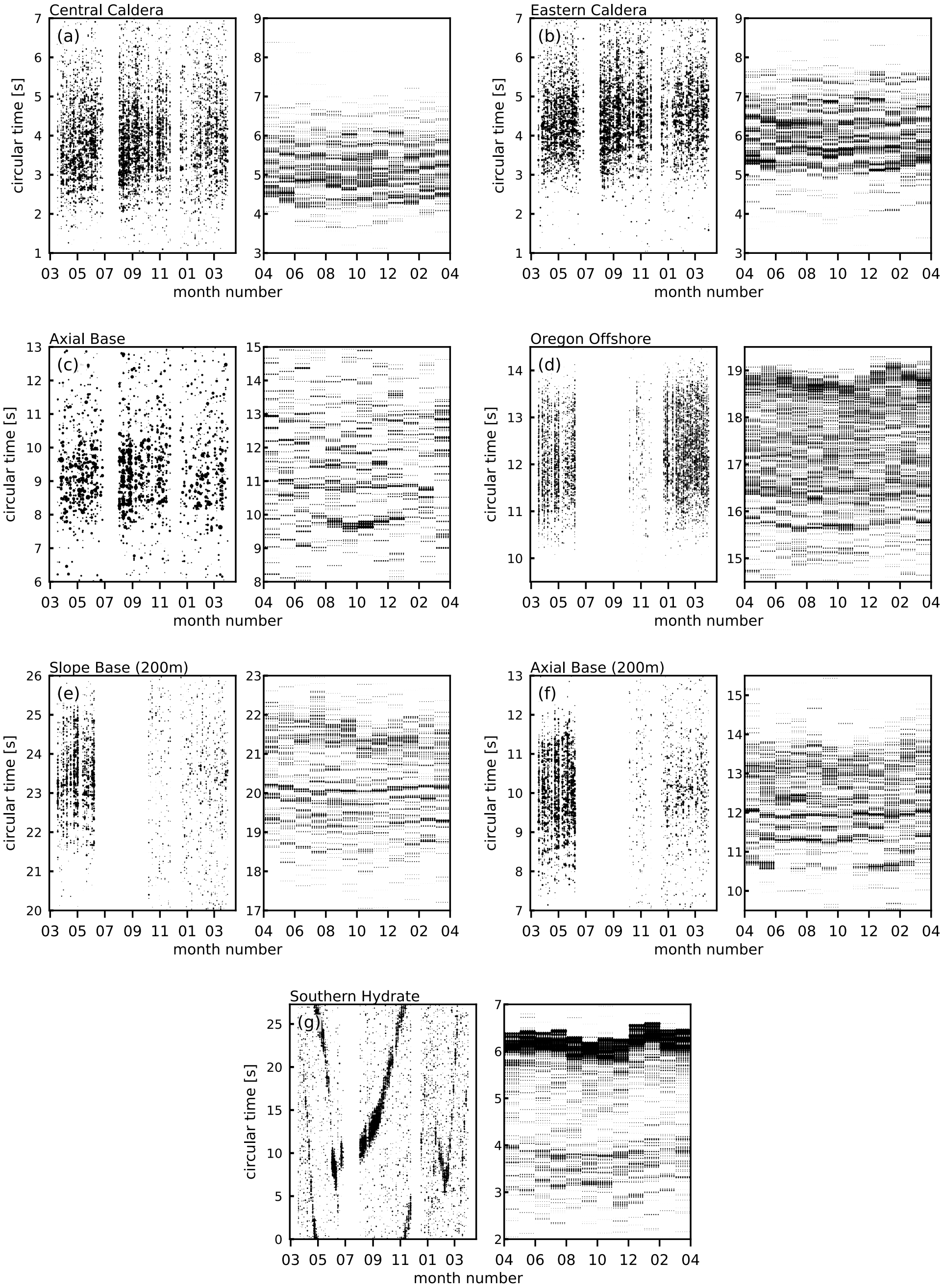

Figure 6.3: Receptions of the Kauai Beacon by OOI hydrophones over the first year (March 2023 to March 2024) of regular transmissions. Each panel represents a different hydrophone location. The left sub-panel shows the receptions measured by the hydrophones and the right sub-panel shows the monthly simulated arrival pattern (simulated with PE). (a)(b)(c) and (g) are low frequency (sampling rate of 200 Hz) hydrophones. (d)(e)(f) are broadband (sampling rate of 64 kHz) hydrophones.

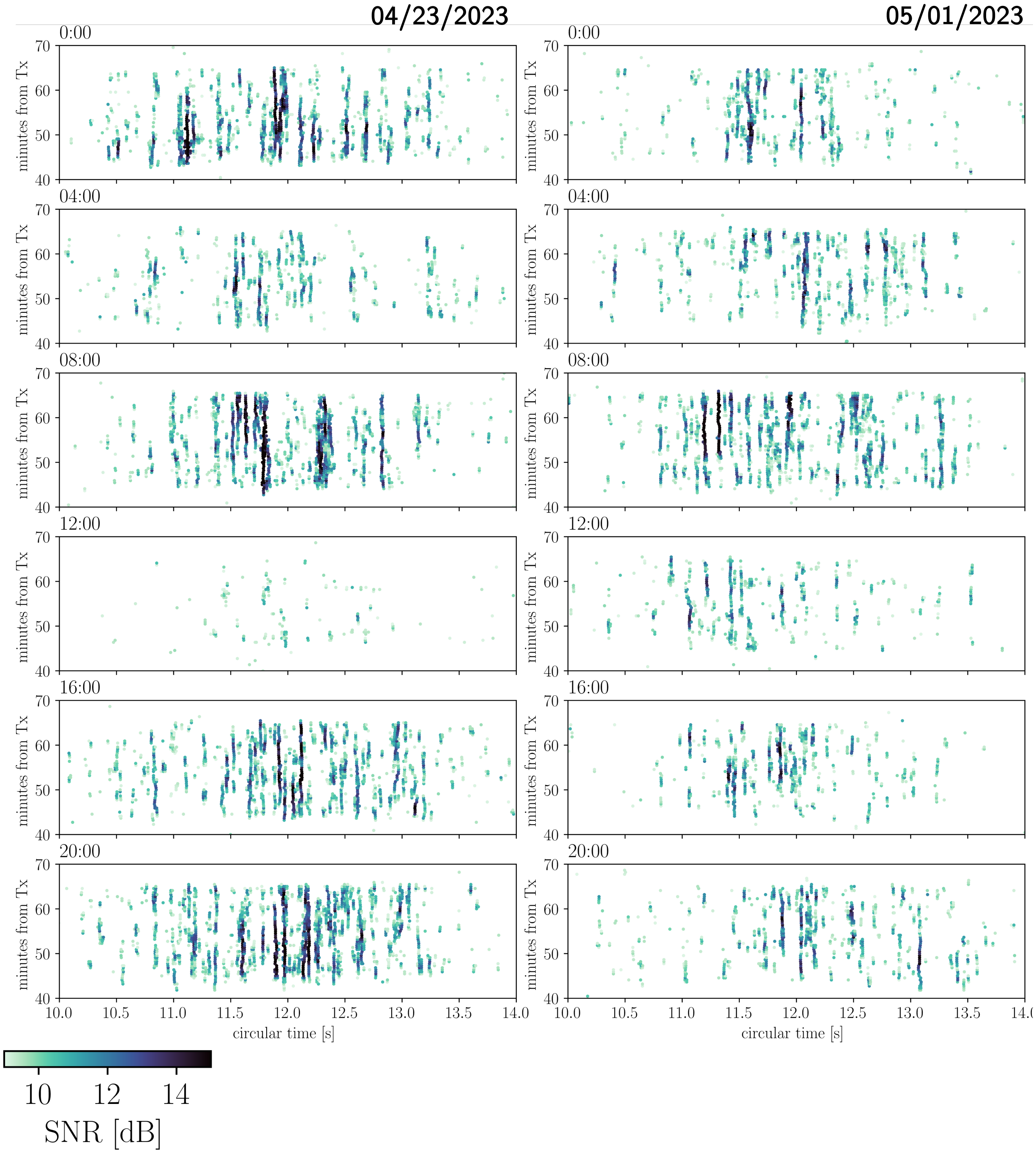

Figure 6.4: High time resolution receptions over a single day at the Oregon Offshore hydrophone location.

Chapter 7

CONCLUSION

Annual human energy consumption is currently at about 10 % of energy captured by land photosynthesis, which is already a humbling percentage. But projecting into the future, various models of human energy consumption including continued exponential growth and more efficient uses of energy all eclipse the total energy captured by land photosynthesis within this century [2]. Energy use is not necessarily bad, in so far as it will go towards lifting the quality of life for billions of humans. But, at human energy consumption scales similar to global photosynthesis, the system will be heavily determined by decisions that we make as a human civilization.* To make these decisions responsibly, we need a global network of system observations that can resolve every spatial scale,† and a critical piece to this infrastructure will be a global ocean observing system. A global ocean observing system will provide invaluable data to better inform our models of how ocean processes work, and will also provide direct observations of the ocean as it inevitably changes. The increased understanding of ocean processes and direct observations of the changing ocean state will serve to inform our decisions related to being resilient to climate change, and a well managed future for human civilization.

With their potential to economically scale, and the complementary integrated nature of their measurements, acoustic based methods of observing the ocean should play a critical role in the total ocean observing system [37, 65]. In this work, continued progress in two different methods for measuring acoustic propagation, both of which utilize existing passive acoustic monitoring infrastructure, is presented. In Chapter 2, a preliminary analysis of the ambient sound statistics is reported, which informs all subsequent Chapters. Additionally, the statistical analysis in Chapter 2 serves to inform other fields such as understanding human contributions to underwater sound and acoustically monitoring marine mammals.

---

[*] For further discussion around this topic see [2], a video of which is available online `https://www.youtube.com/watch?v=OaDzggJw3Ac&t=2388s&ab_channel=ArielAnbar`. The section of the lecture related to this discussion begins at 35:35, however the entire lecture is worth watching.

[†] Such a system, and plans to implement it are envisioned by the as the Global Climate Observing System (GCOS). `https://gcos.wmo.int/en/home`

Ambient noise interferometry utilizes diffuse ambient sound to passively illuminate acoustic propagation between two sensors. In this work, two hydrophones separated by 3.2 km and bottom mounted at a depth of 1500 m are used with this technique. In Chapter 3, the cross-correlations of the ambient sound are shown to consistently converge to an estimate of the empirical Green's function between the hydrophones, which contain multi-path propagation peaks. This was the first time that deep ocean, multi-path peaks had been observed with the technique of ambient noise interferometry. The emergence of the empirical Green's function with averaging time and the long-term trends in signal-to-noise ratio were also quantified. In Chapter 4, a seismic reflection survey is used as a data of opportunity to show that the steep angle propagation paths seen in Chapter 3 are illuminated by local surface sources, which indicates that the most likely source mechanism used to illuminate the acoustic propagation is surface generated wind noise. Chapter 5 estimates the acoustic arrival time for the single surface reflection path and uses the estimated acoustic propagation time to invert for depth-averaged water temperature with an RMS difference of 0.13 °C compared to the HYCOM ocean model. Averaging times on the order of one month were used and seasonal fluctuations in depth averaged water temperature were clearly resolved. I also demonstrated that averaging times as small as 100 hours could resolve acoustic arrival times with an accuracy of approximately 1.5 ms, corresponding to depth averaged ocean temperature accuracy of 0.2 °C. Within this work, ambient noise interferometry has been shown to be capable of measuring internal ocean temperature, but it also has other applications such as self localization and estimating currents.

In Chapter 6, the use of single, bottom mounted hydrophones to receive ocean basin acoustic transmissions from the Kauai Beacon (KB) is demonstrated to be feasible, with consistent arrivals being demonstrated over the first year of KB operation. These arrivals are compared to simulated acoustic arrivals, and agree. The quantifying of the arrival structure and documenting of the arrivals for various hydrophone geometries is a necessary first step in using this data of opportunity for ocean acoustic thermometry. It can also serve to further our understanding of long-range acoustic propagation in the ocean, and developing acoustic based localization methods analogous to an underwater GPS.

Both ambient sound cross-correlations and ocean basin acoustic receptions leverage existing passive acoustic monitoring infrastructure. These techniques, along with seismic ocean thermometry [16, 176], stand to be promising methods to contribute to observations of deep ocean temperature, or other oceanographic variables. As passive acoustic monitoring infrastructure continues to expand with ocean observatories and future technologies like SMART cables [64, 118], acoustic methods such as those presented within this work will have the potential to globally observe the ocean acoustically.

BIBLIOGRAPHY

[1] A. Alvarez, C. Harrison, and M. Siderius. Predicting underwater ocean noise with genetic algorithms. *Physics Letters A*, 280(4):215–220, February 2001.

[2] Ariel Anbar. The Science of Living Worlds - Carl Sagan lecture, December 2022.

[3] Victor C. Anderson. Variation of the vertical directionality of noise with depth in the North Pacific. *The Journal of the Acoustical Society of America*, 66(5):1446–1452, November 1979.

[4] Rex K. Andrew, Bruce M. Howe, and James A. Mercer. Long-time trends in ship traffic noise for four sites off the North American West Coast. *The Journal of the Acoustical Society of America*, 129(2):642–651, February 2011.

[5] Rex K. Andrew, Bruce M. Howe, James A. Mercer, and Matthew A. Dzieciuch. Ocean ambient sound: Comparing the 1960s with the 1990s for a receiver off the California coast. *Acoustics Research Letters Online*, 3(2):65–70, April 2002.

[6] R. W. Bannister. Deep sound channel noise from high-latitude winds. *The Journal of the Acoustical Society of America*, 79(1):41–48, January 1986.

[7] G. D. Bensen, M. H. Ritzwoller, M. P. Barmin, A. L. Levshin, F. Lin, M. P. Moschetti, N. M. Shapiro, and Y. Yang. Processing seismic ambient noise data to obtain reliable broad-band surface wave dispersion measurements. *Geophysical Journal International*, 169(3):1239–1260, June 2007.

[8] J. Berger, J.-R. Bidlot, M. A. Dzieciuch, W. E. Farrell, P. F. Worcester, and R. A. Stephen. A deep ocean acoustic noise floor, 1–800 Hz. *The Journal of the Acoustical Society of America*, 143(2):1223–1233, February 2018.

[9] Pierre Boué, Marine Denolle, Naoshi Hirata, Shigeki Nakagawa, and Gregory C. Beroza. Beyond basin resonance: Characterizing wave propagation using a dense array and the ambient seismic field. *Geophysical Journal International*, 206(2):1261–1272, August 2016.

[10] Laura A. Brooks and Peter Gerstoft. Green's function approximation from cross-correlations of 20–100Hz noise during a tropical storm. *The Journal of the Acoustical Society of America*, 125(2):723–734, February 2009.

[11] Michael G. Brown, Oleg A. Godin, Neil J. Williams, Nikolay A. Zabotin, Liudmila Zabotina, and Geoffrey J. Banker. Acoustic Green's function extraction from ambient noise in a coastal ocean environment. *Geophysical Research Letters*, 41(15):5555–5562, 2014.

[12] Michael G. Brown, Oleg A. Godin, Neil J. Williams, Nikolay A. Zabotin, Liudmila Zabotina, and Geoffrey J. Banker. Acoustic Green's function extraction from ambient noise in a coastal ocean environment. *Geophysical Research Letters*, 41(15):5555–5562, 2014.

[13] Michael G. Brown and Chuntao Lu. Green's function retrieval in a field of random water waves. *Wave Motion*, 60:8–19, January 2016.

[14] Michael J. Buckingham. On the two-point cross-correlation function of anisotropic, spatially homogeneous ambient noise in the ocean and its relationship to the Green's function. *The Journal of the Acoustical Society of America*, 129(6):3562–3576, June 2011.

[15] Jessica C. Burtenshaw, Erin M. Oleson, John A. Hildebrand, Mark A. McDonald, Rex K. Andrew, Bruce M. Howe, and James A. Mercer. Acoustic and satellite remote sensing of blue whale seasonality and habitat in the Northeast Pacific. *Deep Sea Research Part II: Topical Studies in Oceanography*, 51(10):967–986, May 2004.

[16] Jörn Callies, Wenbo Wu, Shirui Peng, and Zhongwen Zhan. Vertical-Slice Ocean Tomography With Seismic Waves. *Geophysical Research Letters*, 50(8):e2023GL102881, 2023.

[17] J. Caplan-Auerbach, R. P. Dziak, J. Haxel, D. R. Bohnenstiehl, and C. Garcia. Explosive processes during the 2015 eruption of Axial Seamount, as recorded by seafloor hydrophones. *Geochemistry, Geophysics, Geosystems*, 18(4):1761–1774, 2017.

[18] G. Carter. Time delay estimation for passive sonar signal processing. *IEEE Transactions on Acoustics, Speech, and Signal Processing*, 29(3):463–470, June 1981.

[19] W Chadwick, R Embley, D Clague, and Butterfield. Processed Swath Bathymetry Grids (NetCDF:GMT format) derived from Multibeam Sonar Data from the Juan de Fuca - Axial Seamount assembled as part of the JdF_Gorda:NOAA_VENTS Data Compilation., 2015.

[20] William W. Chadwick Jr., William S. D. Wilcock, Scott L. Nooner, Jeffrey W. Beeson, Audra M. Sawyer, and T.-K. Lau. Geodetic Monitoring at Axial Seamount Since Its

2015 Eruption Reveals a Waning Magma Supply and Tightly Linked Rates of Deformation and Seismicity. *Geochemistry, Geophysics, Geosystems*, 23(1):e2021GC010153, 2022.

[21] N. Ross Chapman and Andrea Price. Low frequency deep ocean ambient noise trend in the Northeast Pacific Ocean. *The Journal of the Acoustical Society of America*, 129(5):EL161–EL165, May 2011.

[22] Michael D. Collins. A split-step Padé solution for the parabolic equation method. *The Journal of the Acoustical Society of America*, 93(4):1736–1742, April 1993.

[23] John A. Colosi and Stanley M. Flatté. Mode coupling by internal waves for multimegameter acoustic propagation in the ocean. *The Journal of the Acoustical Society of America*, 100(6):3607–3620, December 1996.

[24] John A. Colosi, Edward K. Scheer, Stanley M. Flatté, Bruce D. Cornuelle, Matthew A. Dzieciuch, Walter H. Munk, Peter F. Worcester, Bruce M. Howe, James A. Mercer, Robert C. Spindel, Kurt Metzger, Theodore G. Birdsall, and Arthur B. Baggeroer. Comparisons of measured and predicted acoustic fluctuations for a 3250-km propagation experiment in the eastern North Pacific Ocean. *The Journal of the Acoustical Society of America*, 105(6):3202–3218, June 1999.

[25] John A. Colosi, Edward K. Scheer, Stanley M. Flatté, Bruce D. Cornuelle, Matthew A. Dzieciuch, Walter H. Munk, Peter F. Worcester, Bruce M. Howe, James A. Mercer, Robert C. Spindel, Kurt Metzger, Theodore G. Birdsall, and Arthur B. Baggeroer. Comparisons of measured and predicted acoustic fluctuations for a 3250-km propagation experiment in the eastern North Pacific Ocean. *The Journal of the Acoustical Society of America*, 105(6):3202–3218, June 1999.

[26] THE ATOC CONSORTIUM. Ocean Climate Change: Comparison of Acoustic Tomography, Satellite Altimetry, and Modeling. *Science*, 281(5381):1327–1332, August 1998.

[27] Benjamin F. Cron and Charles H. Sherman. Spatial-Correlation Functions for Various Noise Models. *The Journal of the Acoustical Society of America*, 34(11):1732–1736, November 1962.

[28] Benjamin F. Cron and Charles H. Sherman. Addendum: Spatial-Correlation Functions for Various Noise Models [J. Acoust. Soc. Am. 34, 1732–1736 (1962)]. *The Journal of the Acoustical Society of America*, 38(5):885–885, November 1965.

[29] Keith R. Curtis, Bruce M. Howe, and James A. Mercer. Low-frequency ambient sound in the North Pacific: Long time series observations. *The Journal of the Acoustical Society of America*, 106(6):3189–3200, November 1999.

[30] Peter H. Dahl, David R. Dall'Osto, and Michael J. Harrington. Trends in low-frequency underwater noise off the Oregon coast and impacts of COVID-19 pandemic. *The Journal of the Acoustical Society of America*, 149(6):4073–4077, June 2021.

[31] M. A. Denolle, E. M. Dunham, G. A. Prieto, and G. C. Beroza. Ground motion prediction of realistic earthquake sources using the ambient seismic field. *Journal of Geophysical Research: Solid Earth*, 118(5):2102–2118, 2013.

[32] Emanuele Di Lorenzo and Nathan Mantua. Multi-year persistence of the 2014/15 North Pacific marine heatwave. *Nature Climate Change*, 6(11):1042–1047, November 2016.

[33] Carlos M. Duarte, Lucille Chapuis, Shaun P. Collin, Daniel P. Costa, Reny P. Devassy, Victor M. Eguiluz, Christine Erbe, Timothy A. C. Gordon, Benjamin S. Halpern, Harry R. Harding, Michelle N. Havlik, Mark Meekan, Nathan D. Merchant, Jennifer L. Miksis-Olds, Miles Parsons, Milica Predragovic, Andrew N. Radford, Craig A. Radford, Stephen D. Simpson, Hans Slabbekoorn, Erica Staaterman, Ilse C. Van Opzeeland, Jana Winderen, Xiangliang Zhang, and Francis Juanes. The soundscape of the Anthropocene ocean. *Science*, 371(6529):eaba4658, February 2021.

[34] B. D. Dushaw, P. F. Worcester, W. H. Munk, R. C. Spindel, J. A. Mercer, B. M. Howe, K. Metzger Jr., T. G. Birdsall, R. K. Andrew, M. A. Dzieciuch, B. D. Cornuelle, and D. Menemenlis. A decade of acoustic thermometry in the North Pacific Ocean. *Journal of Geophysical Research: Oceans*, 114(C7), 2009.

[35] B. D. Dushaw, P. F. Worcester, W. H. Munk, R. C. Spindel, J. A. Mercer, B. M. Howe, K. Metzger Jr., T. G. Birdsall, R. K. Andrew, M. A. Dzieciuch, B. D. Cornuelle, and D. Menemenlis. A decade of acoustic thermometry in the North Pacific Ocean. *Journal of Geophysical Research: Oceans*, 114(C7), 2009.

[36] B.D. Dushaw, B.M. Howe, J.A. Mercer, R.C. Spindel, A.B. Baggeroer, D. Menemenlis, C. Wunsch, T.G. Birdsall, K. Metzger, C. Clark, J.A. Colosi, B.D. Comuelle, M. Dzieciuch, W. Munk, P.F. Worcester, D. Costa, and A.M.G. Forbes. Multimegameter-range acoustic data obtained by bottom-mounted hydrophone arrays for measurement of ocean temperature. *IEEE Journal of Oceanic Engineering*, 24(2):202–214, April 1999.

[37] Brian D. Dushaw. Surprises in Physical Oceanography: Contributions from Ocean Acoustic Tomography. *Tellus: Dynamic Meteorology and Oceanography, Series A*, 74(1):33–67, 2022.

[38] L.G. Evers, K. Wapenaar, K.D. Heaney, and M. Snellen. Deep ocean sound speed characteristics passively derived from the ambient acoustic noise field. *Geophysical Journal International*, 210(1):27–33, July 2017.

[39] Mehdi Farrokhrooz, Kathleen E. Wage, Matthew A. Dzieciuch, and Peter F. Worcester. Vertical line array measurements of ambient noise in the North Pacific. *The Journal of the Acoustical Society of America*, 141(3):1571–1581, March 2017.

[40] S. E. Fried, W. A. Kuperman, Karim G. Sabra, and Philippe Roux. Extracting the local Green's function on a horizontal array from ambient ocean noise. *The Journal of the Acoustical Society of America*, 124(4):EL183–EL188, September 2008.

[41] Martin Gassmann, Sean M. Wiggins, and John A. Hildebrand. Deep-water measurements of container ship radiated noise signatures and directionality. *The Journal of the Acoustical Society of America*, 142(3):1563–1574, September 2017.

[42] Kay L. Gemba, Nicholas C. Durofchalk, David R. Dall'Osto, Rex K. Andrew, Paul Leary, Bruce M. Howe, and Kevin B. Smith. Basin scale coherence of Kauai-Beacon m-sequence transmissions received at Wake Island and Monterey, CA. *JASA Express Letters*, 3(8):080801, August 2023.

[43] O. A. Godin. On the possibility of using acoustic reverberation for remote sensing of ocean dynamics. *Acoustical Physics*, 58(1):129–138, January 2012.

[44] O. A. Godin, B. G. Katsnelson, Jixing Qin, M. G. Brown, N. A. Zabotin, and Xiaoqin Zang. Application of time reversal to passive acoustic remote sensing of the ocean. *Acoustical Physics*, 63(3):309–320, May 2017.

[45] Oleg A. Godin. Accuracy of the deterministic travel time retrieval from cross-correlations of non-diffuse ambient noise. *The Journal of the Acoustical Society of America*, 126(6):EL183–EL189, December 2009.

[46] Oleg A. Godin. Emergence of deterministic Green's functions from noise generated by finite random sources. *Physical Review E*, 80(6):066605, December 2009.

[47] Oleg A. Godin. Cross-correlation function of acoustic fields generated by random high-frequency sources. *The Journal of the Acoustical Society of America*, 128(2):600–610, August 2010.

[48] Oleg A. Godin. Acoustic noise interferometry in a time-dependent coastal ocean. *The Journal of the Acoustical Society of America*, 143(2):595–604, February 2018.

[49] Oleg A. Godin, Michael G Brown, Nikolay A. Zabotin, Liudmila Y. Zabotina, and Neil J. Williams. Passive acoustic measurement of flow velocity in the Straits of Florida. *Geoscience Letters*, 1(1):16, December 2014.

[50] Oleg A. Godin, Michael G Brown, Nikolay A. Zabotin, Liudmila Y. Zabotina, and Neil J. Williams. Passive acoustic measurement of flow velocity in the Straits of Florida. *Geoscience Letters*, 1(1):16, December 2014.

[51] Oleg A. Godin, Ernst M. Uzhansky, Tsuwei Tan, Boris G. Katsnelson, Dexter Y. Tan, Thomas Renucci, Antoine Voyer, and Ryan M. McMullin. Acoustic characterization of the seabed with a single-element time-reversal mirror. *Applied Acoustics*, 210:109442, July 2023.

[52] Oleg A. Godin, Nikolay A. Zabotin, and Valery V. Goncharov. Ocean tomography with acoustic daylight. *Geophysical Research Letters*, 37(13), 2010.

[53] Solomon Wolf Golomb. *Shift Register Sequences*. Holden-Day, 1967.

[54] Valeriy V. Goncharov, Alexandr I. Vedenev, Alexandr V. Shatravin, Andrey S. Shurup, Sergei N. Sergeev, Oleg A. Godin, Nicolay A. Zabotin, and Michael G Brown. Tomographic inversion of measured cross-correlations of ambient noise in shallow water using the ray theory. *Proceedings of Meetings on Acoustics*, 24(1):070005, September 2015.

[55] J. C. Groos, S. Bussat, and J. R. R. Ritter. Performance of different processing schemes in seismic noise cross-correlations. *Geophysical Journal International*, 188(2):498–512, 2012.

[56] Charles R. Harris, K. Jarrod Millman, Stéfan J. van der Walt, Ralf Gommers, Pauli Virtanen, David Cournapeau, Eric Wieser, Julian Taylor, Sebastian Berg, Nathaniel J. Smith, Robert Kern, Matti Picus, Stephan Hoyer, Marten H. van Kerkwijk, Matthew Brett, Allan Haldane, Jaime Fernández del Río, Mark Wiebe, Pearu Peterson, Pierre Gérard-Marchant, Kevin Sheppard, Tyler Reddy, Warren Weckesser, Hameer Abbasi, Christoph Gohlke, and Travis E. Oliphant. Array programming with NumPy. *Nature*, 585(7825):357–362, September 2020.

[57] Leila Hatch, Christopher Clark, Richard Merrick, Sofie Van Parijs, Dimitri Ponirakis, Kurt Schwehr, Michael Thompson, and David Wiley. Characterizing the Relative Contributions of Large Vessels to Total Ocean Noise Fields: A Case Study Using the Gerry E. Studds Stellwagen Bank National Marine Sactuary. *Environmental Management*, pages 735–752, July 2008.

[58] Samara M. Haver, Jason Gedamke, Leila T. Hatch, Robert P. Dziak, Sofie Van Parijs, Megan F. McKenna, Jay Barlow, Catherine Berchok, Eva DiDonato, Brad Hanson, Joseph Haxel, Marla Holt, Danielle Lipski, Haru Matsumoto, Christian Meinig, David K. Mellinger, Sue E. Moore, Erin M. Oleson, Melissa S. Soldevilla, and Holger Klinck. Monitoring long-term soundscape trends in U.S. Waters: The NOAA/NPS Ocean Noise Reference Station Network. *Marine Policy*, 90:6–13, April 2018.

[59] John A. Hildebrand, Kaitlin E. Frasier, Simone Baumann-Pickering, and Sean M. Wiggins. An empirical model for wind-generated ocean noise. *The Journal of the Acoustical Society of America*, 149(6):4516–4533, June 2021.

[60] Rachel R. Holser, Theresa R. Keates, Daniel P. Costa, and Christopher A. Edwards. Extent and Magnitude of Subsurface Anomalies During the Northeast Pacific Blob as Measured by Animal-Borne Sensors. *Journal of Geophysical Research: Oceans*, 127(7):e2021JC018356, 2022.

[61] B.M. Howe, S.G. Anderson, A. Baggeroer, J.A. Colosi, K.R. Hardy, D. Horwitt, F.W. Karig, S. Leach, J.A. Mercer, K. Metzger, L.O. Olson, D.A. Peckham, D.A. Reddaway, R.R. Ryan, R.P. Stein, K. von der Heydt, J.D. Watson, S.L. Weslander, and P.F. Worcester. Instrumentation for the Acoustic Thermometry of Ocean Climate (ATOC) prototype Pacific Ocean network. In *OCEANS '95 MTS/IEEE 'Challenges of Our Changing Global Environment'. Conference Proceedings*, volume 3, pages 1483–1500 vol.3, October 1995.

[62] B.M. Howe, B.D. Cornuelle, B.D. Dushaw, M.A. Dzieciuch, D. Menemenlis, J.A. Mercer, W.H. Munk, R.C. Spindel, D. Stammer, P.F. Worcester, and M.R. Zarnetske. Acoustic remote sensing of large-scale temperature variability in the North Pacific Ocean. In *Oceans '04 MTS/IEEE Techno-Ocean '04 (IEEE Cat. No.04CH37600)*, volume 3, pages 1504–1506, Kobe, Japan, 2004. IEEE.

[63] Bruce M. Howe, Brian K. Arbic, Jérome Aucan, Christopher R. Barnes, Nigel Bayliff, Nathan Becker, Rhett Butler, Laurie Doyle, Shane Elipot, Gregory C. Johnson, Felix Landerer, Stephen Lentz, Douglas S. Luther, Malte Müller, John Mariano, Kate Panayotou, Charlotte Rowe, Hiroshi Ota, Y. Tony Song, Maik Thomas, Preston N. Thomas, Philip Thompson, Frederik Tilmann, Tobias Weber, and Stuart Weinstein. SMART Cables for Observing the Global Ocean: Science and Implementation. *Frontiers in Marine Science*, 6, 2019.

[64] Bruce M. Howe, Brian K. Arbic, Jérome Aucan, Christopher R. Barnes, Nigel Bayliff, Nathan Becker, Rhett Butler, Laurie Doyle, Shane Elipot, Gregory C. Johnson, Felix Landerer, Stephen Lentz, Douglas S. Luther, Malte Müller, John Mariano, Kate Panayotou, Charlotte Rowe, Hiroshi Ota, Y. Tony Song, Maik Thomas, Preston N. Thomas,

Philip Thompson, Frederik Tilmann, Tobias Weber, and Stuart Weinstein. SMART Cables for Observing the Global Ocean: Science and Implementation. *Frontiers in Marine Science*, 6, 2019.

[65] Bruce M. Howe, Jennifer Miksis-Olds, Eric Rehm, Hanne Sagen, Peter F. Worcester, and Georgios Haralabus. Observing the Oceans Acoustically. *Frontiers in Marine Science*, 6, 2019.

[66] HYCOM. Hybrid-Cooridinate Ocean Model, 2024.

[67] Lawrence E. Kinsler, Austin R. Frey, Alan B. Coppens, and James V. Sanders. *Fundamentals of Acoustics.* John Wiley & Sons, January 2000.

[68] Holger Klinck, Sharon L. Nieukirk, David K. Mellinger, Karolin Klinck, Haruyoshi Matsumoto, and Robert P. Dziak. Seasonal presence of cetaceans and ambient noise levels in polar waters of the North Atlantic. *The Journal of the Acoustical Society of America*, 132(3):EL176–EL181, September 2012.

[69] V. O. Knudsen, R. S. Alford, and J. W. Emling. Underwater ambient noise. *Journal of Marine Research*, pages 410–429, 1948.

[70] Eric Larose, Ludovic Margerin, Derode Arnaud, Bart Tiggelen, Michel Campillo, Nikolai Shapiro, Anne Paul, Laurent Stehly, and Mickaël Tanter. Correlation of random wavefields: An interdisciplinary review. *Geophysics*, 71:Soc Explorat Geophysicists, July 2006.

[71] Alberto Leon-Garcia. *Probability, Statistics, and Random Processes For Electrical Engineering.* Pearson Higher Ed, November 2011.

[72] Lisa Levin, B. Bett, Andrew Gates, Patrick Heimbach, Bruce Howe, Felix Janssen, Andrea Mccurdy, Henry Ruhl, Paul Snelgrove, Karen Stocks, David Bailey, Simone Baumann-Pickering, Chris Beaverson, Mark Benfield, David Booth, Marina Carreiro-Silva, Ana Colaco, Marie Eblé, Ashley Fowler, and Robert Weller. Global Observing Needs in the Deep Ocean. *Frontiers in Marine Science*, 6, May 2019.

[73] Fenghua Li, Xishan Yang, Yanjun Zhang, Wenyu Luo, and Weiming Gan. Passive ocean acoustic tomography in shallow water. *The Journal of the Acoustical Society of America*, 145(5):2823–2830, May 2019.

[74] Guofu Li, Jie Liu, and Shuang Zhang. Enhancing cross correlations of ocean ambient noise in the time domain based on random matrix theory. *The Journal of the Acoustical Society of America*, 152(5):2849–2858, November 2022.

[75] M. Esther Jiménez López, Daniel M. Palacios, Armando Jaramillo Legorreta, Jorge Urbán R, and Bruce R. Mate. Fin whale movements in the Gulf of California, Mexico, from satellite telemetry. *PLOS ONE*, 14(1):e0209324, January 2019.

[76] Barry B. Ma, Jeffrey A. Nystuen, and Ren-Chieh Lien. Prediction of underwater sound levels from rain and wind. *The Journal of the Acoustical Society of America*, 117(6):3555–3565, June 2005.

[77] Kenneth V. Mackenzie. Nine-term equation for sound speed in the oceans. *The Journal of the Acoustical Society of America*, 70(3):807–812, September 1981.

[78] Charles S. McCreery, Frederick K. Duennebier, and George H. Sutton. Correlation of deep ocean noise (0.4–30 Hz) with wind, and the Holu Spectrum—A worldwide constant. *The Journal of the Acoustical Society of America*, 93(5):2639–2648, May 1993.

[79] Mark A. McDonald, John A. Hildebrand, and Spahr C. Webb. Blue and fin whales observed on a seafloor array in the Northeast Pacific. *The Journal of the Acoustical Society of America*, 98(2):712–721, August 1995.

[80] Mark A. McDonald, John A. Hildebrand, and Sean M. Wiggins. Increases in deep ocean ambient noise in the Northeast Pacific west of San Nicolas Island, California. *The Journal of the Acoustical Society of America*, 120(2):711–718, August 2006.

[81] Mark A. McDonald, John A. Hildebrand, Sean M. Wiggins, and Donald Ross. A 50Year comparison of ambient ocean noise near San Clemente Island: A bathymetrically complex coastal region off Southern California. *The Journal of the Acoustical Society of America*, 124(4):1985–1992, October 2008.

[82] M. F. McKenna, S. L. Katz, S. M. Wiggins, D. Ross, and J. A. Hildebrand. A quieting ocean: Unintended consequence of a fluctuating economy. *The Journal of the Acoustical Society of America*, 132(3):EL169–EL175, August 2012.

[83] Megan F. McKenna, Sean M. Wiggins, and John A. Hildebrand. Relationship between container ship underwater noise levels and ship design, operational and oceanographic conditions. *Scientific Reports*, 3(1):1760, May 2013.

[84] Ravishankar Menon, Peter Gerstoft, and William S. Hodgkiss. Asymptotic Eigenvalue Density of Noise Covariance Matrices. *IEEE Transactions on Signal Processing*, 60(7):3415–3424, July 2012.

[85] Sebastian Menze, Daniel Zitterbart, Martin Biuw, and Olaf Boebel. Estimating the spatial distribution of vocalizing animals from ambient sound spectra using widely spaced recorder arrays and inverse modelling. *The Journal of the Acoustical Society of America*, 146(6):4699–4717, December 2019.

[86] Nathan Merchant, Philippe Blondel, Tom Dakin, and John Dorocicz. Averaging underwater noise levels for environmental assessment of shipping. *The Journal of the Acoustical Society of America*, 132:EL343–EL349, September 2012.

[87] Nathan D. Merchant, Tim R. Barton, Paul M. Thompson, Enrico Pirotta, D. Tom Dakin, and John Dorocicz. Spectral probability density as a tool for ambient noise analysis. *The Journal of the Acoustical Society of America*, 133(4):EL262–EL267, March 2013.

[88] Nathan D. Merchant, Enrico Pirotta, Tim R. Barton, and Paul M. Thompson. Monitoring ship noise to assess the impact of coastal developments on marine mammals. *Marine Pollution Bulletin*, 78(1-2):85–95, January 2014.

[89] Jennifer L. Miksis-Olds, David L. Bradley, and Xiaoyue Maggie Niu. Decadal trends in Indian Ocean ambient sound. *The Journal of the Acoustical Society of America*, 134(5):3464–3475, November 2013.

[90] Jennifer L. Miksis-Olds and Stephen M. Nichols. Is low frequency ocean sound increasing globally? *The Journal of the Acoustical Society of America*, 139(1):501–511, January 2016.

[91] Sally A. Mizroch, Dale W. Rice, Denny Zwiefelhofer, Janice Waite, and Wayne L. Perryman. Distribution and movements of fin whales in the North Pacific Ocean. *Mammal Review*, 39(3):193–227, 2009.

[92] W. Munk. *Achievements in Physical Oceanography.* 2000.

[93] Walter Munk, Peter Worcester, and Carl Wunsch. *Ocean Acoustic Tomography.* Cambridge University Press, 1995.

[94] Nori Nakata, Pierre Boué, Florent Brenguier, Philippe Roux, Valérie Ferrazzini, and Michel Campillo. Body and surface wave reconstruction from seismic noise correlations between arrays at Piton de la Fournaise volcano. *Geophysical Research Letters*, 43(3):1047–1054, 2016.

[95] Brendan Nichols, James Martin, Christopher Verlinden, and Karim G. Sabra. Enhancing ambient noise correlation processing using vector sensors. *The Journal of the Acoustical Society of America*, 145(6):3567–3577, June 2019.

[96] Stephen M. Nichols and David L. Bradley. Global examination of the wind-dependence of very low frequency underwater ambient noise. *The Journal of the Acoustical Society of America*, 139(3):1110–1123, March 2016.

[97] Sharon L. Nieukirk, Kathleen M. Stafford, David K. Mellinger, Robert P. Dziak, and Christopher G. Fox. Low-frequency whale and seismic airgun sounds recorded in the mid-Atlantic Ocean. *The Journal of the Acoustical Society of America*, 115(4):1832–1843, April 2004.

[98] Haiqiang Niu, Emma Ozanich, and Peter Gerstoft. Ship localization in Santa Barbara Channel using machine learning classifiers. *The Journal of the Acoustical Society of America*, 142(5):EL455–EL460, November 2017.

[99] Scott L. Nooner and William W. Chadwick. Inflation-predictable behavior and co-eruption deformation at Axial Seamount. *Science*, 354(6318):1399–1403, December 2016.

[100] OOI. NSF Ocean Observatories Initiative, 2024.

[101] OOI. NSF Ocean Observatories Initiative, 2024.

[102] OOI. NSF Ocean Observatories Initiative, 2024.

[103] OOI. NSF Ocean Observatories Initiative, 2024.

[104] M. B. Porter. The KRAKEN Normal Mode Program. Technical report, NAVAL RESEARCH LAB WASHINGTON DC, May 1992.

[105] Michael B. Porter. BELLHOP Ray Program. Technical report, 2011.

[106] John R. Potter. ATOC: Sound Policy or Enviro-Vandalism? Aspects of a Modern Media-Fueled Policy Issue. *The Journal of Environment & Development*, 3(2):47–62, June 1994.

[107] John Ragland and Shima Abadi. Exploring surface source contributions to ocean ambient noise interferometry with airgun shots. *The Journal of the Acoustical Society of America*, 152(5):3069–3077, November 2022.

[108] John Ragland and Shima Abadi. Long-term ambient noise interferometry in the NE Pacific deep ocean. In *Ocean Sciences Meeting*, volume 2022, Online Meeting, February 2022.

[109] John Ragland and Shima Abadi. Overview of ocean ambient noise interferometry – Theory and simulation. In *183th Meeting of the Acoustical Society of America*, volume 152, page A290, Nashville, TN, October 2022.

[110] John Ragland, Shima Abadi, and Karim Sabra. Long-term noise interferometry analysis in the northeast Pacific Ocean. *The Journal of the Acoustical Society of America*, 151(1):194–204, January 2022.

[111] John Ragland, Felix Schwock, Matthew Munson, and Shima Abadi. An overview of ambient sound using Ocean Observatories Initiative hydrophones. *The Journal of the Acoustical Society of America*, 151(3):2085–2100, March 2022.

[112] James Reagan and Tim et. al. World Ocean Atlas 2023.

[113] Rolling Deck To Repository. Cruise MGL1905 on RV Marcus G. Langseth. 2019.

[114] James Rickett and Jon Claerbout. Acoustic daylight imaging via spectral factorization: Helioseismology and reservoir monitoring. *The Leading Edge*, 18(8):957–960, August 1999.

[115] D. Ross. Ship Sources of Ambient Noise. *IEEE Journal of Oceanic Engineering*, 30(2):257–261, April 2005.

[116] Philippe Roux and W. A. Kuperman. Extracting coherent wave fronts from acoustic ambient noise in the ocean. *The Journal of the Acoustical Society of America*, 116(4):1995–2003, October 2004.

[117] Philippe Roux and W. A. Kuperman. Time reversal of ocean noise. *The Journal of the Acoustical Society of America*, 117(1):131–136, January 2005.

[118] Charlotte A. Rowe, Bruce M. Howe, Matthew J. Fouch, Michael Angove, Jerome Aucan, Christopher R. Barnes, Nigel Bayliff, Nathan C. Becker, Fernando Carrilho, Bill Fry, Helen A. Janiszewski, Anthony Jamelot, Laura S.L. Kong, Stephen T. Lenz, Douglas S. Luther, Giuditta Marinaro, Luis Matias, Amir Salaree, Andi Eka Sakya, Torsten Thiele, Frederik Tilmann, Christa von Hildebrandt-Andrade, Laura M. Wallace, Stuart A. Weinstein, William S.D. Wilcock, and José Barros. SMART Cables Observing the Oceans and Earth. *Marine Technology Society Journal*, 56(5):13–25, October 2022.

[119] Karim G. Sabra, Peter Gerstoft, Philippe Roux, W. A. Kuperman, and Michael C. Fehler. Surface wave tomography from microseisms in Southern California. *Geophysical Research Letters*, 32(14), 2005.

[120] Karim G. Sabra, Philippe Roux, and W. A. Kuperman. Arrival-time structure of the time-averaged ambient noise cross-correlation function in an oceanic waveguide. *The Journal of the Acoustical Society of America*, 117(1):164–174, January 2005.

[121] K.G. Sabra, P. Roux, A.M. Thode, G.L. D'Spain, W.S. Hodgkiss, and W.A. Kuperman. Using ocean ambient noise for array self-localization and self-synchronization. *IEEE Journal of Oceanic Engineering*, 30(2):338–347, April 2005.

[122] K A M Sambell, P S M Smets, D G Simons, M Snellen, and L G Evers. A study on the ambient noise field at a hydroacoustic array near Robinson Crusoe Island. *Geophysical Journal International*, 218(1):88–99, July 2019.

[123] Felix Schwock. *Statistical Analysis of Wind- and Rain-generated Ocean Ambient Noise in the Northeast Pacific Continental Margin.* Thesis, University of Washington, 2021.

[124] Felix Schwock and Shima Abadi. Characterizing underwater noise during rain at the northeast Pacific continental margin. *The Journal of the Acoustical Society of America*, 149(6):4579–4595, June 2021.

[125] Felix Schwock and Shima Abadi. Statistical analysis and modeling of underwater wind noise at the northeast pacific continental margin. *The Journal of the Acoustical Society of America*, 150(6):4166–4177, December 2021.

[126] Felix Schwock and Shima Abadi. Statistical Properties of a Modified Welch Method That Uses Sample Percentiles. In *ICASSP 2021 - 2021 IEEE International Conference on Acoustics, Speech and Signal Processing (ICASSP)*, pages 5165–5169, June 2021.

[127] Felix Schwock, John Ragland, Landung Setiawan, Matthew Munson, Dmitry Volodin, and Shima Abadi. OOIPy: A Python toolbox designed to aid in the scientific analysis of Ocean Observatories Initiative (OOI) data, February 2024.

[128] Paul Scrimger and Richard M. Heitmeyer. Acoustic source-level measurements for a variety of merchant ships. *The Journal of the Acoustical Society of America*, 89(2):691–699, February 1991.

[129] Nikolai M. Shapiro, Michel Campillo, Laurent Stehly, and Michael H. Ritzwoller. High-Resolution Surface-Wave Tomography from Ambient Seismic Noise. *Science*, 307(5715):1615–1618, March 2005.

[130] Martin Siderius and Michael B. Porter. Modeling broadband ocean acoustic transmissions with time-varying sea surfaces. *The Journal of the Acoustical Society of America*, 124(1):137–150, July 2008.

[131] Yvan Simard, Nathalie Roy, Cédric Gervaise, and Samuel Giard. Analysis and modeling of 255 source levels of merchant ships from an acoustic observatory along St. Lawrence Seaway. *The Journal of the Acoustical Society of America*, 140(3):2002–2018, September 2016.

[132] Ana Širović, John A. Hildebrand, and Mark A. McDonald. Ocean ambient sound south of Bermuda and Panama Canal traffic. *The Journal of the Acoustical Society of America*, 139(5):2417–2423, May 2016.

[133] Ana Širović, Lauren N. Williams, Sara M. Kerosky, Sean M. Wiggins, and John A. Hildebrand. Temporal separation of two fin whale call types across the eastern North Pacific. *Marine Biology*, 160(1):47–57, January 2013.

[134] E. K. Skarsoulis and B. D. Cornuelle. Cross-correlation of shipping noise: Refraction and receiver-motion effects. *The Journal of the Acoustical Society of America*, 145(5):3003–3010, May 2019.

[135] E. K. Skarsoulis and B. D. Cornuelle. Cross-correlation sensitivity kernels with respect to noise source distribution. *The Journal of the Acoustical Society of America*, 147(1):1–9, January 2020.

[136] Julius O. Smith. *Spectral Audio Signal Processing.* W3k Publishing, 2011.

[137] Roel Snieder. Extracting the Green's function from the correlation of coda waves: A derivation based on stationary phase. *Physical Review E*, 69(4):046610, April 2004.

[138] Dax C. Soule and William S. D. Wilcock. Fin whale tracks recorded by a seismic network on the Juan de Fuca Ridge, Northeast Pacific Ocean. *The Journal of the Acoustical Society of America*, 133(3):1751–1761, March 2013.

[139] Kathleen M. Stafford, Sharon L. Nieukirk, and Christopher G. Cox. Geographic and seasonal variation of blue whale calls in the North Pacific. *J. Cetacean Res. Manage.*, 3(1):65–76, 2001.

[140] Tsu Wei Tan and Oleg A. Godin. Passive acoustic characterization of sub-seasonal sound speed variations in a coastal ocean. *The Journal of the Acoustical Society of America*, 150(4):2717–2737, October 2021.

[141] Tsu Wei Tan and Oleg A. Godin. Passive acoustic characterization of sub-seasonal sound speed variations in a coastal ocean. *The Journal of the Acoustical Society of America*, 150(4):2717–2737, October 2021.

[142] Tsu Wei Tan, Oleg A. Godin, Michael G. Brown, and Nikolay A. Zabotin. Characterizing the seabed in the Straits of Florida by using acoustic noise interferometry and time warping. *The Journal of the Acoustical Society of America*, 146(4):2321–2334, October 2019.

[143] Tsu Wei Tan, Oleg A. Godin, Boris G. Katsnelson, and Marina Yarina. Passive geoacoustic inversion in the Mid-Atlantic Bight in the presence of strong water column variability. *The Journal of the Acoustical Society of America*, 147(6):EL453–EL459, June 2020.

[144] Tsuwei Tan and Oleg A. Godin. Rapid emergence of empirical Green's functions from cross-correlations of ambient sound on continental shelfa). *The Journal of the Acoustical Society of America*, 154(6):3784–3798, December 2023.

[145] Tsuwei Tan, Oleg A. Godin, Adrien Lefebvre, Wandrille Beaute, Boris G. Katsnelson, and Marina Yarina. Characterizing the seabed by using noise interferometry and time warping. *Proceedings of Meetings on Acoustics*, 35(1):070001, November 2018.

[146] William O. Taylor, Marios N. Anagnostou, Diego Cerrai, and Emmanouil N. Anagnostou. Machine Learning Methods to Approximate Rainfall and Wind From Acoustic Underwater Measurements (February 2020). *IEEE Transactions on Geoscience and Remote Sensing*, 59(4):2810–2821, April 2021.

[147] Paul O. Thompson, Lloyd T. Findley, and Omar Vidal. 20-Hz pulses and other vocalizations of fin whales, Balaenoptera physalus, in the Gulf of California, Mexico. *The Journal of the Acoustical Society of America*, 92(6):3051–3057, December 1992.

[148] Andrea Trucco, Roberto Bozzano, Emanuele Fava, Sara Pensieri, Alessandro Verri, and Annalisa Barla. A Supervised Learning Approach for Rainfall Detection From Underwater Noise Analysis. *IEEE Journal of Oceanic Engineering*, 47(1):213–225, January 2022.

[149] P. L. Tyack, T. Akamatsu, O. Boebel, L. Chapuis, E. Debusschere, C. de Jong, C. Erbe, K. Evans, J. Gedamke, T. Gridley, G. Haralabus, R. Jenkins, J. Miksis-Olds, H. Sagen, F. Thomsen, K. Thomisch, and E. Urban. Ocean Sound Essential Ocean Variable Implementation Plan. Report, International Quiet Ocean Experiment, Scientific Committee on Oceanic Research and Partnership for Observation of the Global Ocean, 2023.

[150] Peter Tyack. Document – Global Ocean Observing System. https://web.archive.org/web/20240117230707/https://goosocean.org/document/22567, June 2020.

[151] Ines Elisa Ulrich, Christian Boehm, Andrea Zunino, Cyrill Bösch, and Andreas Fichtner. Diffuse ultrasound computed tomography for medical imaging, January 2022.

[152] Robert J. Urick. *Principles of Underwater Sound.* McGraw-Hill, New York, 2 edition, 1975.

[153] Robert J. Urick. *Sound Propagation in the Sea.* Department of Defense], Office of the Secretary of Defense, Defense Advanced Research Projects Agency, 1979.

[154] Svein Vagle, William G. Large, and David M. Farmer. An Evaluation of the WOTAN Technique of Inferring Oceanic Winds from Underwater Ambient Sound. *Journal of Atmospheric and Oceanic Technology*, 7(4):576–595, August 1990.

[155] Karina von Schuckmann, Lijing Cheng, Matthew D. Palmer, James Hansen, Caterina Tassone, Valentin Aich, Susheel Adusumilli, Hugo Beltrami, Tim Boyer, Francisco José Cuesta-Valero, Damien Desbruyères, Catia Domingues, Almudena García-García, Pierre Gentine, John Gilson, Maximilian Gorfer, Leopold Haimberger, Masayoshi Ishii, Gregory C. Johnson, Rachel Killick, Brian A. King, Gottfried Kirchengast, Nicolas Kolodziejczyk, John Lyman, Ben Marzeion, Michael Mayer, Maeva Monier, Didier Paolo Monselesan, Sarah Purkey, Dean Roemmich, Axel Schweiger, Sonia I. Seneviratne, Andrew Shepherd, Donald A. Slater, Andrea K. Steiner, Fiammetta Straneo, Mary-Louise Timmermans, and Susan E. Wijffels. Heat stored in the Earth system: Where does the energy go? *Earth System Science Data*, 12(3):2013–2041, September 2020.

[156] R. A. Wagstaff. Low-frequency ambient noise in the deep sound channel—The missing component. *The Journal of the Acoustical Society of America*, 69(4):1009–1014, April 1981.

[157] Stephen C. Wales and Richard M. Heitmeyer. An ensemble source spectra model for merchant ship-radiated noise. *The Journal of the Acoustical Society of America*, 111(3):1211–1231, March 2002.

[158] S. C. Walker. Coherence and interference in diffuse noise: On the information and statistics associated with spatial wave correlations in directional noise fields. *The Journal of the Acoustical Society of America*, 131(3):1987–1998, March 2012.

[159] Shane C. Walker and Michael J. Buckingham. Spatial coherence and cross correlation of three-dimensional ambient noise fields in the ocean. *The Journal of the Acoustical Society of America*, 131(2):1079–1086, February 2012.

[160] Kees Wapenaar. Retrieving the Elastodynamic Green's Function of an Arbitrary Inhomogeneous Medium by Cross Correlation. *Physical Review Letters*, 93(25):254301, December 2004.

[161] William A. Watkins, Peter Tyack, Karen E. Moore, and James E. Bird. The 20-Hz signals of finback whales (Balaenoptera physalus). *The Journal of the Acoustical Society of America*, 82(6):1901–1912, December 1987.

[162] Richard Weaver, Berenice Froment, and Michel Campillo. On the correlation of non-isotropically distributed ballistic scalar diffuse waves. *The Journal of the Acoustical Society of America*, 126(4):1817–1826, October 2009.

[163] Richard L. Weaver and Oleg I. Lobkis. Ultrasonics without a Source: Thermal Fluctuation Correlations at MHz Frequencies. *Physical Review Letters*, 87(13):134301, September 2001.

[164] Richard L. Weaver and Oleg I. Lobkis. Diffuse fields in open systems and the emergence of the Green's function (L). *The Journal of the Acoustical Society of America*, 116(5):2731–2734, November 2004.

[165] Richard L. Weaver and Oleg I. Lobkis. Fluctuations in diffuse field-field correlations and the emergence of the Green's function in open systems. *The Journal of the Acoustical Society of America*, 117(6):3432–3439, June 2005.

[166] Spahr C. Webb. The equilibrium oceanic microseism spectrum. *The Journal of the Acoustical Society of America*, 92(4):2141–2158, October 1992.

[167] Michelle J. Weirathmueller, Kathleen M. Stafford, William S. D. Wilcock, Rose S. Hilmo, Robert P. Dziak, and Anne M. Tréhu. Spatial and temporal trends in fin whale vocalizations recorded in the NE Pacific Ocean between 2003-2013. *PLOS ONE*, 12(10):e0186127, October 2017.

[168] P. Welch. The use of fast Fourier transform for the estimation of power spectra: A method based on time averaging over short, modified periodograms. *IEEE Transactions on Audio and Electroacoustics*, 15(2):70–73, June 1967.

[169] Gordon M. Wenz. Acoustic Ambient Noise in the Ocean: Spectra and Sources. *The Journal of the Acoustical Society of America*, 34(12):1936–1956, December 1962.

[170] William S. D. Wilcock. Tracking fin whales in the northeast Pacific Ocean with a seafloor seismic network. *The Journal of the Acoustical Society of America*, 132(4):2408–2419, October 2012.

[171] William S. D. Wilcock, Maya Tolstoy, Felix Waldhauser, Charles Garcia, Yen Joe Tan, DelWayne R. Bohnenstiehl, Jacqueline Caplan-Auerbach, Robert P. Dziak, Adrien F. Arnulf, and M. Everett Mann. Seismic constraints on caldera dynamics from the 2015 Axial Seamount eruption. *Science*, 354(6318):1395–1399, December 2016.

[172] Katherine Woolfe and Karim Sabra. Variability of the coherent arrivals extracted from low-frequency deep-ocean ambient noise correlations. *The Journal of the Acoustical Society of America*, 138:521–532, August 2015.

[173] Katherine F. Woolfe, Shane Lani, Karim G. Sabra, and W. A. Kuperman. Monitoring deep-ocean temperatures using acoustic ambient noise. *Geophysical Research Letters*, 42(8):2878–2884, 2015.

[174] Peter F. Worcester, Bruce D. Cornuelle, Matthew A. Dzieciuch, Walter H. Munk, Bruce M. Howe, James A. Mercer, Robert C. Spindel, John A. Colosi, Kurt Metzger, Theodore G. Birdsall, and Arthur B. Baggeroer. A test of basin-scale acoustic thermometry using a large-aperture vertical array at 3250-km range in the eastern North Pacific Ocean. *The Journal of the Acoustical Society of America*, 105(6):3185–3201, June 1999.

[175] Peter F. Worcester and Robert C. Spindel. North Pacific Acoustic Laboratory. *The Journal of the Acoustical Society of America*, 117(3):1499–1510, March 2005.

[176] Wenbo Wu, Zhongwen Zhan, Shirui Peng, Sidao Ni, and Jörn Callies. Seismic ocean thermometry. *Science*, 369(6510):1510–1515, September 2020.

[177] Xiaoqin Zang, Michael G. Brown, and Oleg A. Godin. Waveform modeling and inversion of ambient noise cross-correlation functions in a coastal ocean environment. *The Journal of the Acoustical Society of America*, 138(3):1325–1333, September 2015.

Appendix A

HYPERBOLOID SLICE EQUATIONS

The equations for hyperboloid slices corresponding to every image contribution that is plotted in Figs. 4.3 and 4.4 is given below. In the following equations, L is half the distance between the hydrophones, H is the depth of the water, z_s is the depth of the horizontal slice, C is the speed of sound, τ is delay time, and x and y are Cartesian coordinates. For the curves shown in Figs. 4.3 and 4.4 the values of $L = 3.182/2$ km, $H = 1523$ m, $z_s = 12$ m, and $C = 1480.33\ \frac{\mathrm{m}}{\mathrm{s}}$ are used. The hydrophones are assumed to be directly on the ocean bottom, instead of at 1522 m. Table 1 gives the hyperboloid index pair as defined in sections 4.4.1 and the corresponding equation number.

Table A.1: Hyperboloid index pairs as defined in section 4.4.1 and the corresponding equation numbers

hyperboloid indexes	equation number
(0,0)	(A.1)
(1,0)	(A.2)
(2,0)	(A.3)
(3,0)	(A.4)
(1,1)	(A.5)
(2,1)	(A.6)
(3,1)	(A.7)

$$\left(\frac{4\,x^2}{C^2\,\tau^2}-1\right)\left(L^2-\frac{C^2\,\tau^2}{4}\right)-y^2-(H-\mathrm{zs})^2=0 \tag{A.1}$$

$$\left(\frac{4\left(\frac{L\,x}{\sqrt{H^2+L^2}}+\frac{H\,(2\,H-\mathrm{zs})}{\sqrt{H^2+L^2}}\right)^2}{C^2\,\tau^2}-1\right)\times\left(-\frac{C^2\,\tau^2}{4}+H^2+L^2\right)-\left(\frac{H\,x}{\sqrt{H^2+L^2}}-\frac{L\,(2\,H-\mathrm{zs})}{\sqrt{H^2+L^2}}\right)^2-y^2=0 \tag{A.2}$$

$$\left(\frac{4\left(\frac{L\,x}{\sqrt{4\,H^2+L^2}}+\frac{2\,H\,(3\,H-\mathrm{zs})}{\sqrt{4\,H^2+L^2}}\right)^2}{C^2\,\tau^2}-1\right)\times\left(-\frac{C^2\,\tau^2}{4}+4\,H^2+L^2\right)-\left(\frac{2\,H\,x}{\sqrt{4\,H^2+L^2}}-\frac{L\,(3\,H-\mathrm{zs})}{\sqrt{4\,H^2+L^2}}\right)^2-y^2=0 \tag{A.3}$$

$$\left(\frac{4\left(\frac{L\,x}{\sqrt{9\,H^2+L^2}}+\frac{3\,H\,(4\,H-\mathrm{zs})}{\sqrt{9\,H^2+L^2}}\right)^2}{C^2\,\tau^2}-1\right)\times\left(-\frac{C^2\,\tau^2}{4}+9\,H^2+L^2\right)-\left(\frac{3\,H\,x}{\sqrt{9\,H^2+L^2}}-\frac{L\,(4\,H-\mathrm{zs})}{\sqrt{9\,H^2+L^2}}\right)^2-y^2=0 \tag{A.4}$$

$$\left(\frac{4\,x^2}{C^2\,\tau^2}-1\right)\times\left(L^2-\frac{C^2\,\tau^2}{4}\right)-(3\,H-\mathrm{zs})^2-y^2=0 \tag{A.5}$$

$$\left(\frac{4\left(\frac{L\,x}{\sqrt{H^2+L^2}}+\frac{H\,(4\,H-\mathrm{zs})}{\sqrt{H^2+L^2}}\right)^2}{C^2\,\tau^2}-1\right)\times\left(-\frac{C^2\,\tau^2}{4}+H^2+L^2\right)-\left(\frac{H\,x}{\sqrt{H^2+L^2}}-\frac{L\,(4\,H-\mathrm{zs})}{\sqrt{H^2+L^2}}\right)^2-y^2=0 \tag{A.6}$$

$$\left(\frac{4\left(\frac{L\,x}{\sqrt{4\,H^2+L^2}}+\frac{2\,H\,(5\,H-\mathrm{zs})}{\sqrt{4\,H^2+L^2}}\right)^2}{C^2\,\tau^2}-1\right)\times\left(-\frac{C^2\,\tau^2}{4}+4\,H^2+L^2\right) \\ -\left(\frac{2\,H\,x}{\sqrt{4\,H^2+L^2}}-\frac{L\,\left(5\,H-\mathrm{zs}\right)}{\sqrt{4\,H^2+L^2}}\right)^2-y^2=0 \tag{A.7}$$